Investigation of electrical properties of monolayer oxo-functionalized graphene-based two-dimensional materials

Inaugural-Dissertation

to obtain the academic degree

Doctor rerum naturalium (Dr. rer. nat.)

Submitted to the Department of Biology, Chemistry and Pharmacy

of Freie Universität Berlin

by

Zhenping Wang

02/2020

The work presented in this thesis was conducted in the research group of Prof. Dr. Siegfried Eigler from 02/2017 to 02/2020 at Institut für Chemie und Biochemie of Freie Universität Berlin.

1.) Referee: Prof. Dr. Siegfried Eigler (FU Berlin)

2.) Referee: Prof. Dr. Kannan Balasubramanian (HU Berlin)

Defense date: 16.04.2020

Abstract

Chemically modified graphene, such as oxo-functionalized graphene (oxo-G), has received considerable interests for electronic, optoelectronic, biological and chemical sensing applications due to its tunable bandgap, diverse luminescence behaviors and the ability to modify carbon atoms covalently and non-covalently. In contrast to pristine graphene with carbon arranged in a two-dimensional hexagonal lattice, oxo-G consists of abundant sp^3 hybridized carbon atoms due to covalent bonds of carbon with oxo-groups, mainly hydroxyl and epoxy groups. The existence of surface oxo-groups has profound impacts on improving its hydrophilicity, chemical reactivity, catalytic activity, and optical properties, while the effect is detrimental for the electrical conductivity. The defunctionalization of oxo-G by chemical reduction or thermal annealing leads to a certain type of graphene (G), termed as reduced oxo-G (r-oxo-G).

So far, the majority of studies on oxo-G based materials focused on optimizing preparation and reduction methods, understanding preparation protocols and reduction mechanism, and various applications. Deep knowledge about electrical properties and the chemical structure of the reduced oxo-G (r-oxo-G) based materials themselves is still lacking. In detail, no systematic study involves room-temperature transport perfromances of monolayer graphene derived from oxo-G. Currently reported mobility or resistance values were determined from multilayer thin films of the r-oxo-G related materials with unknown thickness and differential quality. It does not make sense for comparing these results obtained from non-standard transport measurements and test conditions. In addition, the structure evolution of the oxo-G remains ambiguous during the thermal annealing treatment.

The thesis presented here is dedicated to study the problems mentioned above by using oxo-G and r-oxo-G with various densities of defects as main research objects. Firstly, substrate effects on the room-temperature electrical transport of monolayer reduced oxo-G with defects of about 0.5% ($^{0.5\%}$G) were studied. The results demonstrated that the monolayer $^{0.5\%}$G on a hexagonal boron nitride (h-BN) substrate exhibited lighter p-doping and smaller hysteresis than on a SiO_2 substrate due to less trapped molecules induced by the h-BN buffer layer. Then, the relation between densities of defects in the range of 0.2% and 1.5% and transport properties was quantitatively investigated. The defects divided graphene domains into isolated small islands with a distance between nearest two defects lower than 3 nm. Therefore, the mobility values of charge carriers of graphene with densities of defects between 0.2% and 1.5%, changed from 0.3 cm^2 V^{-1} s^{-1} and 33.2 cm^2 V^{-1} s^{-1}. Finally, the structural evolution and electrical performances of the monolayer oxo-G during the thermal decomposition process were studied. The defect structures including holes and bilayer C-C sp^3-patches induced by thermal disproportion of the monolayer oxo-G were demonstrated. Scanning tunnelling spectroscopy revealed a semiconducting behavior of the nanometer-sized sp^3 bilayer structures with a bandgap of ~ 0.4 eV. These fundamental studies can help to better understand oxo-functionalized graphene derivatives and promote more extensive applications.

Keywords: oxo-functionalized graphene, atomic structures, mobility, defects

<p style="text-align:center">Contents</p>

1. Introduction

1.1 Atomic structure of pristine graphene

Graphene is a single atomic layer of carbon atoms arranged in a repetitive honeycomb lattice. The primitive unit cell of graphene contains two hexagonal carbon sublattices: A and B, defined by lattice vectors a_1 and a_2 ($|a_1|=|a_2|=0.246$ nm), causing two inequivalent conical points (K and K′) in each Brillouin zone (in the reciprocal space).[1] The valence band (bonding π-states) and conduction band (antibonding π*-states) are intersected at K (K′) point and the crossing point is referred to as Dirac point.[2] Density of states around the Dirac point vanishes linearly.[3] The unique linear energy-momentum dispersion in graphene has led to massless Dirac fermion characteristics and an anomalous quantum Hall effect, which brings graphene many fascinating properties, exemplified by extremely high mobility (10^5 cm^2 V^{-1} s^{-1}) at room temperature and minimum quantum conductivity.[4]
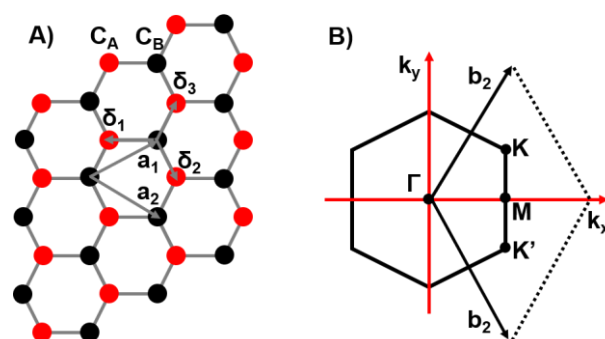
Figure 1.1. A) Honeycomb lattice of graphene and B) its Brillouin zone. $|\delta_1|=|\delta_2|=|\delta_3|=0.142$ nm is the interatomic distance.

1.2 Chemical structure of graphene oxide

1.2.1 Common structure models of graphene oxide

Graphene oxide (GO), a derivative of graphene, is obtained by oxidation of graphite or graphene. The sp^2-bonded carbon atoms arranged in a honeycomb lattice are partially decorated with oxygen-containing functional groups.[5] Because of the non-stoichiometric chemical composition of GO, the precise structure is variable and closely depends on the preparation protocols.[6] The main structural models of GO have been proposed in literatures[6] depicted in **Figure 1.2.1**. Among them, the Lerf-Klinowski model has been most generally accepted. The model was verified by solid state-nuclear magnetic resonance (ss-NMR) experiments executed on ^{13}C labeled samples.[7] It has been demonstrated that hydroxyl- and epoxy-groups decorate the carbon lattice on both sides of the basal plane, while other functional groups like carbonyl-, carboxyl- and ester-groups are mainly attached to the edge.[5-7] Moreover, there also exist minor amounts of peroxide groups or C-centered radicals in GO.[5-7]
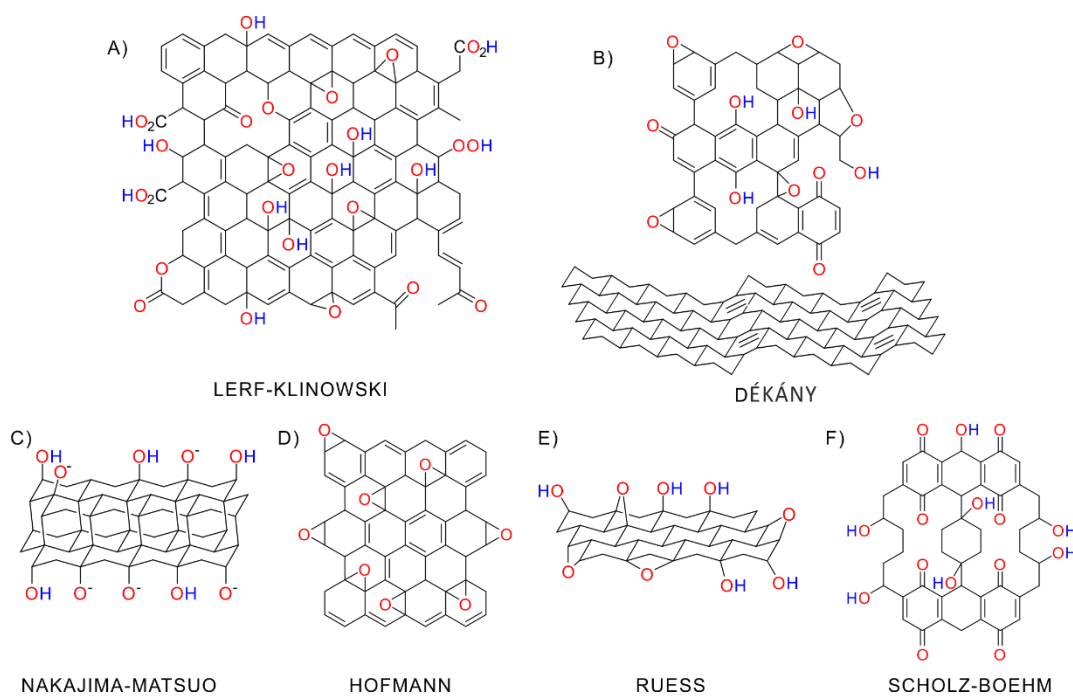
Figure 1.2.1.The main structural models of GO.

1.2.2 Dynamic structure of graphene oxide

All the above proposed models consider GO as a static structure containing fixed functional groups. But in fact, the GO is transforming its chemical structure due to inevitable interactions with water or oxygen. Ayrat M. Dimiev et al. proposed a new dynamic structural model (DSM) of GO (**Figure 1.2.2**) to explain the change of the GO structure in aqueous solutions.[8] The DSM explains that GO does not contain any significant quantity of preexisting acidic functional groups, but gradually generates them through interaction with water. The reaction with water results in C-C bond cleavage, formation of vinylogous carboxylic acids, and the generation of protons. The carboxylic acids may decarboxylate with releasing CO_2.[9] An electrical double layer formed at the GO interface in aqueous solutions plays an important role for the observed GO chemistry. Prolonged exposure of the GO to water gradually degrades GO flakes converting them into humic acid-like structures. Although the DSM provides an explanation for the dynamic transfer of GO in aqueous solutions, the local structure of GO, in particular at defect sites, remains unclear.

2
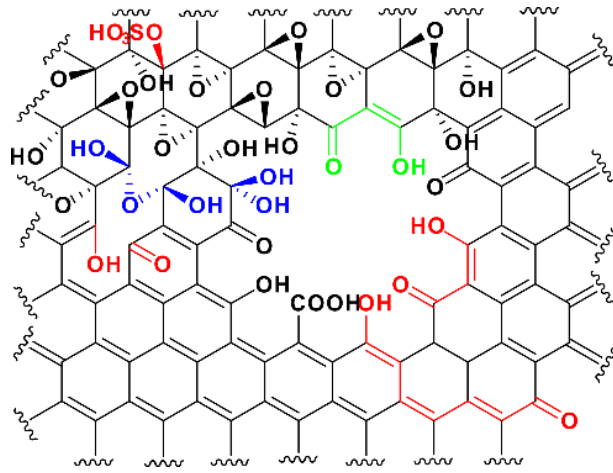
Figure 1.2.2. Dynamic structure of graphene oxide.

1.2.3 Structure model of oxo-functionalized graphene

Oxo-G functionalized graphene (oxo-G), as a sub-class of GO, bears an intact carbon framework, as shown in **Figure 1.2.3**. The main oxo-groups including hydroxyl and epoxy groups are located on both sides of the carbon skeleton. The oxo-G bears a degree of functionalization of around 50%. It can be estimated that every second carbon atom of oxo-G is sp^3-hybridized. Since the formation of defects is almost completely avoided by keeping the whole reaction below 10 °C, the hexagonal carbon lattice was found to be preserved against degradation in contrast to the GO.[10]
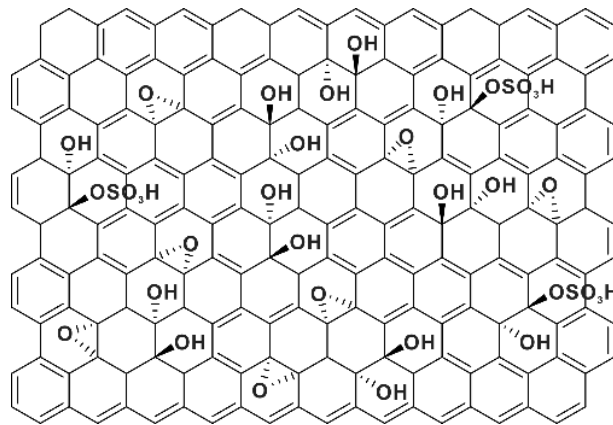
Figure 1.2.3. Illustration of oxo-G with epoxy and hydroxyl groups.

1.3 Bandgap structure of graphene oxide

Unlike gapless graphene, GO has a considerable bandgap of ~2.2 eV,[11] as shown in **Figure 1.3**. The bandgap closely depends on the oxygen atoms contents, configurations and sp^2/sp^3 fraction in GO. Oxygen concentration ranging from 50% to 6.25% led to a related bandgap decrease from 3.0 eV to 0.1 eV, demonstrated by Haiming Huang et al. by using the density functional theory.[12] But the bandgap was found to be a non-monotonic function of the O/C contents at O/C of 11.1% and 25% with values of

0.780 eV and 0.354 eV, respectively. However, the bandgap is proportional to the density of defects. The reduction of GO decreases the bandgap due to the gradual restructuration of the conjugated π-system.
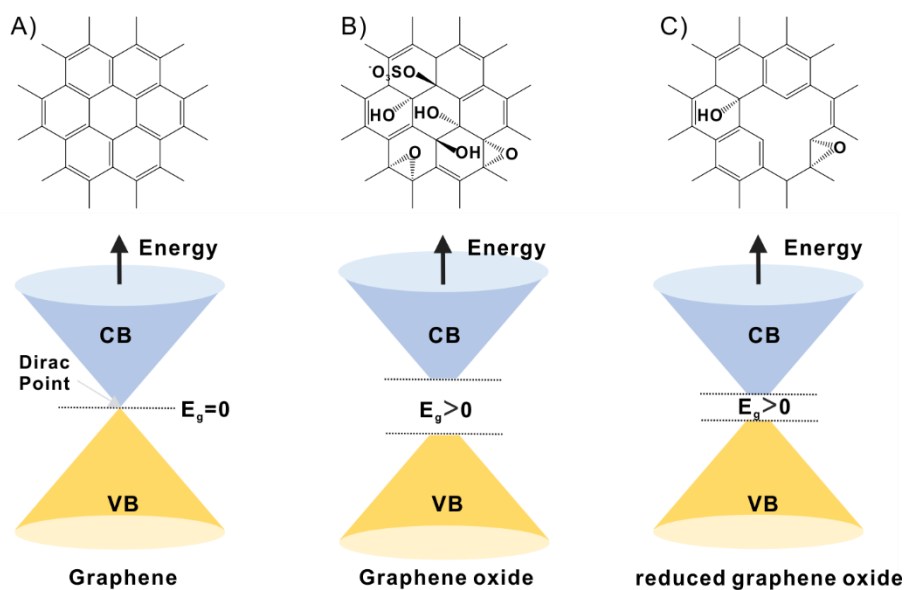
Figure 1.3. Energy band of graphene, graphene oxide and reduced graphene oxide.

1.4 Methods for the synthesis of graphene oxide-based materials

1.4.1 Synthetic methods of graphene oxide

GO is produced from graphite by oxidation with strong oxidants in concentrated acid media. There are multiple routes to prepare GO, including Brodie's method[13], Staudenmaier's method[14], Tour method[15] and Hummers' method[14, 16]. All these methods have in common that graphite oxide is yielded as a brown to yellow solid after removing the solvent. Individual layers of GO are then yielded after delamination. However, over-oxidation under aggressive reaction conditions violently disintegrates the sp²-carbon lattice and results in either vacancy defects or flake-like amorphous carbon. The size of defect-free graphene patches in reduced GO are about 1-10 nm. Over-oxidation during the preparation of GO was identified as reason for the ruptured graphene lattice in GO due to the loss of carbon via formation of CO_2.[9, 17] As verified by Dimiev *et al.* using Hummers' method in first approximation, one CO_2 molecule is formed from 20 carbon atoms. However, kinetically controlled oxidation procedures to obtain oxo-G can effectively hinder the over-oxidation, although the oxidation by harsh oxidants such as potassium permanganate in sulfuric acid or sodium chlorate in nitric acid, as demonstrated by Eigler group.[10] The main preparation methods of GO-based materials are summarized in **Table 1.4.1**.

Table 1.4.1. Main preparation methods of graphene oxide-based materials.

Method	oxidant	Reaction media	Reaction temperature	Reaction time	Carbon/oxygen ratio	Reference
Brodie 1859	$KClO_3$	$HNO_3+H_2SO_4$	Up to 60 °C	3-4 days	2.9	13
Staudenmaier 1898	$KClO_3$	Fuming HNO_3	25 °C	4 days	1.74	14
Hummers 1957	$KMnO_4$ $NaNO_3$	Conc. H_2SO_4	70-90 °C	1.0 hour	0.84-1.8	14, 16
Tour	$KMnO_4$	$H_2SO_4+H_3PO_4$	50 °C	12 hours	0.74	15
Eigler 2013	$KMnO_4$	Conc. H_2SO_4	< 10°C	16 hours	1	10

1.4.2 Mechanism of graphene oxide formation

Conversion of bulk graphite to GO is artificially divided into three separate steps: formation of sulfuric acid-graphite intercalation compound (H_2SO_4-GIC), oxidation of the H_2SO_4-GIC to pristine GO (PGO) and delamination of the PGO.[18] In the first step, the H_2SO_4-GIC exhibits a deep-blue color. The stoichiometry of the H_2SO_4-GIC can be expressed by the equation $C_{(21-28)}^{+} \cdot HSO_4^{-} \cdot 2.5\ H_2SO_4$. The H_2SO_4-GIC formation increases the distance between graphene layers in graphite, which makes the interlayer galleries accessible for the oxidizing agent. In the second step, the oxidizing agent diffuse into the pre-occupied graphene layers from edge to center. The intercalated oxidants directly react with nearby carbon atoms to form the bright-yellow colored PGO. The formation of PGO in the second step is controlled by the rate of diffusion of the oxidizing agent into the H_2SO_4-GIC. However, the diffusion process is significantly slower, which takes several hours or days depending on reaction temperature, oxidizing agents and graphite types. In the third step, by exposing the PGO to water, the GO can be obtained via delamination of the PGO. The whole mechanism of GO formation is shown in below **Figure1.4.2**.
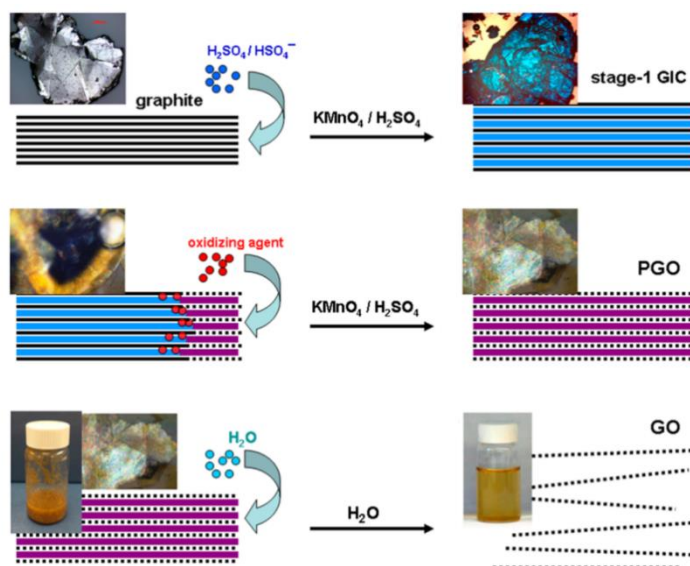
Figure1.4.2. Schematics of conversion of bulk graphite into GO with corresponding micrographic images or sample appearances at each phase. Reproduced from [15] with permission of ACS.

1.5 Defects in oxo-functionalized graphene

1.5.1 Structural models of defects in oxo-functionalized graphene

GO is a heterogeneous material with various lattice defects, which can be roughly categorized into two types: extrinsic defects (on-plane functionalization defects) and intrinsic defects (in-plane lattice defects).[19] The extrinsic defects such as oxo-functional groups mainly stem from the oxidation preparation. The foreign groups severely perturb the sp^2 hybridized carbon lattice in graphene. But particular emphasis is put on the physicochemical phenomena of GO such as tunable bandgap, diverse luminescence, biological compatibility and the ability of chemical modify due to these extrinsic oxo-addends, resulting in considerable interests and potential applications.[20] Thus, engineering this type of defects as structural motifs allows for precisely tailoring the properties of GO according to the specific needs. Intrinsic defects are composed of non-sp^2 hybridized carbon atoms in GO. The intrinsic defects of GO can be divided into four categories: rearrangement defects (such as grain boundaries), cleaved carbon bonds, vacancy defects and holes (**Figure 1.5.1**). Reductive defunctionalization of on-plane functional groups of GO recovers the carbon lattice that remains rearranged. The cleaved C-C bond shown in **Figure 1.5.1B** can be healed after a reductive restoration. The formation of vacancy defects in graphene oxide is the result of CO_2 formation via over-oxidation of the graphene lattice. Thereby, a point defect of a specific diameter is formed, which can be considered as a vacancy. However, the edges of such point defects in graphene oxide must carry functional groups, such as hydroxyl or carbonyl groups. A vacancy defect is not necessarily a hole, because functional groups at edges fill the space of the former C-atoms. However, multiple vacancy defects can form a hole defect. In **Figure 1.5.1G,** a hole in GO is depicted as a result of 35 missing carbon atoms. Consequently, the chemical reduction leads to a hole in graphene. In addition, thermal annealing can increase the size of holes as few nm-scales.[21]
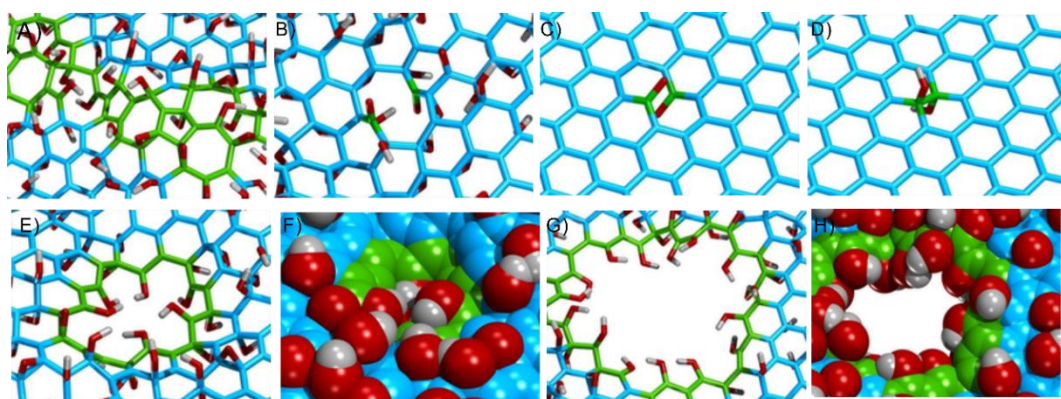
Figure 1.5.1. Illustration of defect types in GO. A) GO with a rearranged carbon lattice. B) GO with cleaved C-C bond forming a 10-membered ring. C) Proposed reduction to in-plane oxo-groups. D) Proposed on-plane hydroxyl groups formed after rearrangement. E) GO with 7 missing C-atoms and hydroxyl terminated edge and F) CPK model. G) GO with 35 missing C-atoms and hydroxyl terminated edge and H) CPK model. Reproduced from [16] with permission of Wiley.

1.5.2. Lattice defects in graphene oxide visualized by transmission electron microscopy

The atomic structure of GO or oxo-G, derived from the oxidation-reduction treatment of graphene, can be visualized by high-resolution transmission electron microscopy (TEM),[22] as shown in **Figure 1.5.2**. Different features are marked in colors of **Figure 1.5.2B**. The largest portion of the layer with coverage portion of about 60%, marked in light gray, corresponds to intact graphene domains with a few nanometer sizes in diameter. There exist the contaminated regions (dark gray shown in **Figure 1.5.2B**) constituting about 30% of the total area, which probably originates from adsorbates or trapped heavier atoms.

Individual atomic substitutions and point defects are colored in red and green, respectively. Some holes with average diameter of 1-2 nm are observed in yellow parts. In addition, quasi-amorphous carbon structures named as extended topological defects appear in blue areas. They cover about 5% of the area. Such high-density topological defects evolve from the strong oxidation-reduction process. Further, defect configurations marked in blue exhibit multiple carbon polygons without an order as shown in **Figure 1.5.2C**. These extended topological defects primarily contain abundant pentagons, heptagons and rotated hexagons in a nanometer-sized region. Note that all carbon atoms in these defective areas are linked to three neighbors by planar sp^2 hybridizations. Moreover, the extended defects introduce apparent in-plane distortions and strain around their adjacent lattice.
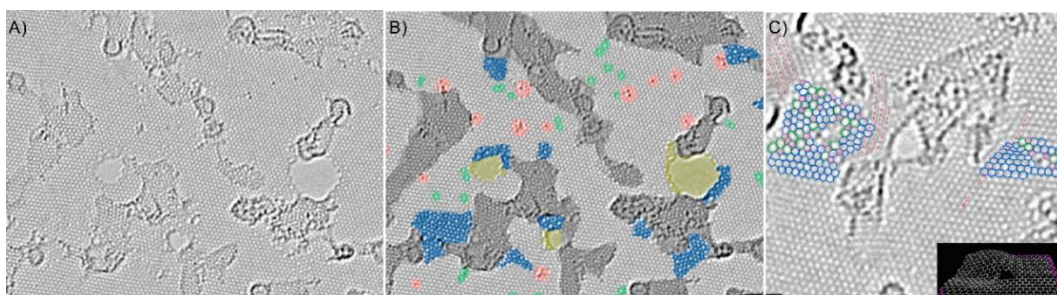

Figure 1.5.2. Atomic structure of monolayer reduced-GO characterized by high-resolution transmission electron microscopy (TEM). (A) Initial TEM image. (B) TEM image with marked areas in color to highlight different areas. (C) Visualized defects and deformations. Reproduced from [19] with permission of ACS.

1.5.3 Lattice defects in graphene oxide visualized by scanning tunneling microscopy

High-resolution scanning tunneling microscopy (STM) can reveal more details about atomic structures of oxygen-functionalized graphene and identify the location of oxidized carbons. A STM image of a single layer GO on a highly oriented pyrolytic graphite (HOPG) substrate,[23] measured at ambient conditions, is shown in **Figure 1.5.3**. Graphene domains in the GO flake are partially preserved. However, it is clear to see that the GO is different from exfoliated graphene or CVD graphene by the appearance of bright spots composed of sp^3 hybridized carbons. They probably originate from the presence of oxygen-addends, calculated by theoretical simulation to array into islands or rows. The degree of functionalization of about 50% of the GO can be roughly estimated by the ratio of ordered areas to bright regions.
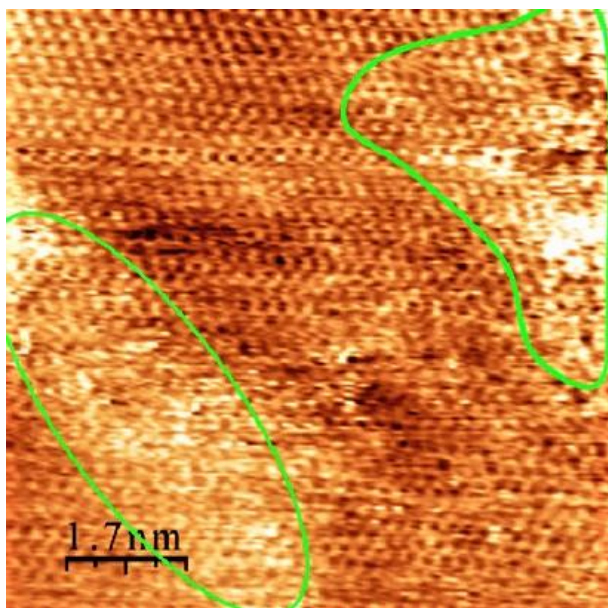
Figure 1.5.3. A STM image of a single layer GO flake on a HOPG substrate, taken at ambient. Reproduced from [20] with permission of ACS.

1.5.4 Determination of the density of defects by Raman spectroscopy

Quantifying defects in graphene related materials is crucial to gain insights into their fundamental properties. Significant efforts on quantifying degree of disorders in graphene materials have been undertaken by using Raman spectroscopy.[24] Raman spectra of graphene with defects between 0.005% and ~1% consist of three main peaks: D peak (1340 cm^{-1}), G peak (1580 cm^{-1}) and 2D peak (2700 cm^{-1}) as shown in **Figure 1.5.4.1**. Moreover, a faint D+D' band at ~2940 cm^{-1} can be observed once defects appear. The shape of Raman spectra of the graphene depends on the concentration of defects.[25] The full width at half maximum (FWHM, Γ) of D, G and 2D peaks increase with increasing density of defects.

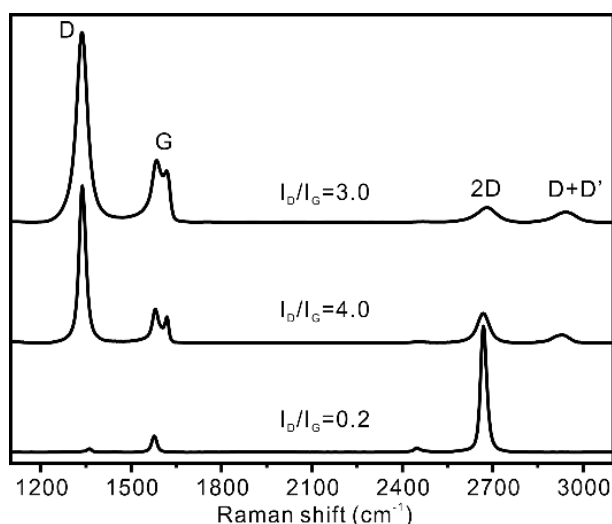**Figure 1.5.4.1.** Raman spectra of graphene with different defects, measured at λ=532 nm.

Furthermore, the intensity ratio of D to G (I_D/I_G) follows a relation of the distance between two nearest defects (L_D). The I_D/I_G ratio is an important indicator to estimate the defects density. In the case of

graphene with a low-defect density (L_D>3 nm), the I_D/I_G increases and corresponds to the decrease of the L_D. On the contrary, for graphene with a high-defect density (L_D≤3 nm), the I_D/I_G increases with decreasing defects and increasing the L_D, respectively.[26] (see **Figure 1.5.4.2a and 1.5.4.2b**).
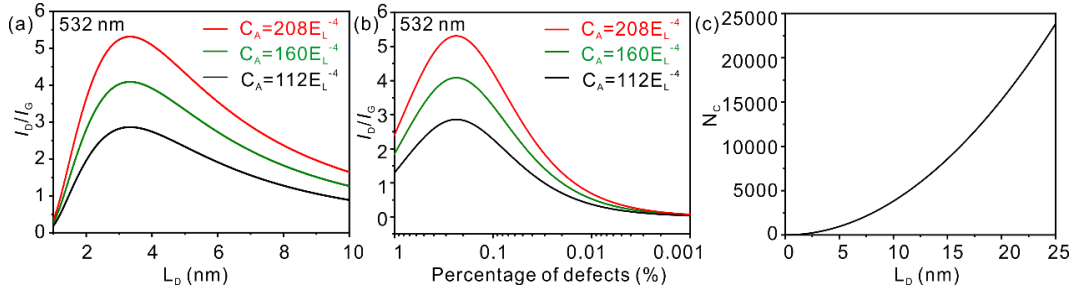

Figure 1.5.4.2. (a) I_D/I_G as s function of L_D. (b) I_D/I_G as s function of percentage of defects (%). The red, green and black curves are given by C_A=208×E_L^{-4}, C_A=160×E_L^{-4} and C_A=112×E_L^{-4}, respectively, where the excitation energies E_L of 532 nm laser is 2.33 eV. (c) The relation between N_C and L_D.

The calculation of the defect density is based on the model introduced and interpreted by Lucchese and Cançado and interpretation by Englert et al.[27] The detailed calculation processes are based on the following three equations. Here r_A and r_S are length scales that determine the region induced by the D band scattering. The C_A parameter is related to the ratio between the efficiency of optical phonons between K and Γ. E_L is the excitation energy (E_L = 2.33 eV, λ_L=532 nm). N_C is the number of carbon atoms in graphene domains. The A_{cell} is a graphene unit cell, where the A_{cell} = 0.246^2sin (60°) = 0.05239 nm^2. The lines in **Figure 1.5.4.2** are fitting curves following the three equations. [21a]

$$v\frac{I_D}{I_G} = C_A \frac{r_A^2-r_S^2}{r_A^2-2r_S^2} [e^{-\pi r_S^2\omega/L_D^2} - e^{-\pi(r_A^2-r_S^2)r_S^2/L_D^2}] \tag{1}$$

$$C_A = (160 \pm 48)E_L^4 \tag{2}$$

$$N_C = 2L_D^2/A_{cell} \tag{3}$$

However, the I_D/I_G ratio is limited to the L_D of around 1 nm, or a density of defects of roughly 1%.[28] Therefore, for the graphene with lattice or functionalized defects exceeding 1%, the density of defects or degree of functionalisation (θ) can be quantified by the absolute Raman D- and G-mode intensities.[28] In **Figure 1.5.4.3,** a continuous increase in both I_D and I_G with the θ was observed, spanning several orders of magnitude. Here θ is directly associated with the presence of C (sp^3) domains.
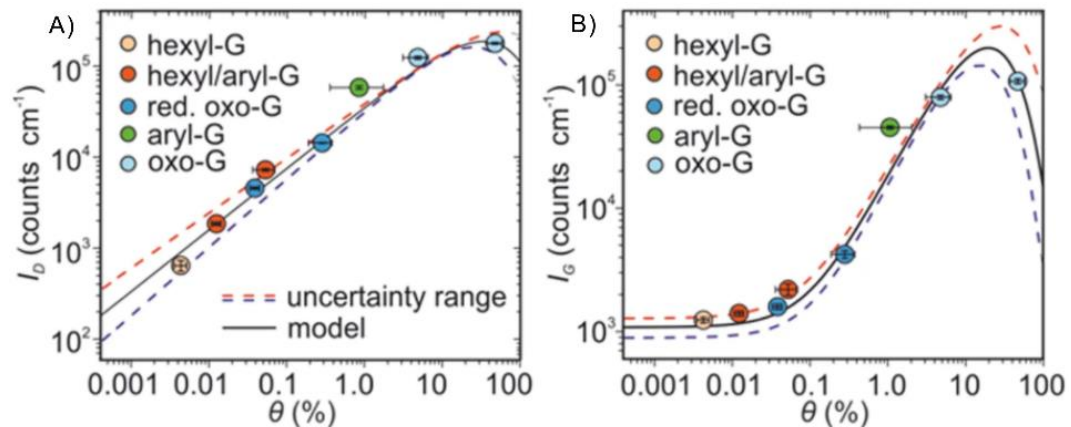
1.6 Graphene based back-gate field effect transistor

1.6.1 Structures of back-gate graphene-based FETs

High carrier mobility, unique electronic band structure and atomically-thin layer structure make graphene promising for field effect transistor (FET) applications.[29] Structure and geometry of a basic back-gate graphene FET are schematically shown in **Figure 1.6.1A**. The SiO$_2$ layer is selected as back-gate dielectric and graphene flakes inserted between source and drain electrodes work as conducting channel. The electrodes, fabricated by electron beam lithography and subsequent gold evaporation, are used to connect external circuits. Applying an extrinsic electrical field induces a potential drop across the SiO$_2$ dielectric layer by separating positive and negative charge carriers on the surface of silicon and graphene, which further changes the carrier density in graphene and therefore its carrier mobility. An optical microscope image of a back-gate FET with monolayer reduced oxo-G prepared by oxidization-reduction processes is shown in **Figure 1.6.1B**.
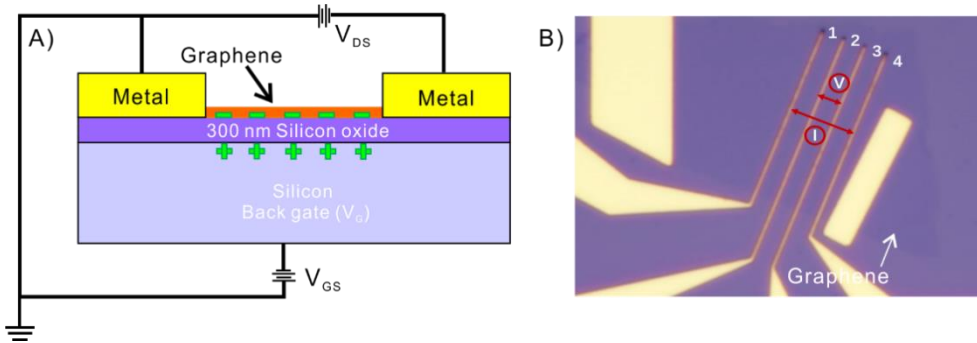

Figure 1.6.1. A) The schematic diagram and B) the optical image of back-gated graphene FET devices.

1.6.2 Electrical field effect of graphene

For a single-layer of pristine graphene, its valence and conduction bands are cone-shaped and cross at the Dirac point. That means the density of states (DOS) at the Dirac point is zero (see inset of **Figure 1.6.2**), which gives rise to the minimum conductance G$_{min}$.[1] Applying an external electrical field effect converts Dirac fermion from electron to hole (or in turn) continuously. The density of single-electron states in conduction (electron concentration, n_e) or single-hole states in the valence band (hole concentration, n_h) as a function of gate voltage is described by equation (4),[29a] where $\varepsilon_0=8.854\times10^{-12}$ F m^{-1} is the permittivity of free space, $\varepsilon_r=3.9$ is the relative permittivity of SiO$_2$ with a thickness of 300 nm, d=300 nm is the thickness of SiO$_2$ layer, e=1.602$\times10^{-19}$ C is the electron charge and $\alpha = \varepsilon_0\varepsilon_r / de = 7.2 \times10^{10}$ cm^{-2} V^{-1}, is charge injection rate in the gate. According the surface charge density (electron or hole density) increases linearly with the gate voltage. In case of doped graphene, the Dirac point shifts away from zero voltage to the electron or hole conduction regime depending on doping type (n- or p- doping)

(**Figure 1.6.2**). The modification of relationship between charge density and gate voltage can be described by equation (5), where the V_{Dirac} serves as an offset value.

$$n = \frac{\varepsilon_0 \varepsilon_r}{de} V_g = \alpha V_g \tag{4}$$

$$n' = \alpha(V_g - V_{Dirac}) = \alpha \Delta V_{Dirac} \tag{5}$$
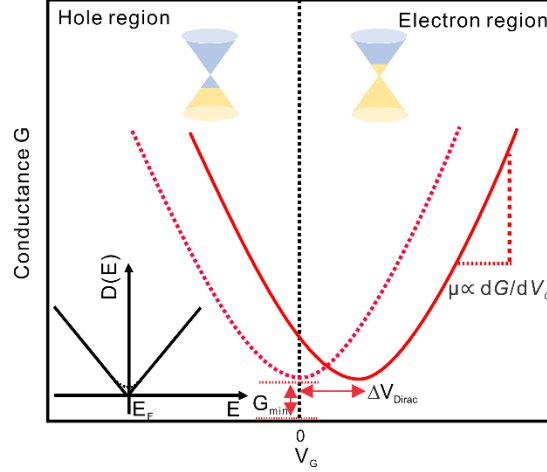

Figure 1.6.2. Conductance versus back-gate voltage measurement for graphene-based FETs. The inset is the theoretical density of states (DOS) of pristine graphene.

The carrier mobility is estimated from the slope (equation (6)),[30] as shown in **Figure 1.6.2**, where V is drift velocity, E is the applied electrical field, σ is the conductivity, n is the carrier density, L and W are the channel length and width, G is the conductivity and C_{ox}= 1.15×10^{-8} F cm^{-2} is the capacitance per unit area of the 300 nm SiO$_2$ dielectric. In theory, mobility values for electrons and holes are equivalent owing to their equal velocities in intrinsic graphene and the symmetrical energy dispersion between conduction and valence band.[1] The carrier mobility closely depends on the quality of graphene (number of layers, grain boundaries, wrinkles or ripples, and doping types and degree) and measurement conditions (applied gate voltage, measuring temperature, dielectric environment, Schottky barrier and substrates).[1]

$$\mu = \frac{V}{E} = \frac{\sigma}{en} = \frac{1}{C_{ox}} \frac{L}{W} \frac{\Delta G}{\Delta V_g} \tag{6}$$

1.6.3 Graphene-based FET devices

Graphene materials with different quality can be prepared by mechanical exfoliation (ME), chemical vapor deposition (CVD) and wet-chemical methods. Typical mobilities for ME graphene range around 10^5 cm^2 V^{-1} s^{-1},[31] which are closest to the theoretical mobility of graphene. But the uneven lateral size, labor-intensive and time-consuming preparation of ME graphene limit it to laboratory researches. The mobility values for CVD graphene on SiO$_2$ surface are usually lower by two orders of magnitude ($\sim 10^3$ cm^2 V^{-1} s^{-1}).[32] In contrast, the faint extrinsic scattering from hexagonal boron nitride (h-BN) improve carrier mobility of the CVD graphene up to $\sim 10^4$ cm^2 V^{-1} s^{-1}.[33] However, the transfer of CVD graphene has been a bottleneck for applications of high-performance graphene-based transistors, since it inevitably introduce defects like grain boundaries and wrinkles. Recent researches on graphene-based FETs involve chemically-derived graphene derivatives, for example, reduced graphene oxide (r-GO).[34] The oxygen-

containing groups existing in r-GO provide qualitative feasibility of functionalization by foreign molecules as molecular recognition sites onto the carbon skeleton to increase sensing ability.[34b] However, the electrical performance in r-GO is much inferior than that of ME and CVD graphene, with representative mobility values between 10^{-2} cm^2 V^{-1} s^{-1} and 10^2 cm^2 V^{-1} s^{-1}.[23, 35] The presence of oxygen functional groups and defects in r-GO interrupt the conjugated π-electron system. Improving the electrical properties of r-GO could be realized by tailoring the fractions of sp^2/sp^3 domains. We demonstrated that the mobility of charge carriers of reduced oxo-G with a density of defects as low as 0.02% is exceeding 1,000 cm^2 V^{-1} s^{-1}, measured at 1.6 K in a Hall-bar configuration.[10] However, the exploration of electrical structures and properties in chemically-derived graphene exists a lot of uncertainty, so further research is needed and faced in this thesis.

1.6.4 Charge transport mechanism in reduced graphene oxide-based materials

The electrical performance of r-GO does not approach those of pristine graphene prepared by ME or CVD methods because of the defects in the material. Sp^3 hybridized areas and lattice defects disrupt the transport of carriers delocalized in the graphene network. The charge transport in the r-GO based materials usually combines both hopping and tunneling mechanism,[36] as shown in **Figure 1.6.4**. For small localized sp^2 clusters, there exist electron and hole puddles near the charge neutrality point, resulting in a large energy gap between valence band and conduction band. Thus, high energy is required to excite the charge carries, leading to a variable range hopping transport. On the contrary, the large sp^2 domains lead to a decreasing potential barrier among valence band and conduction band. As a result, the carrier transport mechanism of r-GO shows a band-like transport (**Figure 1.6.4A**). Structural restoration of conjugated π-electron system in r-GO can change the charge transport from hopping to tunneling, as demonstrated by R. Negishi et al.[37]
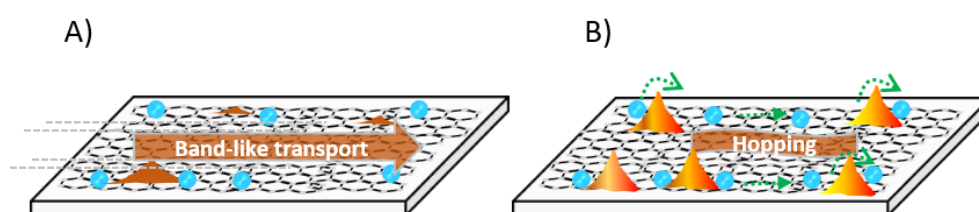
Figure 1.6.4. Illustrations of charge transport pathways of r-GO with (A) low density of defects *via* band-like transport mechanism and (B) high density of defects *via* hopping mechanism.

2. Characterization methods

2.1 Raman spectroscopy on graphene-based materials

Raman spectroscopy has proven to be a powerful tool for characterizing graphene flakes. It is commonly used to determine the number of graphene layers, density of defect, edge chirality, strain, thermal properties and amount of doping.[38] As depicted in **Figure 1.5.4.1**, pristine graphene presents two primary peaks at about 1580 cm^{-1} (G-band) and 2700 cm^{-1} (2D-band). After introducing structural defects, the D peak at 1350 cm^{-1}, D' peak at about 1620 cm^{-1} and their combination D+D' peak at about 2950

cm^{-1} appear. The G-band is related to a doubly-degenerate in-plane stretching vibration of C-C bonds including the transverse optical (TO) mode and longitudinal optical (LO) mode[39] (**Figure 2.1A**). The G-band arises from an incident or scattered photon in either TO or LO zone that vertically motivate electron-hole pair (**Figure 2.1C**). Then, a photon is emitted after radiative recombination of the electron–hole pair. The peak features of the G-band such as the full-width at half-maximum (FWHM) and position can be used to evaluate the deformation and strain of graphene. The 2D-band in pristine graphene is associated with a second-order double resonance (DR) mode (**Figure 2.1B**).[39a] The Raman processes leading to the 2D-band are displayed in **Figure 2.1E and 2.1F**. The DR process is activated by an intervalley scattering of the excited electron by a combination of two TO phonons near the K point and then a recombination near K′ points.[39a] The shape of the 2D-band is sensitive to the number of layers of graphene. Like the 2D-band, the D-band also involves a DR process. However, it is activated by defects such as sp^3-defects, vacancy sites or grain boundaries. As shown in **Figure 2.1D**, an electron is inelastically scattered by a TO phonon to the K′ point and then turns to be elastically back-scattered to the K point by a defect. The defect density in graphene can be estimated qualitatively by the intensity of the D-band. The D+D″ band originates from an intervalley scattering induced by phonons from TO (D) and LA (D″) branches.[33] In comparison with the 2D band, the D+D″ band shows a negative curvature because of longitudinal acoustic (LA) dispersion near the K point.
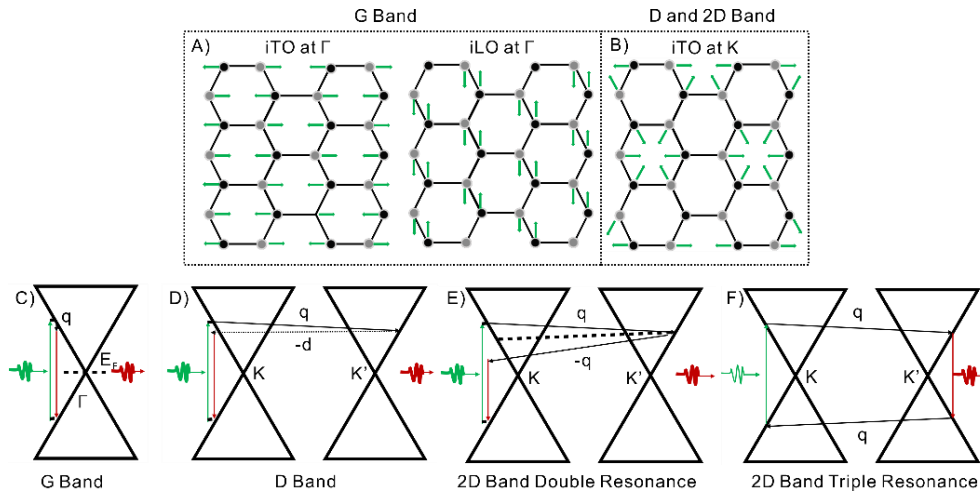

Figure 2.1. A) and B) Vibration modes of G (iTO and iLO phonons at Γ-point), D (iTO phonon at the K-point) and 2D (iTO phonon at the K-point) bands in graphene and corresponding raman processes. The i means in-plane. [39]

2.2 Microscopy Methods

2.2.1 Atomic force microscopy

Atomic force microscopy (AFM) is an imaging technique by scanning a probe over a sample surface. It can capture topographical morphologies for test samples (**Figure 2.3.1A**). The AFM is well suitable for characterizing surface morphology, film thickness, roughness and uniformity. The tapping mode has been widely used to explore morphological structures of graphene-based materials because it can avoid friction, adhesion and electrostatic forces by oscillating the sharp probe.[40] For monolayer exfoliated graphene, the average thickness varies between 0.4 nm and 0.9 nm.[41] In contrast, the thickness of

chemically-derived graphene like GO is about 0.8-1.2 nm due to bilateral oxygen functional groups at the carbon plane (**Figure 2.3.1B**).
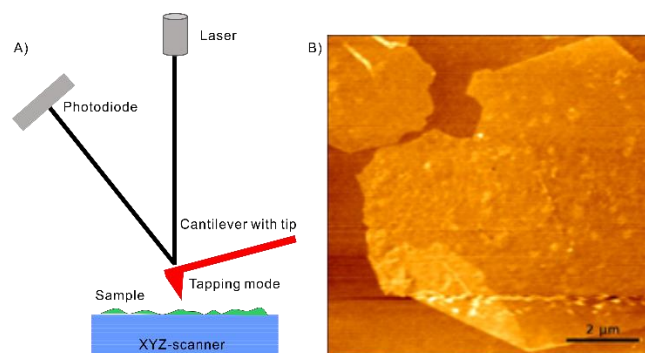

Figure 2.3.1. A) AFM measurement with tapping mode. B) An AFM image of monolayer GO flake.

2.2.2 Scanning tunnelling microscopy

The scanning tunnelling microscopy (STM) is an electron microscope with an atomic-scale resolution. The principle of STM is based on the quantum mechanical effect of tunneling. When a metallic tip (W or Pt/Ir) is in close proximity (a few Å) to a surface, a small applied bias between the tip and surface permits electrons to tunnel through a thin vacuum barrier.[42] Scanning tunnelling spectroscopy (STS), an extension of STM, is obtained from different positions of the STM tip above the sample, which can provide the local density of states (LDOS) of samples by measuring electron tunneling current as a function of electron energy (termed as *I-V* curve). The STM and STS have been used extensively for exploring surface morphologies and related electronic states in graphene-based systems. Recep Zan et al. reported a topographic image of suspended single-layer graphene that displays the hexagonal honeycomb structure with an interatomic distance of 1.4Å.[43] Some STM studies of graphene on different surfaces such as SiO$_2$, and metal (Ru, Ir) have been performed.[44] In these researches, structural features associated with the electronic properties of graphene were strongly influenced by the interaction between the graphene layer and the underlying surface. Thus, it is desirable to explore and discover new substrates to improve the quality of graphene. Régis Decker et al. reported a STM study of the topographic and local electronic structure of graphene monolayers placed on top of hexagonal boron nitride (h-BN) substrates.[45] Their results demonstrated that h-BN/graphene improves graphene stability, roughness, and intrinsic local electronic properties compared to SiO$_2$/graphene.
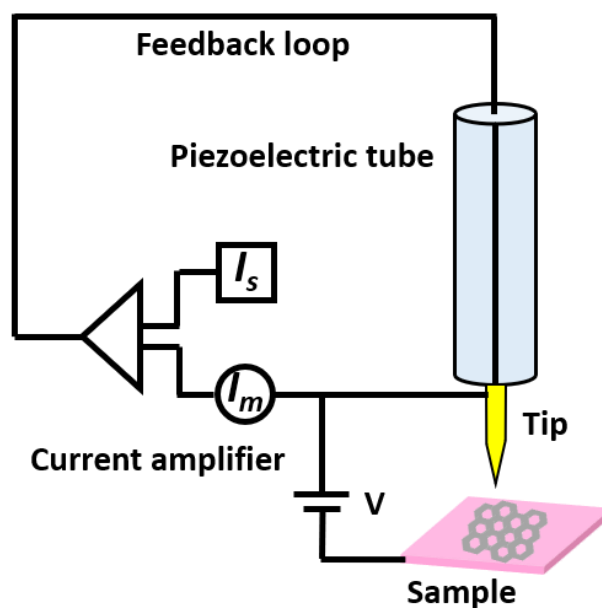
Figure 2.2.2. Schematic diagram of an STM.

2.3 Langmuir-Blodgett technique

The Langmuir-Blodgett (LB) technique is a technique for the self-assembly of amorphous molecules or flakes into highly ordered thin-films at the air-water interface, as shown in **Figure 2.3A**. The liquid-air interface can work as a platform to assemble GO sheets because of the amphiphilic property and surface chemistry of the GO. The morphology of assembled GO flakes can be manipulated by surface pressure, concertation and the pH value of GO solution (**Figure 2.3B**). In addition, the LB technique can achieve controllable deposition of GO sheets with homogeneity over a large area by a layer-by-layer manner, thus allowing the development of GO materials in applications of flexible electronics, solar cells and chemical- or bio-sensors.[46]
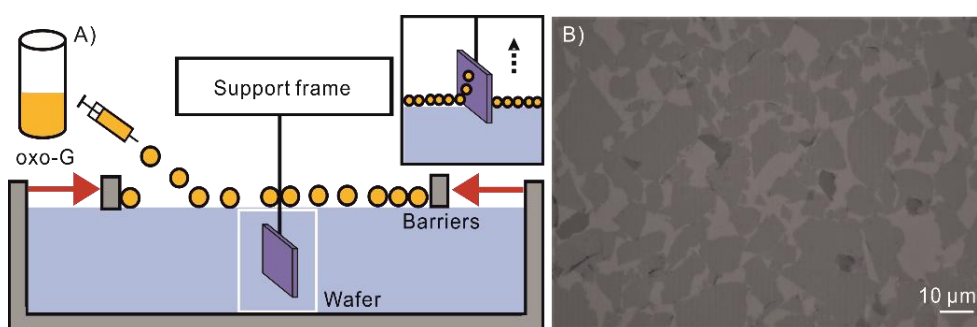
Figure 2.3. A) Schematic illustration of LB assembly of oxo-G single layers. B) Optical image of collected oxo-G flakes on a silicon wafer with 300 nm SiO_2 surface.

2.4 Dry transfer technique for building up two-dimensional based heterostructures

A transfer system is used to stack a stamp onto a substrate. The complete system contains an optical microscope with different objectives (5x, 10x, 20x and 100x), a mechanical stage with high resolution micromanipulators and a heater, as shown in **Figure 2.4.1**. The transfer stage can be moved in X, Y and

Z directions, which allows accurately aligning flakes during the process of building-up 2D-based heterostructures.

Figure 2.4.1. Setup of the 2D-dry transfer system.

The detailed dry-transfer procedure for building-up the r-oxo-G/h-BN heterostructure is depicted in **Figure 2.4.2**. First, the monolayer r-oxo-G flake on a thin Polydimethylsiloxa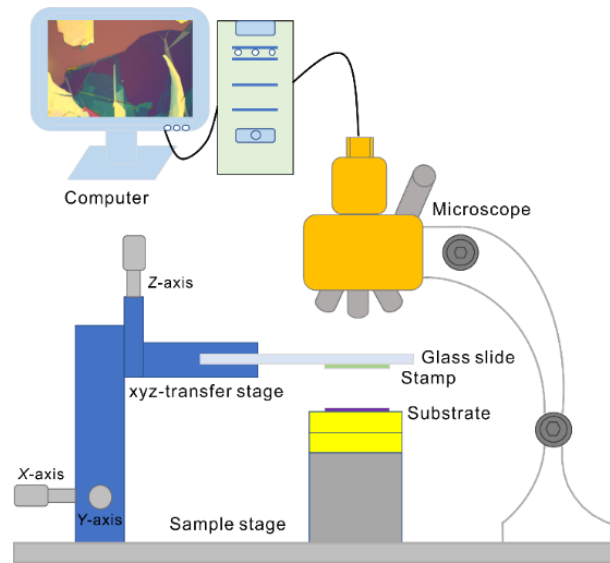n (PDMS, X$_4$, Gelpak) film was transferred onto a glass slide coated with a thick PDMS layer, an adhesive tape layer and an elvicate (2550) layer, respectively. The exfoliated thin h-BN flake on a Si/300 nm SiO$_2$ substrate worked as a target spot. Then, an optical microscope was employed to correct positions of the r-oxo-G onto the h-BN flake to make sure the two flakes overlap. By screwing the Z-axis of transfer stage (**Figure 2.4.1**), the glass slide was approaching the h-BN flake. The stacked wafer and the glass slide were heated at 100 °C for few minutes. Then, the glass slide was picked up rapidly. After that, the h-BN/r-oxo-G heterostructure covered with elvicate was transferred onto the wafer. By dissolving the elvicate in acetone and isopropanol, the clean h-BN/r-oxo-G heterostructure was obtained.
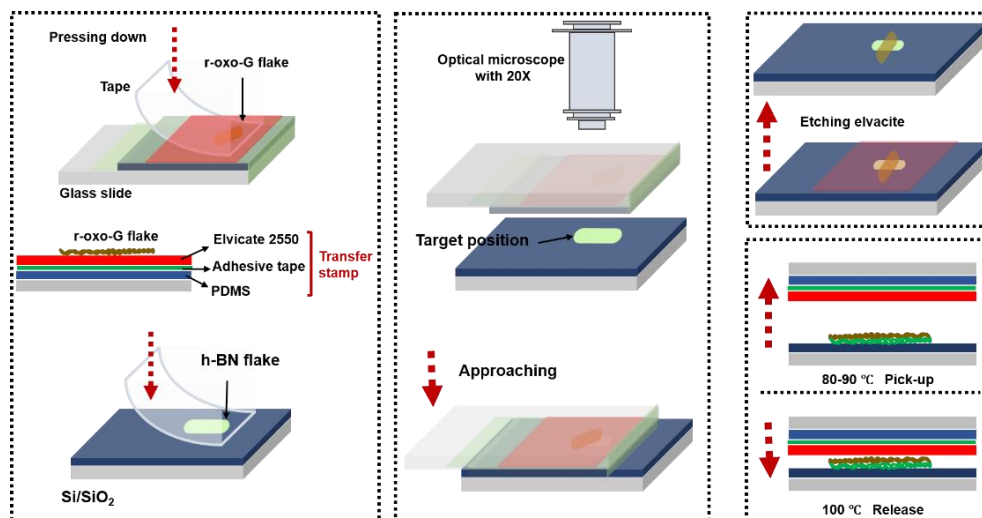
Figure 2.4.2. Schematic illustration of the preparation of the h-BN/r-oxo-G heterostructure.

2.6 Device fabrication

2.6.1 Electron beam lithography

Electron beam lithography (abbreviated as EBL), developed in the late 1960s, is a nanofabrication technique for writing micro- or nanometer-sized structures on various substrates. An EBL system usually contains a chamber, an electron gun and a column for controlling the status of the e-beam. Its working principle is based on a scanning electron microscope (SEM). However, unlike the SEM scanning for collecting secondary electrons to form images, in an EBL, the e-beam is patterned onto the sample according to the instructions from an image generator. In detail, scanning an e-beam across a surface covered with an electron-sensitive resist changes the solubility of resist, resulting in selectively etching either exposed or non-exposed regions of the resist by developing. Polymethylmethacrylate (PMMA) is the most common positive resist, which can be removed by solution mixtures of isopropanol (IPA) and methyl isobutyl ketone (MIBK) in a ratio of 3:1. The largest advantage of the EBL is its extremely high resolution. Considering the proximity effect (the forward and backward scattering of the electrons in the resist), the resolution of EBL in real cases is restricted to about 10 nm.
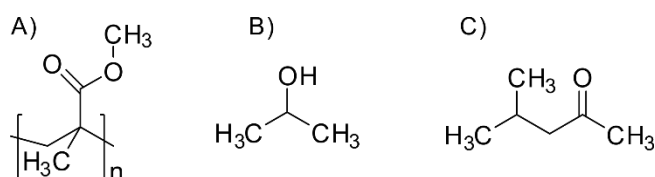
Figure 2.6.1. Chemical structure of PMMA, IPA and MIBK.

2.6.2 Gold evaporator

Thermal evaporation is a method of thin-film deposition. The process involves heating a solid material in a vacuum chamber (lower than 10^{-6} Torr) at a certain temperature. The evaporated vapor stream traverses the chamber and deposit onto the substrate. In order to improve adhesion between gold (Au) and the surface of SiO_2, a thin chromium (Cr) layer is deposited first. The thin-film with Cr/Au is anisotropic alloy deposited on the whole substrate. Thus, lift-off method with acetone is used for patterning the gold interconnects on a substrate.

Figure 2.6.2. An optical microscope image of Cr/Au (5 nm/ 70 nm) contacts on single layer reduced-oxo-G flake.

17

2.7 Electrical transport measurements

The fabricated graphene-based field-effect transistors (FETs) are electrically characterized in a typical two-probe back-gate transport setup shown in **Figure 2.7**. In detail, a Keithley 2450 electrome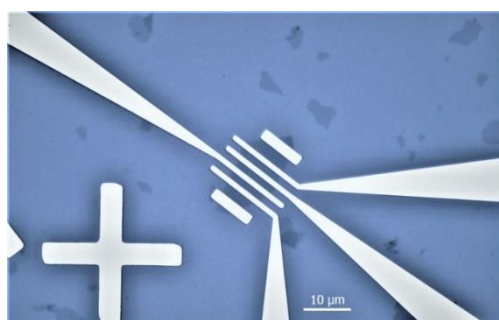ter is used to supply drain-source voltage source (V_{DS}) and the other Keithley 2450 is used as the gate-source voltage (V_{GS}). Both Keithley 2450 are connected to a computer for collecting data. Before measurements, the samples are adhered to a chip carrier by silver paste, and then the electrode pads are bonded with gold wires. Tuning of transport properties of samples is accomplished by applying a gate voltage to a dielectric layer (such as SiO_2), which leads to changes of carrier concentration of samples as conductive channels. There are two ways to characterize a FET device: output and transfer curves. The output characteristic (I_{DS}-V_{DS}) is measured by recording drain-source current (I_{DS}) as a function of the supplied drain-source voltage (V_{DS}) at a constant gate voltage (V_G). Linear responses of I_{DS}-V_{DS} means ohmic contacts. The transfer characteristic (I_{DS}-V_G) plots the I_{DS} as a function of the V_G at a certain V_{DS}. The I_{DS}-V_G curve is used to determine the carrier mobility of test samples.
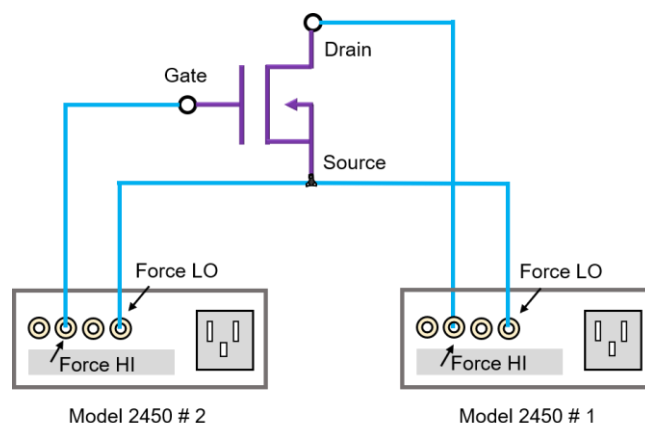

Figure 2.7. Transport test configuration for FETs.

3. Main contributions

3.1 The electrical properties of reduced oxo-G based materials

3.1.1 Effects of substrates on the electrical properties of monolayer reduced oxo-G

The oxygen-containing groups on the graphene basal plane, rims of flakes and holes make GO a p-type semiconductor with a typical resistance of 10^{10}-10^{13} Ω sq^{-1} and a band gap of about 2.2 eV.[47] The reductive defunctionalization of GO leads to a certain type of graphene (G), often named reduced GO (r-GO). In general, the reduction of GO to r-GO leads to a transition from a semi-conductive material to a semi-metal.[5] Mobility values were determined in field effect transistor (FET) devices.[29a] Generally, the quality of graphene strongly depends on the integrity of the hexagonal carbon lattice. Thus, mobility values of 10^{-3} and up to 10^3 cm^2 V^{-1} s^{-1} were reported with the resistance fluctuating between 10^3 and 10^6 Ω sq^{-1}.[23, 35-36, 48] We reported on the highest mobility values of chemically reduced oxo-G (with about 0.02% of lattice defects) of 1,000 cm^2 V^{-1} s^{-1}, determined by Hall-bar measurements at 1.6 K.[10] Because of impurity scattering, remote phonons scattering, charge traps, and surface roughness on adjacent dielectric oxide layers, exhibiting electronic device performances of graphene on substrates are

18

far lower than that of the intrinsic graphene. However, hexagonal boron nitride (h-BN) has been proved to be an excellent substrate for matching graphene-based materials owing to its atomic flatness, chemical inertness and electronic insulation due to a bandgap of ~5.5 eV.[49] Up to now, most studies with graphene deposited on h-BN were restricted to measurements with virtually defect-free graphene.[50] To the best of the authors knowledge, no studies reported transport measurements based on single layers of GO or oxo-G on h-BN substrates. no studies are reported with graphene derived from GO or oxo-G on single-layer level. Recently, we found that chemical reactions can be selectively conducted close to the rims of defects.[51] However, before functionalized devices can be studied, the lack of knowledge on the ambient environment device performances of graphene with defects and the influence of substrates must be addressed.

Therefore, we fabricated the devices composed of the reduced-oxo-G with 0.5% defects, termed as $^{0.5\%}$G, partially deposited on SiO_2 (SiO_2/ $^{0.5\%}$G) and h-BN (h-BN/ $^{0.5\%}$G). Areas of the same flake on both materials are used to ensure reliable measurements and to prove that the results stem from substrate rather than from the difference between devices. The h-BN/$^{0.5\%}$G structure has important applications in highly sensitive chemically-derived graphene based sensors.

Title:	Influence of SiO_2 or h-BN substrate on the room-temperature electronic transport in chemically derived single layer graphene
Authors	Zhenping Wang, Qirong Yao, Yalei Hu, Chuan Li, Marleen Hußmann, Ben Weintrub, Jan N. Kirchhof, Kirill Bolotin, Takashi Taniguchi, Kenji Watanabe and Siegfried Eigler
To be cited as	RSC Advances **2019**, 9, 38011-38016. https://doi.org/10.1039/C9RA09197A
Detailed scientific contribution	The concept of this manuscript was proposed by Zhenping Wang and Prof. Dr. Siegfried Eigler. All samples used in the manuscript were prepared by Zhenping Wang. STM characterization was conducted by Dr. Qirong Yao. All other characterizations are performed by Zhenping Wang. The H-BN material was provided by Prof. Dr. Takashi Taniguchi and Prof. Dr. Kenji Watanabe. The 2-dimentional transfer platform is provided by Prof. Dr. Kirill Bolotin. The problems encountered throughout the experiment were assisted by Yalei Hu, Chuan Li, Marleen Hußmann, Ben Weintrub, Jan N. Kirchhof and Kirill Bolotin. The manuscript was written by Zhenping Wang. The revision of the manuscript was assisted by Prof. Dr. Siegfried Eigler and Prof. Dr. Kirill Bolotin.
Estimated own contribution	~ 90%

Supporting Information

Influence of SiO$_2$ or h-BN substrate on the room-temperature electronic transport in chemically derived single layer graphene

Zhenping Wang, [a] Qirong Yao, [b] Yalei Hu, [a] Chuan Li, [b] Marleen Hußmann, [a] Ben Weintraub, [c] Jan Kirchhof, [c] Kirill Bolotin, [c] Takashi Taniguchi[d], Kenji Watanabe[d] and Siegfried Eigler[a*]

Experimental Section

Synthesis of oxo-G

Oxo-G was prepared by the optimized oxidation of graphite at low temperature (< 4 °C), using potassium permanganate as oxidant in sulfuric acid, as reported before by our group.[1]

Langmuir-Blodgett films of oxo-G

Flakes of oxo-G were deposited onto the Si/SiO$_2$ substrate by Langmuir–Blodgett technique[2] (LB, Kibron µtrough, 3 mN m^{-1} with the surface tension of water as reference value of 72.8 mN m^{-1}). Reduction was performed by vapor of hydriodic acid and trifluoroacetic acid (1/1 mixture by volume) at 80 °C (10 min). Subsequently, the surface of graphene was cleaned with doubly distilled water (Carl Roth) to remove iodine species, which are adsorbed on $^{0.5\%}$G flakes.

Fabrication of h-BN/$^{0.5\%}$G heterostructures device

In order to make h-BN/$^{0.5\%}$G heterostructures, a h-BN flake (obtained from Taniguchi group, Japan) was mechanically exfoliated onto the Si/SiO$_2$ substrate by scotch tape method.[3] The $^{0.5\%}$G flake was transferred onto Si/SiO$_2$/h-BN surfaces with Polydimethysiloxane (PDMS, Gel-pack) as a carrier.[4] Then, the h-BN/$^{0.5\%}$G heterostructure with the same monolayer $^{0.5\%}$G flake partially covered on SiO$_2$ and h-BN surfaces was

finished. Patterning of the electrode structure was achieved by standard electron beam lithography processing (Raith PIONEER TWO). The 5/70 nm Cr/Au electrodes were deposited by thermal evaporation (Kurt J. Lesker NANO 36).

Measurements

Optical imaging was performed using a Nikon LV100ND. Scanning tunnelling microscopy (STM) and Scanning tunnelling spectroscopy (STS) were performed with an ultra-high vacuum ($< 10^{-10}$ mbar) STM (Omicron-STM1). AFM characterization was performed using a JPK Nanowizzard 4 atomic force microscope in tapping mode at room temperature. Statistical Raman spectroscopy was recorded using a confocal Raman microscope (Horiba Explorer, 532 nm excitation wavelength). Electrical measurements were carried out at ambient conditions using a probe station with micromanipulated probes and two source- measurement units (Keithley 2450). In addition, comparing experiments were carried out at vacuum (HI-CUBE) using Lakeshore probe station.
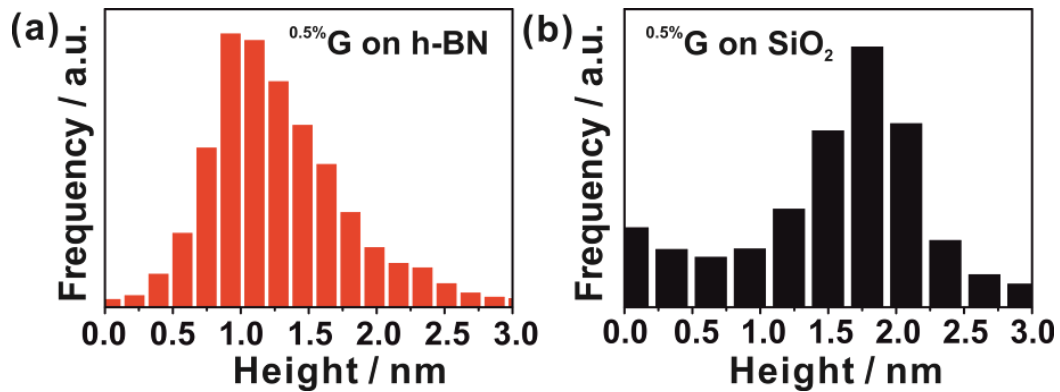
Results

Fig. S1. (a) and (b) Histogram of the height distribution measured by AFM for the $^{0.5\%}$G on h-BN and SiO$_2$.
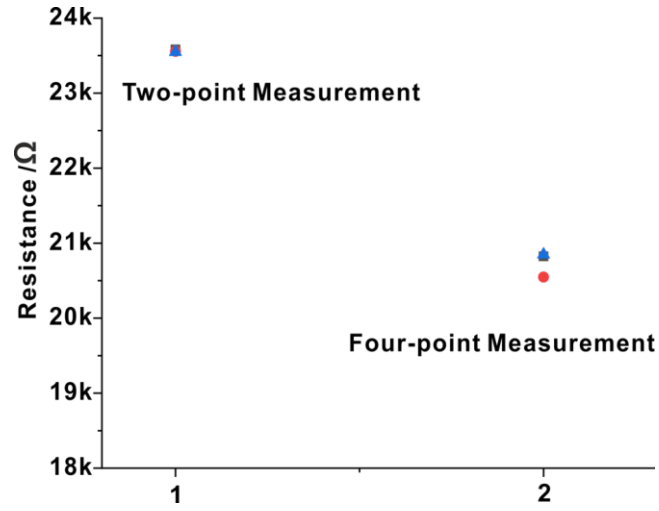
Fig. S2. Measurements of resistance of monolayer $^{0.5\%}$G in two-point and four-point configuration, respectively.
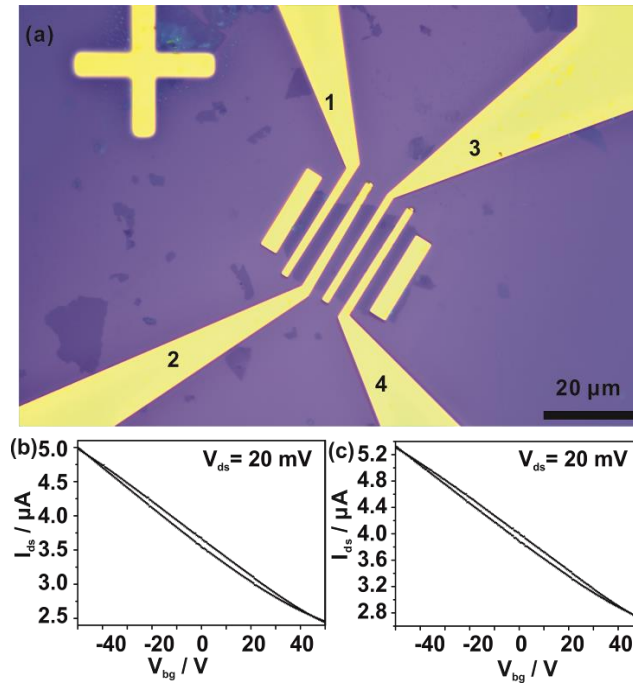
Fig. S3. (a) Optical image of the fabricated monolayer $^{0.5\%}$G device with back-gate. (b) Electrodes 1 and 2 were measured for transfer characteristics for the $^{0.5\%}$G on SiO_2. Channel length and width between 1 and 2 is 3 µm and 24 µm, respectively. (c) Electrodes 2 and 3 were measured for transfer characteristics for the $^{0.5\%}$G on SiO_2. Channel length and width between 2 and 3 is 3 µm and 24 µm, respectively.
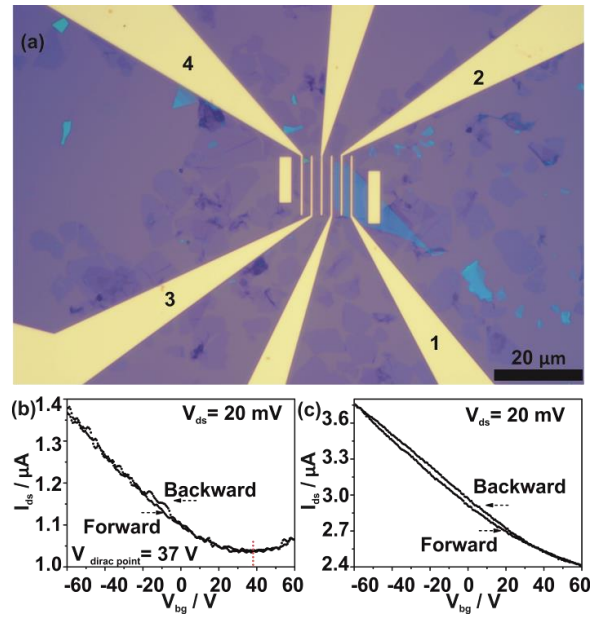
Fig. S4. (a) Optical image of the fabricated h-BN/$^{0.5\%}$G and SiO$_2$/$^{0.5\%}$G heterostructures device with back-gate. (b) Electrodes 1 and 2 were measured for the $^{0.5\%}$G on h-BN. (c) transport results.
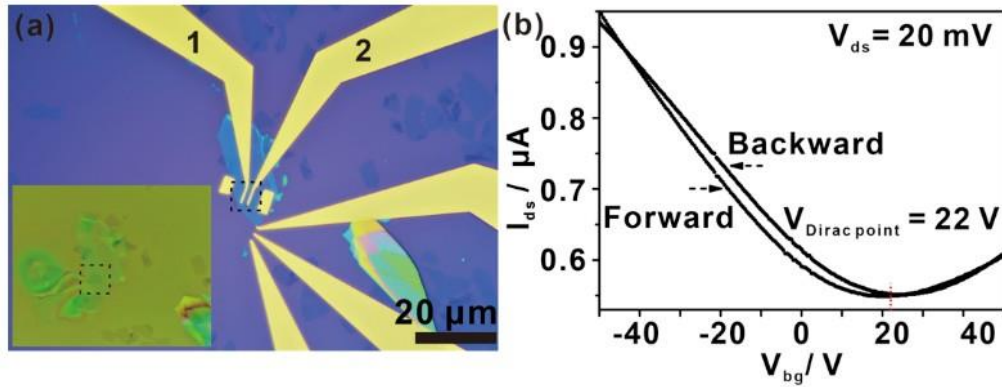
Fig. S5. (a) Optical image of the fabricated h-BN/$^{0.5\%}$G (the $^{0.5\%}$G is completely deposited onto the h-BN) heterostructures device. Channel length and width is 1.5 µm and 5 µm, respectively. The inset shows that the $^{0.5\%}$G flake is completely deposited on h-BN, which can fully avoid the effect of SiO$_2$ substrate on the electrical transport properties of the $^{0.5\%}$G. (b) Transfer characteristics for the $^{0.5\%}$G on h-BN.
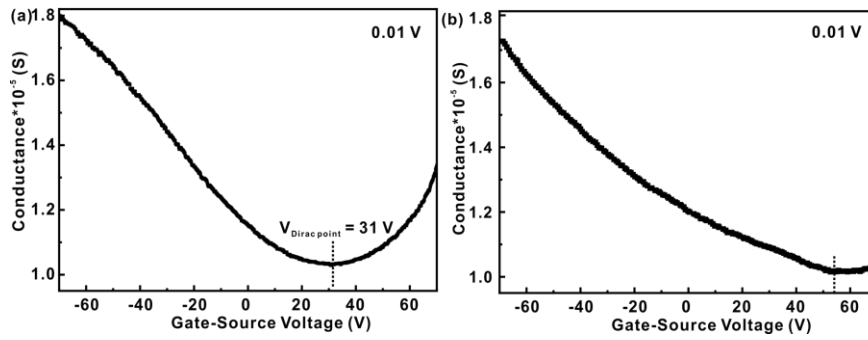
Fig. S6. Transfer curves of the reduced oxo-G with 0.8% defects in vacuum and air by two-probe configuration.

References

1. S. Eigler, M. Enzelberger-Heim, S. Grimm, P. Hofmann, W. Kroener, A. Geworski, C. Dotzer, M. Rockert, J. Xiao, C. Papp, O. Lytken, H. P. Steinrück, P. Müller and A. Hirsch, Adv. Mater., 2013, 25, 3583-3587.

2. L. J. Cote, F. Kim and J. Huang, J. Am. Chem. Soc., 2009, 131, 1043-1049.

3. R. V. Noorden, Nature, 2012, 483, S32-S33.

4. X. Ma, Q. Liu, D. Xu, Y. Zhu, S. Kim, Y. Cui, L. Zhong and M. Liu, Nano Lett., 2017, 17, 6961-6967.

3.1.2 Effects of defects on the electrical properties of monolayer reduced oxo-G

In contrast to pristine graphene with carbon atoms arranged into a two-dimensional hexagonal lattice, oxo-G consists of abundant sp^3 hybridized carbon atoms, which are covalently bound to oxo-groups.[52] The sp^3-portion is between 4% and 60%, with variable functionality.[25] The oxo-addends are tentatively immobilized onto segregated carbon, which isolates intact nanometer-scale graphene domains into small islands.[53] The existence of surface oxo-groups has profound impacts on improving its hydrophilicity, chemical reactivity, catalytic activity, and optical properties, while the effect is detrimental for the electrical conductivity.[54] However, so far, no systematic investigation has been available relating the density of defects to the charge carrier mobilities at room temperature. Most reported values of carrier mobility values with a wide range from 10^{-3} to 10^3 cm^2 V^{-1} s^{-1} had been determined from multilayer thin films of reduced GO related materials with unknown thickness and qualities.[23, 34a, 35, 55] Moreover, taking various synthetic procedures of oxo-G and non-standard transport measurements into consideration, there exist more uncertainties.

Here, we investigated the electrical performances of the reduced single-layer oxo-G with defects from 0.1% to 1.5%. The Raman characterization was used for quantifying the structural defects. Our research results provide a correspondence relationship between structural defects and their related electrical properties. The fundamental findings reported here can explain the generally diverging results often reported for reduced graphene oxide used in applications.

Title	Room-temperature transport properties of graphene with defects derived from oxo-graphene
Authors	Zhenping Wang, Qirong Yao and Siegfried Eigler
To be cited as	Chem. Eur. J. **2020**. *26*, 1-7. https://doi.org/10.1002/chem.201905252
Detailed scientific contribution	The concept of this manuscript was proposed by Zhenping Wang and Prof. Dr. Siegfried Eigler. All samples used in the manuscript were prepared by Zhenping Wang. Except for the STM characterization conducted by Dr. Qirong Yao, all other characterizations were performed by Zhenping Wang. The manuscript was written by Zhenping Wang. The revision of the manuscript was assisted by Prof. Dr. Siegfried Eigler.
Estimated own contribution	~ 90%

Supporting Information

Room-Temperature Transport Properties of graphene with Defects Derived from Oxo-Graphene

Zhenping Wang,[a] Qirong Yao,[b] and Siegfried Eigler*[a]

[a]   M. Sc. Z. Wang, Prof. Dr. S. Eigler
      Freie Universität Berlin, Institute for Chemistry and Biochemistry, Takustraße 3, 14195 Berlin, Germany
      E-mail: siegfried.eigler@fu-berlin.de
[b]   Dr. Q. Yao
      Physics of Interfaces and Nanomaterial, University of Twente,
      Enschede, 7500 AE, The Netherlands

1. Calculation of the defect density from Raman spectra

The calculation of the defect density is based on the model introduced and interpreted by Lucchese and Cançado and interpretation by Englert et al.[27] The detailed calculation processes are based on the following three equations.

$$v\frac{I_D}{I_G} = C_A \frac{r_A^2 - r_S^2}{r_A^2 - 2r_S^2}[e^{-\pi r_S^2 \omega/L_D^2} - e^{-\pi(r_A^2 - r_S^2)r_S^2/L_D^2}] \tag{1}$$

$$C_A = (160 \pm 48)E_L^4 \tag{2}$$

$$N_C = 2L_D^2/A_{cell} \tag{3}$$

Here the r_A and r_S are length scales that determine the region induced by the D band scattering. The C_A is related to the ratio between the efficiency of optical phonons between K and Γ. The E_L is the excitation energies (E_L = 2.33 eV, λ_L=532 nm). The N_C is the number of carbon atoms in graphene domains. The A_{cell} is a graphene unit cell, where the A_{cell} = 0.246^{2}sin (60°) = 0.05239 nm^2. The lines in Figure S1 are fitting curves following the three equations.
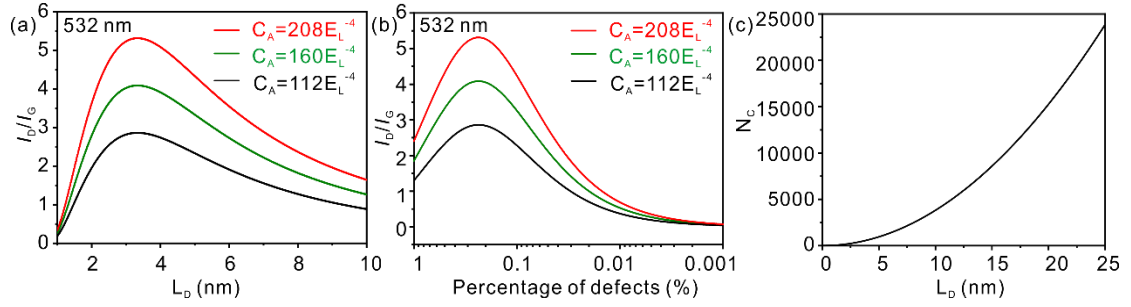

Figure S1. (a) I_D/I_G as s function of L_D. (b) I_D/I_G as s function of percentage of defects (%). The red, green and black curves are given by C_A=208×E_L^{-4}, C_A=160× E_L^{-4} and C_A=112× E_L^{-4}, respectively, where the excitation energies E_L of 532 nm laser is 2.33 eV. (c) The relation between N_C and L_D.

2. The resistance values measured by room-temperature two-probe configuration are summarized in the Table S1:

Table S1. Resistance values measured by room-temperature two-probe configuration are summarized.

Sample	$G_{0\%}$	$G_{0.2\%}$	$G_{0.4\%}$	$G_{0.5\%}$	$G_{0.9\%}$	$G_{1.5\%}$
resistance	0.9 kΩ	2.0 kΩ	7.9 kΩ	5.1 kΩ	131.7 kΩ	434.1 kΩ
Channel length	1.5 μm	2 μm	4 μm	2 μm	4 μm	5 μm

3. Room-temperature transfer characteristics of graphene transistors with densities of defects of 0%, 0.2%, 0.4%, 0.5%, 0.9% and 1.5%, respectively. The gate voltage is swept continuously from -50 V to 50 V and back to -50 V.
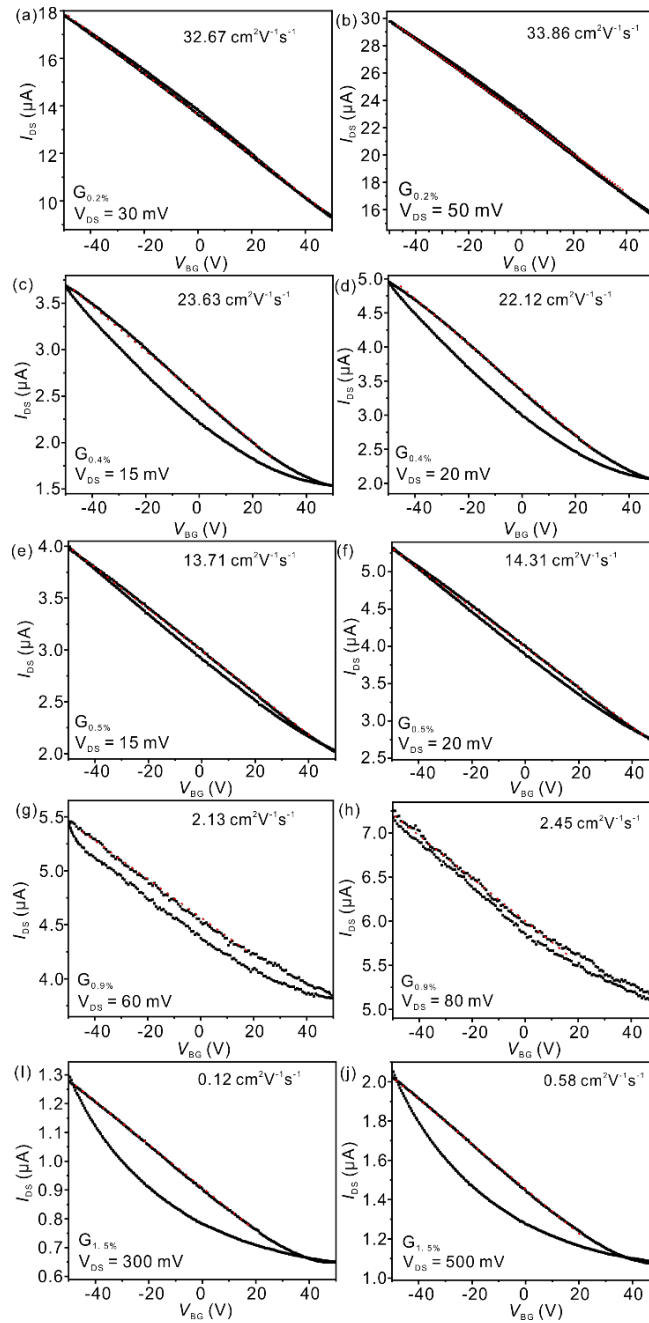
Figure S2. Room-temperature transfer characteristics of graphene transistors with densities of defects of 0%, 0.2%, 0.4%, 0.5%, 0.9% and 1.5%, respectively

References

[1] a) L. G. Cançado, A. Jorio, E. H. M. Ferreira, F. Stavale, C. A. Achete, R. B. Capaz, M. V. O. Moutinho, A. Lombardo, T. S. Kulmala and A. C. Ferrari, *Nano Lett.* **2011**, *11*, 3190-3196; b) J. M. Engiert, P. Vecera, K. C. Knirsch, R. A. Schäfer, F. Hauke and A. Hirsch, *ACS Nano* **2013**, *7*, 5472-5482; c) M. M. Lucchese, F. Stavale, E. H. M. Ferreira, C. Vilani, M. V. O. Moutinho, R. B. Capaz, C. A. Achete and A. Jorio, *Carbon* **2010**, *48*, 1592-1597; d) A. C. Ferrari and D. M. Basko, *Nat. Nanotechnol.* **2013**, *8*, 235-246; e) L. G. Cançado, M.
G. da Silva, E. H. M. Ferreira, F. Hof, K. Kampioti, K. Huang, A. Penicaud, C. A. Achete, R. B. Capaz and A. Jorio, *2D Mater.* **2017**, *4*, 025039-025050.

3.2 The structure evolution of oxo-G during thermal decomposition

Chemically processed oxo-G with a degree of oxo-functionalization of about 4% (abbreviated as oxo-$G_{4\%}$) bears defect-free areas with diameters of about 10 nm in average.[21] After thermal processing up to 175 °C, the oxo-$G_{4\%}$ disproportionates and bears preserved graphene domains with diameters of about 3 nm, next to few-atom large vacancy defects and holes with diameters around 1-2 nm.[21] Oxo-G with a typical degree of functionalization of 60% (oxo-$G_{60\%}$) endures a density of defects of about 2% after annealing.[19, 25] However, deep knowledge about the atomic structures and defects between oxidized and deoxygenated states in oxo-G are ambiguous. In particular, it is still not clear how the structure of GO or oxo-$G_{60\%}$ evolves during thermal processing.

Here, we present the structure evolution and related transport properties of oxo-G on the single layer level by gradual thermally induced disproportionation. Our study gave a deep insight of the structure change of the thermal disproportionation of oxo-G. In particular, the formation of holes and sp^3-stacked regions potentially play a significant role for chemical reactions used to post-functionalize materials. Moreover, graphene-2D-diamond-based materials or bottom-up synthesized molecular materials with a tunable band-gap might be discovered in the future.

Title	Identification of Semiconductive Patches in Thermally Processed Monolayer Oxo-Functionalized Graphene
Authors	Zhenping Wang, Qirong Yao, Christof Neumann, Felix Börrnert, Julian Renner, Ute Kaiser, Andrey Turchanin, Harold J. W. Zandvliet and Siegfried Eigler
Under review	Angew. Chem. Int. Ed
Detailed scientific contribution	The concept of this manuscript was proposed by Zhenping Wang and Prof. Dr. Siegfried Eigler. All samples used in the manuscript were prepared by Zhenping Wang. STM characterization was conducted by Dr. Qirong Yao in Prof. Harold J. W. Zandvliet group. XPS characterization was conducted by Christof Neumann and Dr. Felix Börrnert in Prof. Dr. Andrey Turchanin group. TEM was conducted by Julian Renner in Prof. Dr. Ute Kaiser group. The remaining other characterizations are performed by Zhenping Wang. The manuscript was written by Zhenping Wang. The revision of the manuscript was assisted by Prof. Dr. Siegfried Eigler, Prof. Harold J. W. Zandvliet, Prof. Dr. Andrey Turchanin and Prof. Dr. Ute Käiser.
Estimated own contribution	~ 70%

Identification of Semiconductive Patches in Thermally Processed Monolayer Oxo-Functionalized Graphene

Zhenping Wang, [a] Qirong Yao, [b] Christof Neumann, [c] Felix Börrnert, [d] Julian Renner, [d] Ute Kaiser, [d] Andrey Turchanin, [c] Harold J. W. Zandvliet [b] and Siegfried Eigler*[a]

Abstract: The thermal decomposition of graphene oxide (GO) is a complex process at the atomic level and not fully understood. Here, a subclass of GO, oxo-functionalized graphene (oxo-G) was used to study its thermal disproportion. We present the impact of annealing on the electronic properties of a monolayer oxo-G flake and correlated the chemical composition and topography corrugation by two-probe transport measurements, XPS, TEM, FTIR and STM. Surprisingly, we found that oxo-G, processed at 300 °C, bears C-C sp^3-patches and possibly C-O-C bonds, next to graphene domains and holes. It is striking that those C-O-C/C-C sp^3-separated sp^2-patches with few nanometers in diameter possess semiconducting properties with a bandgap of about 0.4 eV. We propose that sp^3-patches confine conjugated sp^2-C what leads to the local semiconductor properties. Accordingly, graphene with sp^3-C in double layer areas is a potential class of semiconductors and a potential target for future chemical modifications.

Graphene oxide (GO) is described as a derivative of graphene obtained by oxidation of graphite or graphene.[1] The sp^2-bonded carbon atoms, which are arranged in a honeycomb lattice are partially decorated with oxygen-containing species.[2] Tuning the sp^2/sp^3 ratio in the GO materials provides pathways to design diverse graphene derivatives with intriguing physicochemical properties including surface modifiability,[3] tunable bandgap,[4] and variable luminescence[5] toward the extensive applications in sensing based on electronic and luminescent devices.[6] However, because of the polydisperse structure of GO, the structural model remains generalized, in particular with respect to the regiochemistry.[2c, 7] During the preparation of GO via oxidation approaches such as Hummers' method,[8] over-oxidation violently disintegrates the sp^2-carbon lattice and results in either vacancy defects on the scale of 10 nm at best or flake-like amorphous carbon.[9] The size of defect-free graphene patches in reduced GO is about 1 nm.[10] Over-oxidation during the preparation of GO was identified as reason for the ruptured graphene lattice in GO due to the loss of carbon via formation of CO_2.[11] As verified by Dimiev et al. using Hummers' method in first approximation, one CO_2 molecule is formed from 20 carbon atoms.[12] Recently, we found that kinetically controlled oxidation procedures can effectively hinder the over-oxidation, still performing the oxidation by harsh oxidants such as potassium permanganate in sulfuric acid or sodium chlorate in nitric acid.[13] The obtained GO materials, which are a sub-class of GO, are termed as oxo-functionalized graphene (oxo-G). The oxo-G bears an intact carbon framework with densities of lattice defects of about 0.02% and 0.5%, respectively.[14] It was demonstrated that hydroxyl-, epoxy-, and organosulfate-groups decorate the carbon lattice on both sides of the basal plane and edge functional groups like carbonyl- and carboxyl-groups only play a minor role.[13]

The carbon lattice in oxo-G can be visualized by high-resolution transmission electron microscopy (TEM).[15] Chemically processed oxo-G with a degree of oxo-functionalization of about 4% (abbreviated as oxo-$G_{4\%}$) bears defect-free areas with diameters of about 10 nm in average.[16] After thermal processing up to 175 °C, the oxo-$G_{4\%}$ disproportionates and bears preserved graphene domains with diameters of about 3 nm, next to few-atom large vacancy defects and holes with diameters around 1-2 nm.[16] Oxo-G with a typical degree of functionalization of 60% (oxo-$G_{60\%}$) endures a density of defects of about 2% after annealing.[9, 14] Those defects can act as structural motifs and active sites for selective chemical functionalization.[17] So far, the vast majority of studies on GO or oxo-G based materials mainly focused on optimizing preparation and reduction methods,[18] understanding preparation protocols, reduction mechanism,[19], and applications.[20] However, deep knowledge about the atomic structures and defects between oxidized and deoxygenated states in oxo-G are ambiguous. In particular, it is still not clear how the structure of GO or oxo-$G_{60\%}$ evolves during thermal processing.

Here, we present the structure evolution and related transport properties of oxo-$G_{60\%}$ on the single layer level by gradual thermally induced disproportionation. The mobility values of monolayer oxo-G first increased with the release of adsorbed water, disproportionation up to 220 °C and then decreased due to the formation of holes and surprisingly discovered stacked regions bearing sp^3-C. By X-ray photoelectron spectroscopy (XPS), we identified a fraction of about 26% C-C sp^3 and about 3.4% C-O/C-OH/C-O-C, containing nanometer-sized sp^3-patches as visualized by TEM. Those regions turned out to be semiconducting with a bandgap of 0.4 eV, as revealed by scanning tunneling spectroscopy (STS). Thus, sp^2-C isolated by sp^3-patches is most likely responsible for the local semiconducting behavior (see **Scheme 1 and Figure 5**).

[a]   M. Sc. Z. Wang, Prof. Dr. S. Eigler
       Freie Universität Berlin, Institute for Chemistry and Biochemistry,
       Takustraße 3, 14195 Berlin, Germany
       E-mail: Siegfried.eigler@fu-berlin.de
[b]   Dr. Q. Yao, Prof. Dr. Ir. H. J. W. Zandvliet
       Physics of Interfaces and Nanomaterials, University of Twente,
       Enschede, 7500 AE, The Netherlands
[c]   M. Sc. C. Neumann, Prof. Dr. A. Turchanin
       Friedrich Schiller University Jena, Institute of Physical Chemistry,
       Lessingstraße 10, 07743 Jena, Germany
[d]   Dr. F. Börrnert, § M. Sc. J. Renner, Prof. Dr. U. Kaiser
       Universität Ulm, Zentrale Einrichtung Elektronenmikroskopie,
       Albert-Einstein-Allee 11, 89081 Ulm, Germany
       §Current address: Max-Planck-Institut für Mikrostrukturphysik,
       Weinberg 2, 06120 Halle, Germany

       Supporting information for this article is given via a link at the
       end of the document.
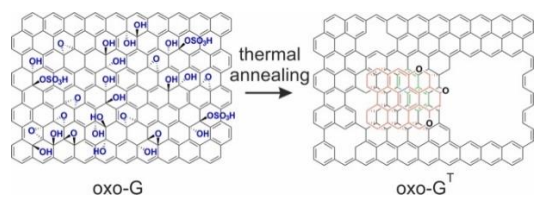
Scheme 1. Schematic illustration of the chemical structure of oxo-G and thermally-processed oxo-G (indicated as oxo-G^T). The latter results in the formation of holes and semiconducting sp^3-patches.

The starting oxo-G material used here possesses a degree of functionalization of about 60% sp^3-carbon, with hydroxyl-, epoxy-, and organosulfate groups as major functional groups.[21]

Temperature-dependent electrical transport properties were conducted by fabricating and analysing a monolayer oxo-G based field-effect transistor (FET) device (**Figure 1A**). The oxo-G device was fabricated by deposition of a monolayer oxo-G flakes on a heavily p-doped Si substrate with a 300 nm thick SiO$_2$ layer (Si/SiO$_2$) using Langmuir-Blodgett technique.[22] Then, gold contacts were deposited on top of the monolayer oxo-G flake by standard electron beam lithography (EBL) and gold evaporation. All electrical transport measurements were carried out by a two-probe configuration (see **Figure 1B**) at ambient conditions. The Si/SiO$_2$ substrate serves as a back-gate and gate dielectric. Different transport performances were obtained by iteratively heating the same device with the same oxo-G flake from room temperature (RT) to 300 °C. All transfer characteristics (I_{ds}-V_{bg}) reveal a typical p-type

behavior (**Figure 1C-J**). The large hysteresis between forward and reverse sweeps are induced by trapped charges.[23] The resistance and charge carrier mobility are extracted from the transport curves **Figure 1C-J**. As depicted in **Figure 1K**, on-resistance of oxo-G FET at V_{ds} = 0.5 V and V_{bg} = 0 V decreases from 5.3×10^8 Ω to 3.3×10^5 Ω. Evolution of the resistances reveals that the oxo-G undergoes an insulator to conductor transition with a partial restoration of sp^2-carbon lattices in the oxo-G flake by thermal processing. The change of hole mobilities (μ_h) displays an inverted parabola shape. The μ_h of the untreated monolayer oxo-G is 0.004 cm^2 V^{-1}s^{-1} with consistently matching its insulating feature. After thermal annealing up to 100 °C, the μ_h increases by an order of magnitude. This is because most of polar adsorbents like water or oxygen molecules desorbed from the oxo-G surface, as we identified before by thermogravimetric analysis.[11] In addition, some decomposition of organosulfate groups takes place.[24] But overall, the carbon skeleton of the oxo-G keeps relatively intact until 100 °C.[25] Then, significant increase of the μ_h is observed between 140 °C and 220 °C. It can be deduced that the main deoxidation process occurs at this stage, which is accompanied by formation of π-conjugated domains, in addition to vacancy defects, small holes and CO$_2$, as evidenced for oxo-G$_{4\%}$.[16] The maximum μ_h of about 0.3 cm^2 V^{-1}s^{-1} is obtained from oxo-G$^{220°C}$, which indicates the maximized sp^2 graphene structures in oxo-G$^{220°C}$. In contrast, further annealing at higher temperature results in decreased μ_h values. These results clearly suggest the limited restoration of the graphene domains and irreversible structural decays of oxo-G induced by the thermal processing.
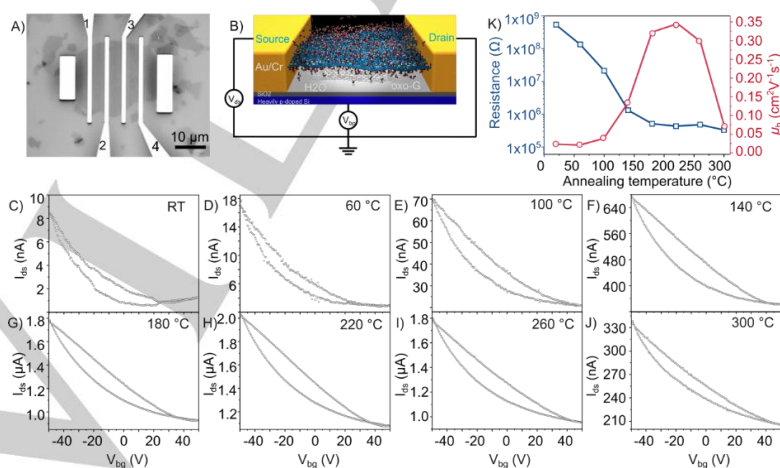

Figure 1. Electrical transport properties of a monolayer oxo-G-based FET device. A) An optical microscope image of a FET device with a monolayer oxo-G flake as a channel. The distance between electrodes is 3 μm and the length of every electrode is 20 μm. B) Schematic view of the monolayer oxo-G transistor with back-gate two-probe configurations. C) to J) Room-temperature transfer characteristics of the monolayer oxo-G treated by iteratively heating up to 300 °C. Metal contacts 1 and 2 were used as source and drain electrodes for the all measurements. K) Changes of resistance and mobility as a function of annealed temperature.

Next, XPS was conducted to analyse changes of chemical compositions in an iteratively annealed oxo-G sample. The high-resolution C 1s spectrum of oxo-G in **Figure 2A** displays a typical saddle-like pattern, which stems from significant oxidation in oxo-G. Four components assigned to C-C/C-H (51.8%, at 284.6 eV), C-O/C-OH/C-O-C (40.6%, at 286.7 eV), C=O (4.0%, at 287.7 eV) and COOH (2.5%, at 288.6 eV) are deconvoluted. The initial C/O ratio of oxo-G was 2.2 : 1. No significant change of the chemical composition is detected up to 100 °C (**Figure 2B** and **C**), in agreement with results of transport measurements. However, starting at 140 °C, the intensity of the peak assigned to C-O bonds weakens significantly. A distinction between sp^2- and sp^3-bonded C-C is observed and the sp^3-hybridized C-C bonds with 23.5% are detected (**Figure 2D**). The subsequent thermal treatments up to 300 °C do not induce an obvious change in chemical compositions (**Figure 2 E-H**) with the C-C sp^3 reaching about 26.1% and C-O/C-OH/C-O-C of 3.4%. The corresponding C/O ratios raise sluggishly from 4.6 to 7.5 (**Table S1**). Thus, considering the relatively stable chemical compositions but significantly weakened mobility values between 260 °C and 300 °C, we propose that structural rearrangements and formation of defects induced by thermal disproportionation further proceed. However, the role of evolving C-C sp^3-carbon, as detected by XPS remains unclear. To gain more precise structural insights into the thermally processed oxo-G, TEM investigations were conducted.[16, 21b, 26] The monolayer oxo-G flakes were deposited onto a TEM sample grid, which subsequently was annealed at 300 °C in vacuum to induce the thermal disproportionation. While oxo-G without thermal treatment possesses a relatively intact hexagonal carbon framework (**Figure S2**), monolayer oxo-G$^{300°C}$ shows an inhomogeneous structure as depicted in the chromatic (Cc) and spherical (Cs) aberration-corrected high-resolution TEM image presented in **Figure 3**. The hexagonal graphene

structures are isolated by holes and stacked double-layer patches, as marked. The size of the defect-free graphene islands varies from
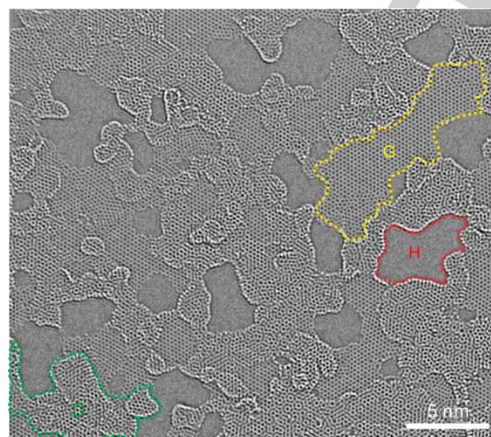

Figure 3. Cc/Cs-corrected high-resolution 80 kV TEM image of thermally-processed oxo-G at 300 °C (oxo-G$^{300°C}$), showing holes, areas of stacked carbon layers and grain-boundaries. The striking features are marked: holes (H), intact single-layer graphene (G) and double-layer carbon (D).

1 nm to 10 nm in diameter or length and these areas cover roughly 50% of the whole surface. The observed holes with diameter size of 3-5 nm comprise approximately 20% of the area. In addition, the nanometer-sized double-layer regions distributed around holes are eye-catching. Accordingly, sp^3 arrangements in the stacked double-layer regions are plausible in conjugation with sp^2-C.[27]
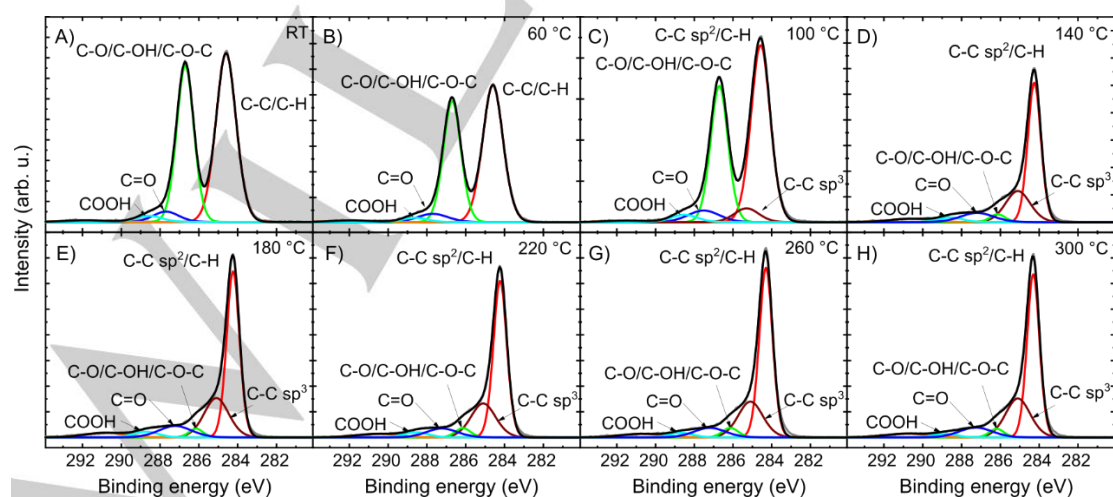

Figure 2. High-resolution C 1s XPS of oxo-G treated by iteratively annealing up to 300 °C
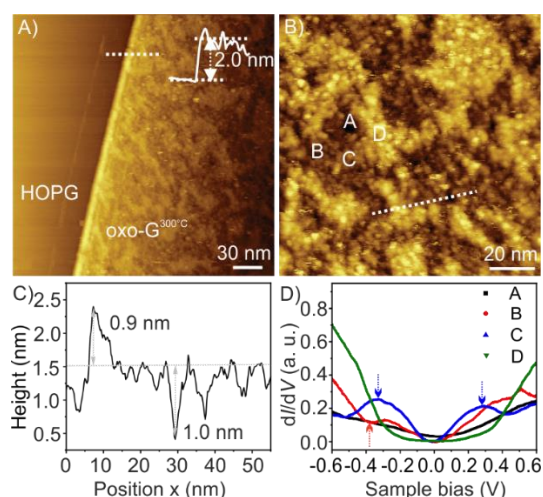
Figure 4. A) A large-scale STM topographic image of the oxo-G$^{300°C}$ on HOPG (200 nm × 200 nm; tunneling current I_t = 0.5 nA, sample voltage bias V_s = -0.6 V). The inset is the height profile of the monolayer oxo-G$^{300°C}$ flake on HOPG. B) A STM topographic image obtained after zooming in onto the surface of the oxo-G$^{300°C}$ flake shown in A (100 nm × 100 nm; I_t = 0.5 nA, V_s = -0.3 V). C) Height profiles along the dashed line marked in B. D) Local dI/dV curves measured at different positions, as marked in B.

To further prove the presence and impact of the sp^3-areas, we conducted scanning tunneling microscopy (STM) and spectroscopy (STS). With STS we surprisingly found local semiconductor properties. First, the morphology of the oxo-G$^{300°C}$ was examined by STM. **Figure 4A** shows a large-scale STM image of a single oxo-G$^{300°C}$ flake on highly oriented pyrolytic graphite (HOPG). The average height of the single layer is about 2.0 nm, which is almost twice the thickness of monolayer oxo-G, as we reported before.[28] This is ascribed to fluctuations of the carbon plane caused by the rearrangement and loss of monoatomic carbon in oxo-G after thermal annealing, as TEM showed. With zooming onto the oxo-G$^{300°C}$ surface, dome-shaped morphologies were detected (**Figure 4B**). There are three differently colored distributions as in **Figure 4B**, dark, brown and bright. Height profiles in **Figure 4C** show the height difference from the bright plane to brown plane and from the dark plane to brown plane of 0.9 and 1 nm, respectively. Topographical fluctuations over a 50 nm range is 1.9 nm, which nearly coincides with the thickness of this single layer. This indirectly indicates that the dark, brown and bright regions correspond to holes, graphene domains and stacked double-layer carbon, respectively.

The local electronic properties of these heterogeneous topographical surfaces in the oxo-G$^{300°C}$ were investigated *via* STS. The differential conductivity (dI/dV), which is proportional to the local density of states (LDOS) at small bias, was simultaneously obtained during the STM measurements using a grid *I-V* scan. The dI/dV curves in **Figure S4** were obtained by averaging 3600 dI/dV curves recorded on the HOPG and the oxo-G$^{300°C}$ surface at respective places, respectively, as labelled in exemplarily in **Figure 4B**. The dI/dV spectrum of HOPG shows a nearly symmetrical parabolic geometry. The oxo-G$^{300°C}$ exhibits a V-shaped dI/dV reminiscent of two-dimensional Dirac material. The Dirac point is located at + 40 mV. This p-type doping here is in agreement with the transport measurements in **Figure 2J** determined on micrometer-sized channels. The specific

electronic information at different positions (marked as A, B, C and D, shown in **Figure 4B**) was depicted by the local dI/dV spectra in **Figure 4D** (exemplary individual data shown in **Figure S8**). Obviously, the measured four positions present a distinct electrical inhomogeneity. First, the black line (measured at dark areas such as position A) shows a metallic-like behavior, similar to LDOS behavior of HOPG,[29] which confirms that the dark areas are holes. Then, the red line (measured at brown areas like position B) shows a conical-shaped curve, corresponding to single layer graphene structures.[30] It is worth noting that the shake at the red arrow represents defective states, indicating some defects exists in the single-layer graphene structure. Two prominent peaks marked by blue arrows are observed in the blue line (measured at bright areas like position C). Similar STS spectra were also found in twisted graphene bilayers.[31] The two saddle peaks are attributed to energy separations of the low-energy van Hove singularities (VHSs) in graphene bilayers. Therefore, it can be demonstrated that the bright regions contain some sp^2-hybrided double-layer graphene structures. It is in particular interesting that a suppressed dI/dV distribution (green line) is measured at the brighter areas (position D, compare **Figure S8**). The green averaged dI/dV curve (**Figure 4D**) represents a typical semiconducting behavior[15b, 32] with a bandgap of around 0.4 eV (**Figure 4D**). Combing the atomically-resolved carbon structures (**Figure 3** and **Figure 4B**) with the height of 1.9 nm (**Figure 4C**) at position D, we thereby deduce that such a large bandgap attributes to formed conjugated sp^2-C, which is isolated from the surrounding graphene lattice.
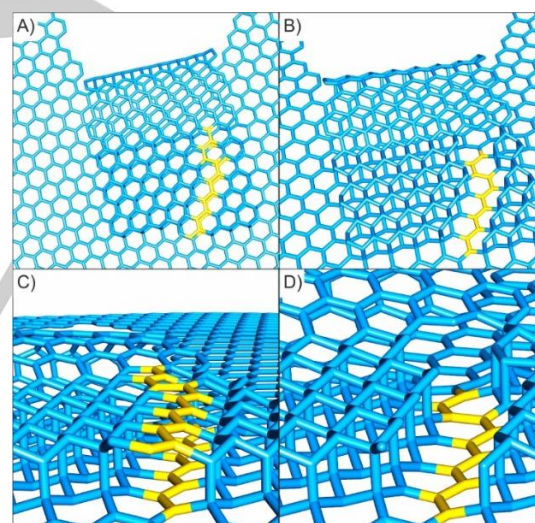

Figure 5. Schematic illustration of proposed chemical structures of thermally-processed oxo-G. A) and B) Top view of the mixed sp^2- and sp^3- C structures. C) and D) Side view of the mixed sp^2- and sp^3- C structures.

As detected by XPS, the sp^3-sp^3-C and C-O/C-OH/C-O-C of 3.4%. can act as insulator (illustrated in **Figure 5**). Their appearance might be related to the in-plane crack of carbon-carbon bonds during the formation of holes and the released carbon fragments react with the underlying graphene by sp^3-hybridization (**Figure 5**). Since the semiconducting areas have a 25% fraction (based on TEM area analysis) in the entire carbon layer, their effect on the overall

band structure of oxo-G$^{300°C}$ is almost insignificant. The formation of sp^2 carbon is further upon thermal disproportionation of oxo-G is supported by FTIR investigations in **Figure S5**, due to the IR active signal at about 1570 cm^{-1}, a signal that was also found in nano-diamonds with sp^2-patches.[33] Moreover C-H bond cleavage may play a role, as evidenced from FTIR (2920 cm^{-1} and 2850 cm^{-1}, **Figure S5**), however, elimination of water is more likely up to 140 °C.

In summary, it can be stated that sp^3-sp^3 diamond-like, imperfect sp^3-sp^2-sp^3 or C-O-C bridged out of plane structures open a new path to semiconducting graphene-based materials. Here, we describe the defect structures including holes and bilayer sp^3-patches induced by thermal disproportion of the oxo-G. The identified C-C sp^3-patches and bridging C-O-C motifs, which are connected to nm-sized patches of the hexagonal carbon lattice of graphene, are separated by grain boundaries and holes which are 5 nm in diameter. We suggest that C-C sp^3-bonds are formed either after folding or adsorption of carbon patches, indicating that reactive species, including C-O-structures, are formed in the course of the disproportionation reaction. The sp^3-patches isolate residual sp^2-C and thus local STS reveals the semiconducting behavior of these areas. It turns out that the nm-sized mixed sp^2- and sp^3- structures have a bandgap of ~ 0.4 eV. Our study indicates that semiconductor/graphene hybrid materials are interesting materials with local semiconducting properties. With these deeper insights of the thermal disproportionation of oxo-G and correlation to the electrical properties future applications and the development of carbon-based semiconductors becomes possible. In particular, the formation of holes and sp^3-stacked regions potentially play a significant role for chemical reactions used to post-functionalize materials. Moreover, bottom-up synthesized molecular carbon materials containing sp^3- and sp^2-carbon with a tunable band-gap might be discovered in the future.

Acknowledgements

References

[1]   a) Y. Zhu, S. Murali, W. Cai, X. Li, J. W. Suk, J. R. Potts, R. S. Ruoff, *Adv. Mater.* **2010**, *22*, 3906-3924; b) D. R. Dreyer, S.Park, C. W. Bielawski, R. S. Ruoff, *Chem. Soc. Rev.* **2010**, *39*, 228-240; c) W. S. Hummers, R. E. Offeman, *J. Am. Chem. Soc.* **1958**, *80*, 1339.

[2]   a) G. Eda, M. Chhowalla, *Adv. Mater.* **2010**, *22*, 2392-2415; b) D. W. Boukhvalov, M. I. Katsnelson, *J. Am. Chem. Soc.* **2008**, *130*, 10697-10701; c) D. R. Dreyer, A. D. Todd, C. W. Bielawski, *Chem. Soc. Rev.* **2014**, *43*, 5288-5301; d) K. Erickson, R. Erni, Z. Lee, N. Alem, W. Gannett, A. Zettl, *Adv. Mater.* **2010**, *22*, 4467-4472.

[3]   V. Georgakilas, M. Otyepka, A. B. Bourlinos, V. Chandra, N. Kim, K. C. Kemp, P. lHobza, R. Zboril, K. S. Kim, *Chem. Rev.* **2012**, *112*, 6156-6214.

[4]   a) T. Tsuchiya, K. Terabe, M. Aono, *Adv. Mater.* **2014**, *26*, 1087-1091; b) H. X. Chang, Z. H. Sun, Q. H. Yuan, F. Ding, X. M. Tao, F. Yan, Z. J. Zheng, *Adv. Mater.* **2010**, *22*, 4872.

[5]   a) Q. S. Mei, B. H. Liu, G. M. Han, R. Y. Liu, M. Y. Han, Z. P. Zhang, *Adv. Sci.* **2019**, *6*, 1900855; b) L. Cao, M. J. Meziani, S. Sahu, Y. P. Sun, *Acc. Chem. Res.* **2013**, *46*, 171-180.

[6]   D. Jariwala, V. K. Sangwan, L. J. Lauhon, T. J. Marks, M. C. Hersam, *Chem. Soc. Rev.* **2013**, *42*, 2824-2860

[7]   D. W. Boukhvalov, M. I. Katsnelson, *J. Am. Chem. Soc.* **2008**, *130*, 10697-10701.

[8]   a) D. C. Marcano, D. V. Kosynkin, J. M. Berlin, A. Sinitskii, Z. Z. Sun, A. Slesarev, L. B. Alemany, W. Lu, J. M. Tour, *ACS Nano* **2010**, *4*, 4806-4814; b) N. Morimoto, H. Suzuki, Y. Takeuchi, S. Kawaguchi, M. Kunisu, C. W. Bielawski, Y. Nishina, *Chem. Mater.* **2017**, *29*, 2150-2156.

[9]   P. Feicht, S. Eigler, *ChemNanoMat* **2018**, *4*, 244-252.

[10]   S. Eigler, C. Dotzer, A. Hirsch, *Carbon* **2012**, *50*, 3666-3673.

[11]   S. Eigler, C. Dotzer, A. Hirsch, M. Enzelberger, P. Müller, *Chem. Mater.* **2012**, *24*, 1276-1282.

[12]   A. Dimiev, D. V. Kosynkin, L. B. Alemany, P. Chaguine, J. M. Tour, *J. Am. Chem. Soc.* **2012**, *134*, 2815-2822.

[13]   S. Eigler, M. Enzelberger-Heim, S. Grimm, P. Hofmann, W. Kroener, A. Geworski, C. Dotzer, M. Rockert, J. Xiao, C. Papp, O. Lytken, H. P. Steinrück, P. Müller, A. Hirsch, *Adv. Mater.* **2013**, *25*, 3583-3587.

[14]   S. Eigler, *Chem. Eur. J.* **2016**, *22*, 7012-7027.

[15]   a) S. H. Dave, C. C. Gong, A. W. Robertson, J. H. Warner, J. C. Grossman, *ACS Nano* **2016**, *10*, 7515-7522; b) *Nat Nanotechnol*; c) F. Banhart, J. Kotakoski, A. V. Krasheninnikov, *ACS Nano* **2011**, *5*, 26-41.

[16]   F. Grote, C. Gruber, F. Börrnert, U. Kaiser, S. Eigler, *Angew. Chem. Int. Ed.* **2017**, *56*, 9222-9225.

[17]   C. E. Halbig, R. Lasch, J. Krull, A. S. Pirzer, Z. P. Wang, J. N. Kirchhof, K. I. Bolotin, M. R. Heinrich, S. Eigler, *Angew. Chem. Int. Ed.* **2019**, *58*, 3599-3603.

[18]   a) L. Dong, J. Yang, M. Chhowalla, K. P. Loh, *Chem. Soc. Rev.* **2017**, *46*, 7306-7316; b) M. Hada, K. Miyata S. Ohmura, Y. Arashida, K. Ichiyanagi, I. Katayama, T. Suzuki, W. Chen, S. Mizote, T. Sawa, T. Yokoya, T. Seki, J. Matsuo, T. Tokunaga, C. Itoh, K. Tsuruta, R. Fukaya, S. Nozawa, S. Adachi, J. Takeda, K. Onda S. Koshihara, Y. Hayashi, Y. Nishina, *ACS Nano* **2019** *13*, 10103-10112; c) R. K. Joshi, S. Alwarappan, M. Yoshimura, V. Sahajwalla, Y. Nishina, *Appl. Mater. Today* **2015**, *1*, 1-12.

[19]   C. K. Chua, M. Pumera, *Chem. Soc. Rev.* **2014**, *43*, 291-312.

[20]   a) V. Georgakilas, J. N. Tiwari, K. C. Kemp, J. A. Perman, A. B. Bourlinos, K. S. Kim, R. Zboril, *Chem. Rev.* **2016**, *116*, 5464-5519; b) N. Morimoto, T. Kubo, Y. Nishina, *Sci. Rep.* **2016**, *6*, 21715.

[21]   a) S. Eigler, C. Dotzer, F. Hof, W. Bauer, A. Hirsch, *Chem. Eur. J.* **2013**, *19*, 9490-9496; b) P. Feicht, J. Biskupek, T. E. Gorelik, J. Renner, C. E. Halbig, M. Maranska, F. Puchtler, U. Kaiser, S. Eigler, *Chem. Eur. J.* **2019**, *25*, 8955-8959.

[22]   Q. B. Zheng, W. H. Ip, X. Y. Lin, N. Yousefi, K. K. Yeung, Z. G. Li, J. K. Kim, *ACS Nano* **2011**, *5*, 6039-6051.

[23]   a) M. H. Yusuf, B. Nielsen, M. Dawber, X. Du, *Nano Lett.* **2014**, *14*, 5437-5444; b) Z. P. Wang Q. R. Yao, Y. L. Hu, C. Li, M. Hussmann, B. Weintrub, J. N. Kirchhof, K. Bolotin, T. Taniguchi, K. Watanabe, S. Eigler, *RSC Adv.* **2019**, *9*, 38011-38016.

[24]   H. Pieper, C. E. Halbig, L. Kovbasyuk, M. R. Filipovic, S. Eigler, A. Mokhir, *Chem. Eur. J.* **2016**, *22*, 15389-15395.

[25]   S. Eigler, S. Grimm, A. Hirsch, *Chem. Eur. J.* **2014**, *20*, 984-989.

[26] S. Seiler, C. E. Halbig, F. Grote, P. Rietsch, F. Börrnert, U. Kaiser, B. Meyer, S. Eigler, *Nat. Commun.* **2018**, *9*, 836.

[27] F. Börrnert, S. M. Avdoshenko, A. Bachmatiuk, I. Ibrahim, B. Buchner, G. Cuniberti, M. H. Rummeli, *Adv. Mater.* **2012**, *24*, 5630-5635.

[28] S. Eigler, F. Hof, M. Enzelberger-Heim, S. Grimm, P. Müller, A. Hirsch, *J. Phys. Chem. C* **2014**, *118*, 7698-7704.

[29] a) T. Matsui, H. Kambara, Y. Niimi, K. Tagami, M. Tsukada, H. Fukuyama, *Phys. Rev. Lett.* **2005**, *94*, 226403; b) Y. Niimi, T. Matsui, H. Kambara, K. Tagami, M. Tsukada, H. Fukuyama, *Phys. Rev. B* **2006**, *73*, 085421.

[30] J. M. Xue, J. Sanchez-Yamagishi, D. Bulmash, P. Jacquod, A. Deshpande, K. Watanabe, T. Taniguchi, P. Jarillo-Herrero, B. J. Leroy, *Nat. Mater.* **2011**, *10*, 282-285.

[31] L. J. Yin, J. B. Qiao, W. X. Wang, W. J. Zuo, W. Yan, R. Xu, R. F. Dou, J. C. Nie, L. He, *Phys. Rev. B* **2015**, *92*, 201408.

[32] K. S. Vasu, D. Pramanik, S. Kundu, S. Sridevi, N. Jayaraman, M. Jain, P. K. Maiti, A. K. Sood, *J. Mater. Chem. C* **2018**, *6*, 6483-6488.

[33] a) Y. J. Liang, M. Ozawa, A. Krueger, *ACS Nano* **2009**, *3*, 2288-2296; b) T. Petit, L. Puskar *Diam. Relat. Mater.* **2018**, *89*, 52-66.

45

Support information

Identification of Semiconductive Patches in Thermally Processed Monolayer Oxo-Functionalized Graphene

Zhenping Wang, [a] Qirong Yao, [b] Christof Neumann, [c] Felix Börrnert, [d] Julian Renner, [d] Ute Kaiser, [d] Andrey Turchanin, [c] Harold J. W. Zandvliet[b] and Siegfried Eigler*[a]

Abstract: The thermal decomposition of graphene oxide (GO) is a complex process at the atomic level and not fully understood. Here, a subclass of GO, oxo-functionalized graphene (oxo-G) was used to study its thermal disproportionation. We present the impact of annealing on the electronic properties of a monolayer oxo-G flake and correlated chemical composition and topography corrugation by two-probe transport measurements, XPS, TEM, FTIR and STM. Surprisingly, we found that the oxo-G, processed at 300 °C, bears C-C sp^3-patches, next to graphene domains and holes. It is striking that those C-C sp^3-patches with few nanometers in diameter possess semiconducting properties with a bandgap of about 0.4 eV. We propose that C-C sp^3-patches confine conjugated sp^2-C what leads to the local semiconductor properties. Accordingly, graphene with sp^3-C in double layer areas is a potential class of semiconductors and a potential target for future chemical modifications.

[a]   M. Sc. Z. Wang, Prof. Dr. S. Eigler
        Freie Universität Berlin, Institute for Chemistry and Biochemistry, Takustraße 3, 14195 Berlin, Germany
        E-mail: Siegfried.eigler@fu-berlin.de
[b]   Dr. Q. Yao, Prof. Dr. Ir. H. J. W. Zandvliet
        Physics of Interfaces and Nanomaterials, University of Twente,
        Enschede, 7500 AE, The Netherlands
[c]   M. Sc. C. Neumann, Prof. Dr. A. Turchanin
        Friedrich Schiller University Jena, Institute of Physical Chemistry,
        Lessingstraße 10, 07743 Jena, Germany
[d]   Dr. F. Börrnert, § M. Sc. J. Renner, Prof. Dr. U. Kaiser
        Universität Ulm, Zentrale Einrichtung Elektronenmikroskopie, Albert-
        Einstein-Allee 11, 89081 Ulm, Germany
        §Current address: Max-Planck-Institut für Mikrostrukturphysik,
        Weinberg 2, 06120 Halle, Germany

Table of Contents 47

Experimental Procedures

Materials:

Double-distilled water was obtained from Carl Roth GmbH. Graphite (3061) was purchased from Asbury Carbon. Chemicals, solvents and other materials were obtained from Sigma-Aldrich. Si wafers with a 300 nm thick SiO_2 layer were purchased from Fraunhofer-Institut für Integrierte Systeme und Bauelementetechnologie IISB in Erlangen.

Synthesis of oxo-G:

Oxo-G was synthesized by low-temperature oxidation of graphite based on our previously reported method. Briefly, 1g of graphite (type 3061, Asbury Carbon) was mixed with 25 mL of sulfuric acid (97.5%) at a temperature low than 10 °C. Then, 2 g of $KMnO_4$ was slowly added over 4 h and further stirred for 16 h. After that, 20 mL of cold diluted sulfuric acid (20 wt%) and 50 mL of cold double distilled water were orderly added into the mixture using programmed pump with 4 h and 16 h. Subsequently, 20 mL of H_2O_2 (5 wt%) was added to remove excess manganese species. Finally, the oxo-G dispersion solution was obtained after purification treatment by centrifugation and mild sonication.

Preparation of LB-assembled oxo-G film:

The oxo-G spreading solution (2 mL) with a 1:2 mixture of water/ methanol was added on a water subphase trough (Kibron, µtrough). Flakes of oxo-G were deposited onto Si/SiO2 (300 nm) substrate (for preparation of XPS samples and FET devices), HOPG bulk (for preparation of STM samples) and Quantifoil grid (for preparation of TEM samples) at 3 mN/m by Langmuir–Blodgett (LB) technique.[21] The LB-assembled oxo-G samples were used for further characterization and preparation of FET devices.

Fabrication of monolayer oxo-G FET transistor:

Standard electron beam lithography (EBL) procedure (Raith PIONEER TWO) was used to define and expose the geometry of metal contacts. Subsequently, a 5 nm/ 70 nm Cr/Au stack was deposited with thermal evaporation (Kurt J. Lesker NANO 36) and lifted off in acetone to make electrode contact to oxo-G flake. Thermally annealing of the oxo-G FET device was performed using a heating oven with a vacuum degree of 10^{-3} mbar.

Preparation of GO Films on ZnSe

A diluted oxo-G solution was drop-casted on a ZnSe substrate. And then the oxo-G film was formed by evaporation of the distilled water at ambient conditions.

Characterization:

Optical microscope (Nikon Eclipse, LV150) was used to visualize oxo-G FET devices. Cc/Cs-corrected high-resolution 80 kV Transmission electron microscopy (TEM) images were obtained using the SALVE microscope operated at 80 kV electron acceleration voltage. Statistical Raman spectroscopy (SRS) was recorded using a Horiba Explorer spectrometer with a 532 nm laser for excitation. Scanning tunneling microscopy (STM) and Scanning tunneling spectroscopy (STS) were achieved by Omicron-STM1 with an ultra-high vacuum of $<10^{-10}$ mbar. X-ray photoelectron spectroscopy (XPS) was performed by a multiprobe system (Scienta Omicron) with a monochromatic X-ray source (Al K_α) and an electron analyzer (Argus CU) with 0.6 eV spectral energy resolution. The spectra were fitted using Voigt functions (30: 70) after Shirley background subtraction. The FTIR measurements were performed by FT-IR Vertex 70 (Bruker) in transmission mode using ZnSe windows as support. All transport measurements were performed at ambient conditions by a two-probe station and two source-measurement units (Keithley 2450).
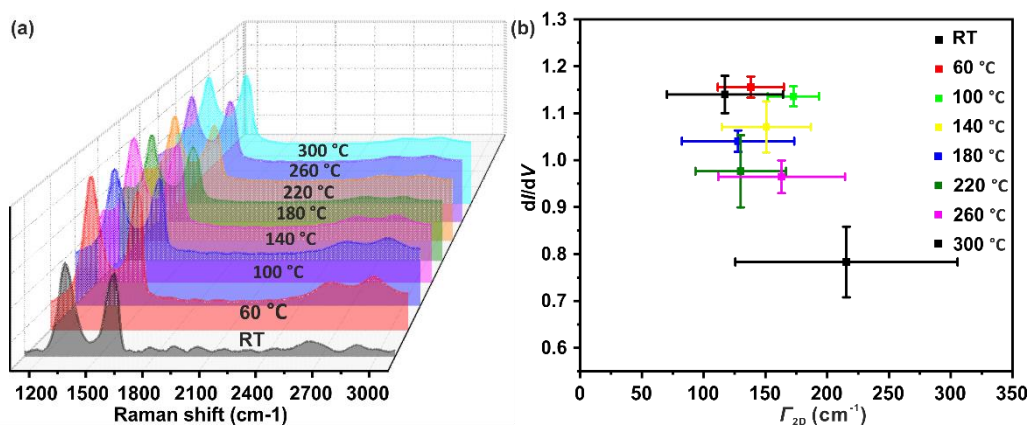
Figure S1. Statistical Raman analysis performed by scanning an area of with ∼ 20 ×20 µm² at 532 nm laser excitation wavelength. (a). Average Raman spectra of monolayer oxo-G and thermally processed monolayer oxo-G at different temperature. (b) plot of I_D/I_G versus Γ_{2D}.
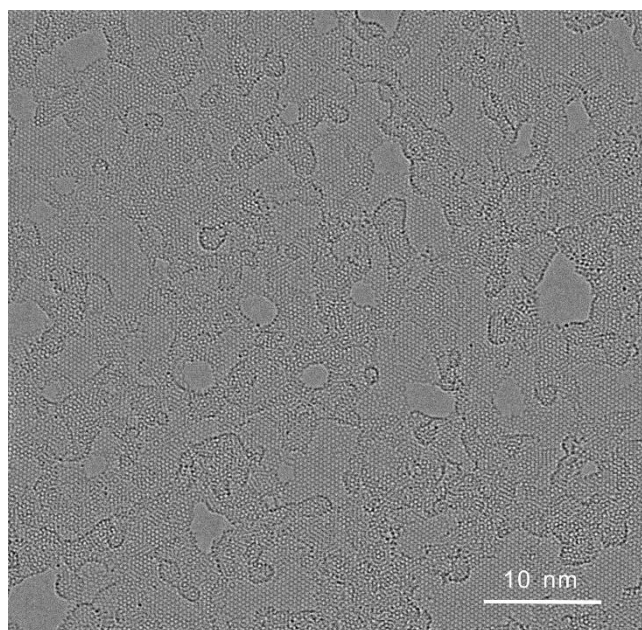

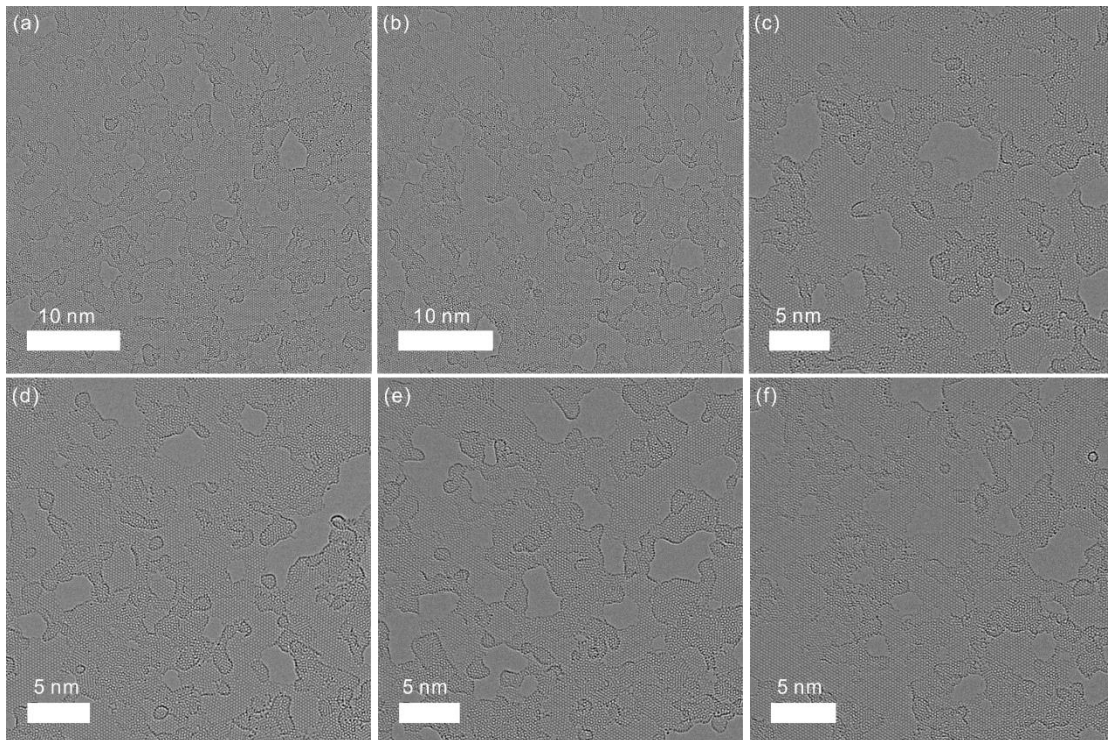**Figure S2**. Cc/Cs-corrected high-resolution 80 kV Transmission electron microscopy (TEM) images of untreated oxo-G.

Figure S3. Cc/Cs-corrected high-resolution 80 kV Transmission electron microscopy (TEM) images of oxo-G treated at 300 °C for 15 mins. The oxo-G sample was heated using the TEM heating holder in the vacuum of our plasma cleaner at 300 °C for 15 minutes and analyzed directly afterwards in the SALVE microscope at 80 kV electron acceleration voltage.
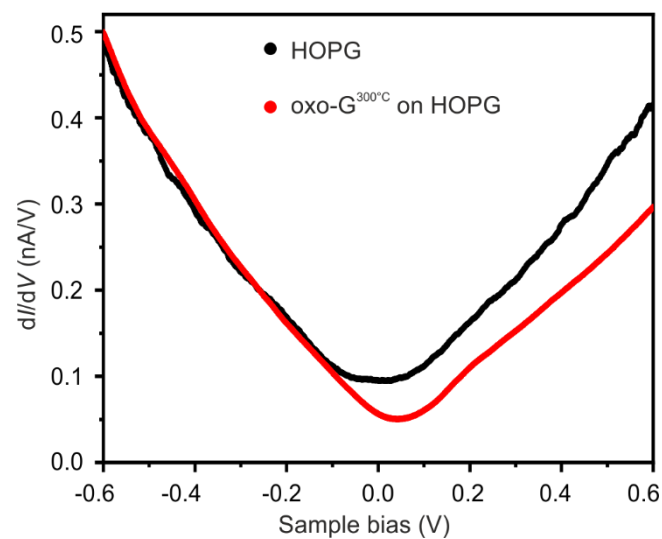
Figure S4. Averaged dI/dV spectra on HOPG and oxo-G$^{300°C}$ surface. The dI/dV spectra were recorded by using a lock-in amplifier with a sinusoidal modulation (f =1.89 KHz, V_{mode} = 18 meV) of the feedback-loop gain off.
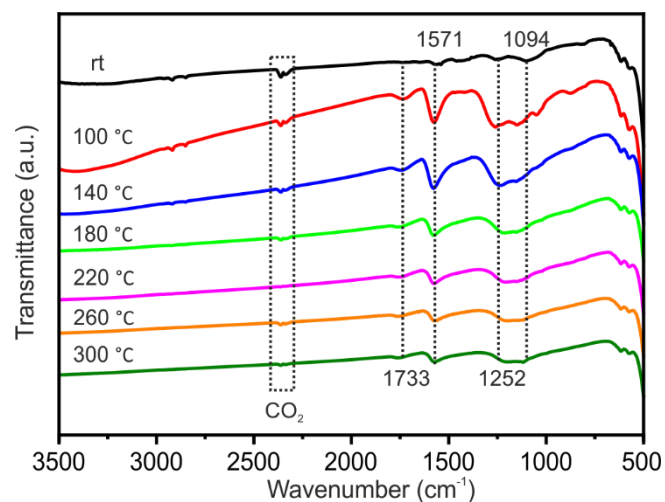
Figure S5. FTIR spectra of thermally processed oxo-G films on a ZnSe substrate.
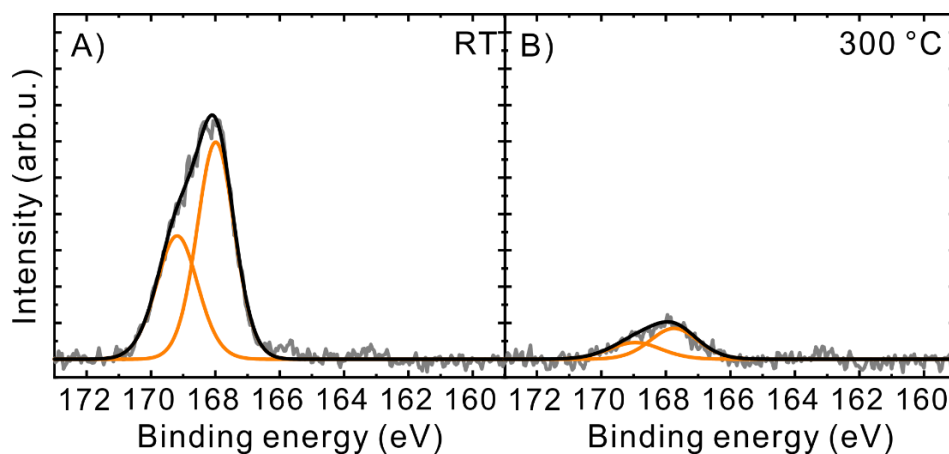
Figure S6. High-resolution S 2p XPS of oxo-G and oxo-G^T annealed with 300 °C. Both spectra show a signal assigned to oxidized sulfur whereas no trace of C-S bonds (162-164 eV) are detected. The total amount of sulfur is decreasing with higher annealing temperatures (Table S1).
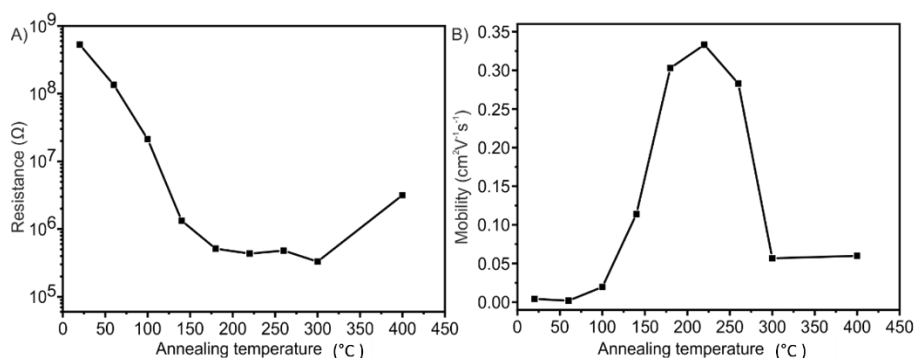
Figure S7. Changes of resistance and mobility as a function of annealed temperature.

Table S1. C/O and C/S ratios obtained by X-ray photoelectron spectroscopy using a relative sensitivity factor (RSF) of 1 (C 1s), 2.93 (O 1s) and 1.68 (S 2p). Note that the absolute C/O ratio is affected by the oxygen in the underlying SiO$_2$/Si substrate.

sample	C / O ratio (±0.1)	C / S ratio (±1)
RT	2.2 : 1	24 : 1
60 °C	2.4 : 1	28 : 1
100 °C	2.4 : 1	28 : 1
140 °C	4.6 : 1	32 : 1
180 °C	4.7 : 1	33 : 1
220 °C	4.6 : 1	33 : 1
260 °C	5.0 : 1	79 : 1
300 °C	7.5 : 1	191 : 1

Table S2. Quantitative analysis of the high resolution XP C 1s spectra presented in **Figure 1** of the main paper including the peak assignment, their binding energies, full width at half maximum (FWHM) values and areas obtained from the spectra deconvolution.

Peak assignment	Binding energy, eV	FWHM, eV	Area, %
RT			
C-C/C-H	284.6	1.2	51.8
C-O/C-OH/C-O-C	286.7	1.0	40.6
C=O	287.7	1.6	4.0
COOH	288.6	1.6	2.5
aromatic shake-up	291.8	2.5	1.1

60 °C			
C-C/C-H	284.6	1.2	52.3
C-O/C-OH/C-O-C	286.7	1.1	39.5
C=O	287.7	1.8	4.7
COOH	288.6	1.5	2.1
aromatic shake-up	291.9	2.5	1.4
100 °C			
C-C sp^2/C-H	284.6	1.2	50.7
C-C sp^3	285.3	1.5	5.1
C-O/C-OH/C-O-C	286.7	1.0	34.9
C=O	287.5	1.9	5.4
COOH	288.5	1.6	2.9
aromatic shake-up	291.5	2.5	1.0
140 °C			
C-C sp^2/C-H	284.3	0.8	55.6
C-C sp^3	285.1	1.5	23.5
C-O/C-OH/C-O-C	286.1	0.9	3.7
C=O	287.2	2.0	9.3
COOH	288.6	1.5	3.5
aromatic shake-up	290.6	2.5	4.4
180 °C			
C-C sp^2/C-H	284.2	0.8	54.2
C-C sp^3	285.1	1.5	24.7
C-O/C-OH/C-O-C	286.2	0.8	3.1
C=O	287.2	2.0	9.6
COOH	288.7	1.5	3.6
aromatic shake-up	290.8	2.5	4.9
220 °C			
C-C sp^2/C-H	284.2	0.8	57.5
C-C sp^3	285.1	1.5	23.2
C-O/C-OH/C-O-C	286.2	0.9	3.9
C=O	287.2	1.9	7.7
COOH	288.5	1.5	3.5
aromatic shake-up	290.5	2.5	4.3
260 °C			
C-C sp^2/C-H	284.3	0.8	58.2
C-C sp^3	285.1	1.5	23.1
C-O/C-OH/C-O-C	286.1	1.0	4.0
C=O	287.2	1.9	7.9
COOH	288.7	1.5	2.9
aromatic shake-up	290.7	2.5	4.0

300 °C			
C-C sp^2/C-H	284.3	0.8	54.9
C-C sp^3	285.1	1.5	26.1
C-O/C-OH/C-O-C	286.2	0.9	3.4
C=O	287.3	2.0	8.9
COOH	288.9	1.5	2.4
aromatic shake-up	290.8	2.5	4.4

4. Minor contributions

4.1 Functionalization of oxo-G-based materials

4.1.1. Selective functionalization of oxo-G at defect-activated sites

Title:	Selective Functionalization of Graphene at Defect-Activated Sites by Arylazocarboxylic tert-Butyl Esters
Authors	Christian E. Halbig, Roman Lasch, Jasmin Krüll, Anna Pirzer, Zhenping Wang, Markus R. Heinrich and Siegfried Eigler
To be cited as	*Angew. Chem. Int. Ed*. **2019**, *58*, 3599–3603 https://doi.org/10.1002/anie.201811192
Detailed scientific contribution	In this paper, partly Raman characterizations were done by me. The AFM image of oxo-G flakes was provided by me.
Estimated own contribution	~ 8%

Supporting Information

Selective Functionalization of Graphene at Defect-Activated Sites by Arylazocarboxylic tert-Butyl Esters

Christian E. Halbig, Roman Lasch, Jasmin Krgll, Anna S. Pirzer, Zhenping Wang, Jan N. Kirchhof, Kirill I. Bolotin, Markus R. Heinrich, and Siegfried Eigler

Experimental Section

Materials and Methods

Double-distilled water from Carl Roth GmbH. All other chemicals were purchase from sigma Aldrich and used as obtained. For SRS, we used a Horiba LabRAM Aramis spectrometer and equipped with a 532 nm laser for excitation combined with 100x magnification lenses. dT- SRS was measured under nitrogen flow using a Horiba LabRAM Aramis combined with a heating chamber. Maps with a sufficient number of spectra suitable for a convincing statistical analysis had been recorded. Elemental analysis (EA) was measured with Vario EL from Elementar Analysensysteme GmbH. TGA-MS was performed on a Netzsch STA 409 CD-QMS 403/5 SKIMMER. AFM images were recorded on an NT-MDT Solver Pro equipped with NSG10/Au probes and intermittent contact mode was chosen. For purification of oxo-G we used a Sigma 4K-15 (rotor: 6x200 mL PP beakers).

Synthesis of oxo-^{S}G and ^{S}G

Oxo-functionalized Graphene with a degree of functionalization of about 66% was prepared by stirring 1g of graphite in sulphuric acid (25 mL; 97%) and the addition of 2g KMnO4 over 4 hours as reported in other literature.[1] Then, 20 mL of cold diluted sulphuric acid (over 4 hour) and 100 mL col water (over 16 hour) was added over 4 hour. Finally, the reaction was stopped by the dropwise addition of cold 3% H2O2 (over 40 min) and the oxidized crystals were centrifuged for six times until the pH was neutral. After delamination with the help of pulsed tip sonication (20 W; 4 min; 2s on, 2s off), non-monolayer particles were removed by repetitive centrifugation at low RCF and smallest particles by centrifugation at high RPM. The concentration was determined by lyophilisation. The dispersion was stored at 4°C. The concentration of the dispersion was 0.75 mg/mL determined by freeze drying. EA: C: 48.4% H: 3.8% N: 0.0% S: 4.6% O*: 43.2%. G was obtained after reduction of oxo-G by hot hydrogen iodine and trifluoro acetic acid (more details below).

Synthesis of oxo-*G and *G

Oxo-functionalized Graphene with an almost intact carbon lattice and a degree of functionalization of about 4% was prepared as following: 20 g graphite was stirred in sulphuric acid (500 mL; 97%) and 3 mass equivalent (NH4)2S2O8 were added over a period of three days in small portions. After few hours, the graphite changed his color from grey to deep-blue. The reactive mixture was stored for several 4 weeks at ambient conditions. An arbitrary amount of the so formed GIC (approx. 1 g) was taken from the bottle and centrifuged to remove excess of sulfuric acid. Then, the precipitated GIC was frozen at - 24 °C, overlaid with cold water (50 mL, 4 °C) and stored in fridge overnight. The deep-blue color disappeared due to the formation of graphite oxide. The dispersion was centrifuged with water using 50 mL falcon tubes at 14.000 RCF until the pH was neutral. Thus, purified graphite oxide was then transferred into a mixture of 50:50 water/methanol and exfoliated by ultrasound for 10 minutes in an ultrasonication bath and finally stored for 16 hours at room temperature. Large particles were removed from the supernatant with following parameters: 4 times, 700 RCF, 5 minutes; 8 times, 1500 RCF, 5 minutes; 4 times 1500 RCF, 7.5 minutes. Smallest fragments were removed from the dispersion by applying 9.000 RCF for 40 minutes for three times, whereas the supernatant was removed. A dark greenish to grey dispersion was obtained containing single layer oxo-G with diameter of about 5 µm next to few-layer oxo-G. *G was obtained after reduction of oxo-*G by hot hydrogen iodine and trifluoro acetic acid (more details below).

Synthesis of ^{S}G/Surfactant

Solid surfactant (sodium dodecylsulfat, sodium dodecylbenzenesulfonat, or sodiumcholate) was added to the obtained and diluted oxo-G$^{50\%}$ dispersion (c = 0.75 mg/mL). The final concentration of the surfactant in the oxo-G dispersion was 4 mg/mL. Then, an excess of 10 mg of sodium borohydride per milligram oxo-G was added to the cold oxo-G dispersion and further stored in refrigerator overnight (4 °C). We obtained a deep black, strongly basic and stable dispersion. At least, the mixture was washed with the corresponding aqueous surfactant (2 mg/mL) by repetitive centrifugation for three times and finally redispersed with pure water.

Deposition and reduction of oxo-G derivatives on SiO2/Si wafer

Oxo-G^0 or its derivatives were deposited a 300 nm SiO2/Si wafer by Langmuir- Blodgett technique. First our oxo-G dispersion was diluted with water (~1:10) and then furthermore diluted with 1:1 with of pure methanol. The mixture was dropped on the water-interface in a Langmuir-Blodgett trough and the barriers were compressed until a surface tension of 3 mN/m was reached. After deposition, wafers were placed in 20 mL glass vials filled with glass wool and were reduced by the vapor of HI and TFA for 20 min at 80 °C. Subsequently they were extensively washed with pure water.

Thermal defect introduction into oxo-*G

Oxo-*G was deposited on 300 nm SiO2/Si wafer (5x5 mm) by drop casting (2.5 µL). After the solvent was evaporated, the wafer was placed in a 50 mL glass vial and filled with argon and annealed for 90 minutes at 200 °C on a heating plate.

Surface assisted functionalization

To achieve functionalization of the graphene derivatives, we prepared solutions of 4-bromophenyldiazonium tetrafluoroborate and all arylazocarboxylate derivatives in 50:50 H$_2$O/MeCN with a concentration of 2 mM. Subsequently, the wafer coated with one of the graphene derivatives was placed in a 5 mL glas vial and 3 mL of the corresponding solution was added in a way, that the complete wafer was covered by the arylation agent. The mixture was activated by the addition of 300 µl trifluoroacetic acid (1 mol/L) and the wafers were incubated for 21°C, 60°C and 80°C for specific reaction times and thereafter carefully rinsed with H2O/MeCN, THF, H2O/MeCN and finally pure water. The same procedure was applied for *G.

Bulk functionalization of ^{S}G/Surfactant

20 mL of aqueous ^{S}G/SCH dispersion was mixed with solid 4 bromobenzenediazonium tetrafluoroborate (100 mg) and stirred overnight. Additionally, 20 mL of the same aqueous ^{S}G/SCH dispersion was mixed with 0.4 mM Arylazocarboxylate dissolved in 8 mL acetonitrile. After 1.5 mL of 1 M trifluoroacetic acid was added, the mixture was heated up to 60 °C for 3 hours while it was vigorously stirred and bubbled with oxygen. All dispersions were centrifuged repeatedly for purification and then freeze-dried overnight. The purification was performed in the following manner: 50:50 H2O/MeCN (2x), acetonitrile (2x), 50:50 H2O/MeCN (2x) and finally one time with pure water. Between every step, the samples were placed in an ultrasound bath for 10 minutes.

Bromophenyl Tetrafluoroborates

These compounds were prepared as described in literature.[2] 4-Bromoaniline (0.25 mol) was dissolved in 110 mL of tetrafluoroboric acid solution under stirring and being cooled in an ice bath an. A cold solution of sodium nitrite (17g, 0.25 mol) in 34 mL water is added dropwise and stirred for 30 minutes. Then, the precipitation was filtered off and washed once with cold fluoroboric acid (≈ 30 mL), for two times with 95% ethanol and for further two times with ether. Yield: 73%.

tert-Butyl 2-(4-cyanophenyl)azocarboxylate: (4-cyano)-hydrazine (11.8 mmol, 2.0 g) is dissolved in dry acetonitrile (20 mL) and treated with di-*tert*- butyl dicarbonate (13.0 mmol, 2.84 g) under argon atmosphere. After complete consumption of the reactants, as monitored by TLC, the solvent is removed under reduced pressure. The residue is subjected to column chromatography (silica gel, 1:0→100:1→50:1→25:1 dichloromethane/methanol) to give *tert*-butyl 2-(4-cyanophenyl)hydrazine-1-carboxylate (10.6 mmol, 2.46 g, 89%) as a yellow solid. R_f = 0.3 in 100:1 dichloromethane/methanol. ^{1}H NMR (400 MHz, CDCl$_3$, 25°C, TMS): δ=7.5 – 7.5 (m, 2H), 6.9 – 6.8 (m, 2H), 6.4 (s, 1H), 1.5 ppm (s,9H).

To a stirred solution of 2-(4-cyanophenyl)hydrazine-1-azocarboxylate (9.26 mmol, 2.16 g) in dry dichloromethane (20 mL), manganese dioxide (46.5 mmol, 4.04 g) is subsequently added under nitrogen atmosphere. After complete consumption of the reactants, as monitored by TLC, the mixture is filtered over Celite. Removal of the solvent under reduced pressure and column chromatography (silica gel, 20:1→10:1→8:1→5:1 hexane/ethyl acetate) give *tert*-butyl 2-(4-cyanophenylazocarboxylate (6.88 mmol, 1.59 g, 74%) as a yellow solid. R_f=0.4 (10:1 hexane/ethylacetate). ^{1}H NMR (400 MHz, CDCl$_3$, 25°C, TMS): δ=8.0- 7.9 (m, 2H), 7.8 -7.8 (m, 2H), 1.7 ppm (s, 9H).^{13}C NMR (101 MHz, CDCl$_3$, 25°C, TMS): δ=160.7 (C$_q$), 153.4 (C$_q$), 133.5 (2 × CH), 124.0 (2 × CH), 118.0 (C$_q$), 116.4 (C$_q$), 86.1 (C$_q$), 28.0 (3 × CH$_3$).; HR-MS (ESI) calculated for C$_{12}$H$_{13}$N$_3$O$_2$ [M$^+$ + Na$^+$]: 251.0900 u, found: 251.0896 u.

tert-Butyl 2-(4-bromophenyl)azocarboxylate: A solution of 4-bromoaniline (28.0 mmol, 4.82 g) in glacial acetic acid (15 mL) is treated with concentrated hydrochloric acid (60 mL) and cooled to 0 °C. A solution of sodium nitrite (28.0 mmol, 1.93 g) in water (6.5 mL) is added over a period of 20 minutes and the reaction is stirred for one hour at 0° C. A solution of tin chloride dihydrate (62.0 mmol, 14.0 g) in concentrated hydrochloric acid (15 mL) is added dropwise over a period of 45 minutes. After stirring for one hour at 0 °C, the precipitate is collected by filtration and dissolved in a saturated aqueous solution of potassium carbonate (200 mL). The composite is extracted with diethyl ether (4 × 50 mL). The combined organic phases are washed with a saturated aqueous solution of sodium chloride and dried over sodium sulfate. The crude product is used without further purification. The crude product is dissolved in dry acetonitrile (30 mL) and treated with di-*tert*-butyl dicarbonate (27.1 mmol, 5.92 g) under argon atmosphere. After complete consumption of the reactants, as monitored by TLC, the solvent is removed under reduced pressure. The residue is subjected to column chromatography (silica gel, hexane/ethyl acetate = 6:1) to give *tert*-butyl 2-(4-bromophenyl) hydrazine carboxylate (16.4 mmol, 4.70 g, 59%) as a white solid. R_f=0.3 in 6:1 hexane/ethyl acetate. ^{1}H NMR (600 MHz, CDCl$_3$, 25°C, TMS): δ=7.3 (d, J=8.8 Hz, 2 H), 6.7 (d, J=8.8 Hz, 2 H), 6.4 (bs, 1 H), 1.46 ppm (s, 9 H).

To a stirred solution of *tert*-butyl 2-(4-bromophenyl) hydrazine carboxylate (16.5 mmol, 4.70 g) in dry dichloromethane (30 mL), manganese dioxide (82.5 mmol, 7.17 g) is subsequently added under nitrogen atmosphere. After complete consumption of the reactants, as monitored by TLC, the mixture is filtered over Celite. Removal of the solvent under reduced pressure and column chromatography (silica gel, 20:1 hexane/ethyl acetate) give *tert*-butyl 2-(4-bromophenyl) azocarboxylate (14.7 mmol, 4.18 g, 89%) as an orange solid. R_f=0.7 (15:1 hexane/ethyl acetate). ^{1}H NMR (600 MHz, CDCl$_3$, 25°C, TMS): δ=7.77 (d, J=8.9 Hz, 2 H), 7.65 (d, J=8.9 Hz, 2 H),1.65 (s, 9 H). ^{13}C NMR (91 MHz, CDCl$_3$, 25°C, TMS): δ=160.9 (Cq), 150.3 (Cq), 132.6 (2 × CH), 128.2 (Cq), 124.9 (2 × CH), 85.3 (Cq), 27.8 ppm (3 × CH3). HR-MS (ESI) calculated for C$_{11}$H$_{13}$BrN$_2$O$_2$ [M$^+$ + Na$^+$]: 307.0053 u, found: 307.0058 u.

tert-Butyl 2-(4-(heptyloxy)phenyl)azocarboxylate: A solution of 4-nitrophenol (28.8 mmol, 4.0 g) and anhydrous potassium carbonate (57.5 mmol,7.95 g) in dry acetonitrile (60 mL) is treated with 1-iodoheptane (57.5 mmol, 9.43 mL) under argon atmosphere. The reaction mixture is stirred for 24 h under reflux. After the reaction is completed, the hot reaction mixture is filtered and the solvent is removed under reduced pressure. The crude product, 1-(heptyloxy)-4-nitrobenzene, is washed with dichloromethane (40 mL) and filtrated.1-(heptyloxy)-4-nitrobenzene (21.1 mmol, 5.02 g, 73%) is received as a yellow oil. R_f= 0.3 in 20:1 hexane/ethyl acetate. ^{1}H NMR (400 MHz, CDCl$_3$, 25°C, TMS): δ=8.2 – 8.2 (m, 2H), 7.0 – 6.9 (m, 2H), 4.1 (t, J(H,H)=7 Hz, 2H), 1.9 – 1.8 (m, 2H), 1.5 – 1.4 (m, 2H), 1.4 – 1.3 (m, 6H), 0.9 ppm (t, J(H,H)=7 Hz,3H).

1-(heptyloxy)-4-nitrobenzene (21.2 mmol, 5.02 g) and tin(II) chloride dihydrate (84.6 mmol, 19.1 g) are dissolved in concentrated hydrochloric acid (14.9 mL) and absolute ethanol (30 mL). The reaction mixture is stirred at room temperature. After complete consumption of the reactants, as monitored by TLC, the solvent is removed under reduced pressure. The crude product is diluted with water and treated with saturated sodium carbonate until a pH value of 9.5 is reached. The crude product is extracted with ethyl acetate (3 x 50 mL) and purified by column chromatography (silica gel, 2:1→1:1 hexane/ ethyl acetate) to give *tert*-butyl 4-(heptyloxy)aniline (12.7 mmol, 2.64 g, 60%) as a brown oil. R_f=0.3 in 1:1 hexane/ethyl acetate. ^{1}H NMR (400 MHz, CDCl$_3$, 25°C, TMS): δ=6.8 -6.7 (m, 2H), 6.7 -6.6 (m, 2H), 3.9 (t, J(H,H)=7 Hz, 2H), 3.3 (s, 1H), 1.8 - 1.7 (m, 2H), 1.5 -1.4 (m, 2H), 1.4 -1.2 (m, 6H),
0.9 ppm (t, J(H,H)=7 Hz, 3H).

A solution of 4-(heptyloxy)aniline (6.51 mmol, 1.35 g) in glacial acetic acid (5.0 mL) is treated with concentrated hydrochloric acid (14.7 mL) and cooled to 0 °C. A solution of sodium nitrite (6.51 mmol, 0.45 g) in water (1.5 mL) is added over a period of 10 minutes and the reaction is stirred for one hour at 0° C. A solution of tin (II) chloride dihydrate (14.3 mmol, 3.23 g) in concentrated hydrochloric acid (3.5 mL) is added dropwise over a period of 15 minutes. After stirring for three hours at 0 °C, the precipitate is collected by filtration and dissolved in a saturated aqueous solution of potassium carbonate (200 mL). The composite is extracted with dichloromethane (4 × 50 mL). The combined organic phases are washed with a saturated aqueous solution of sodium chloride and dried over sodium sulfate. The crude product is used without further purification. The crude product (5.58 mmol, 1.30 g) is dissolved in dry acetonitrile (10 mL) and treated with di-*tert*-butyl dicarbonate (6.44 mmol, 1.40 g) under argon atmosphere. After complete consumption of the reactants, as monitored by TLC, the solvent is removed under reduced pressure. The residue is subjected to column chromatography (silica gel, 20:1→10:1→5:1 hexane/ethyl acetate) to give *tert*-butyl 2-(4-(heptyloxy)phenyl)hydrazine-1-carboxylate (2.86 mmol, 0.92 g, 44%) as a yellow oil. R_f=0.3 in 8:1 hexane/ethyl acetate. ^{1}H NMR (400 MHz, CDCl$_3$, 25°C, TMS): δ=6.8 – 6.8 (m, 4H), 6.4 (s, 1H), 3.9 (t, J(H,H)=7 Hz, 2H), 1.8 – 1.7 (m, 2H), 1.5 – 1.3 (m, 17H), 0.9 ppm (t, J(H,H)= 7 Hz, 3H).

To a stirred solution of 2-(4-(heptyloxy) phenyl) hydrazine-1-carboxylate (1.97 mmol, 0.63 g) in dry dichloromethane (12 mL), manganese dioxide   (9.83 mmol, 0.86 g) is subsequently added under nitrogen atmosphere. After complete consumption of the reactants, as monitored by TLC, the mixture is filtered over Celite. Removal of the solvent under reduced pressure and column chromatography (silica gel, 30:1→20:1 hexane/ethyl acetate) give *tert*- butyl 2-(4-(heptyloxy) phenyl) azocarboxylate (1.50 mmol, 0.48 g 76%) as an orange oil. R_f=0.5 (20:1 hexane/ethylacetate). ^{1}H NMR (400 MHz, CDCl$_3$, 25°C, TMS): δ=8.0 – 7.9 (m, 2H), 7.0 – 6.9 (m, 2H), 4.0 (t, J(H,H)=7 Hz, 2H), 1.9 – 1.8 (m, 2H), 1.7 (s, 9H), 1.5 – 1.4 (m, 2H), 1.4 – 1.3 (m, 6H), 0.9 ppm (t, J(H,H)=7 Hz, 3H). ^{13}C NMR (151 MHz, CDCl$_3$, 25°C, TMS): δ=164.1 (C$_q$), 161.3 (C$_q$), 146.0 (C$_q$), 126.4 (2 × CH), 114.9 (2 × CH), 84.5 (C$_q$), 68.7 (CH$_2$), 31.9 (CH$_2$), 29.2 (CH$_2$), 29.2 (CH$_2$), 28.0 (3 × CH$_3$), 26.1 (CH$_2$), 22.7 (CH$_2$), 14.2 ppm (CH$_3$); HR-MS (ESI) calculated for C$_{18}$H$_{28}$N$_2$O$_3$ [M$^+$ + Na$^+$]: 343.1992u, found: 343.1987 u.

tert-Butyl 2-(4-nitrophenyl) carboxylate: (4-nitrophenyl)-hydrazine (70% in water, 6.85 mmol, 1.50 g) is dissolved in dry acetonitrile (5 mL) and treated with di-*tert*-butyl dicarbonate (8.22 mmol, 1.75 g) under nitrogen atmosphere. After complete consumption of the reactants, as monitored by TLC, the solvent is removed under reduced pressure. The residue is dissolved in ethyl acetate (20 mL). After addition of saturated aqueous sodium bicarbonate solution (40 mL), the crude product was extracted with ethyl acetate (3 x 50 mL) and then purified by column chromatography (silica gel, 25:1 dichloromehtane/methanol) to give *tert*-butyl 2-(4-nitrophenyl)hydrazine-1-carboxylate (5.68 mmol, 1.43 g, 83%) as a yellow solid. R_f=0.3 (25:1 dichloromethane/methanol). ^{1}H NMR (400 MHz, CDCl$_3$, 25°C, TMS): δ=8.2 – 8.1 (m, 2H), 6.9 – 6.8 (m, 2H), 6.4 (s, 1H), 1.5 ppm (s, 9).

To a stirred solution of *tert*-butyl 2-(4-nitrophenyl) hydrazine-1-carboxylate (3.71 mmol, 0.94 g) in dry dichloromethane (15 mL), manganese dioxide (18.5 mmol, 1.61 g) is subsequently added under nitrogen atmosphere. After complete consumption of the reactants, as monitored by TLC, the mixture is filtered over Celite. Removal of the solvent under reduced pressure and column chromatography (silica gel 20:1   10:1 hexane/ethyl acetate) give *tert*-butyl 2-(4-nitrophenyl) azocarboxylate (3.69 mmol, 0.93 g, 96%) as an orange solid. R_f=0.4 in 10:1 hexane/ethyl acetate. ^{1}H NMR (400 MHz, CDCl$_3$, 25°C, TMS): δ=8.4 – 8.3 (m, 2H), 8.1 – 8.0 (m, 2H), 1.7 ppm (s, 9H).^{13}C NMR (101 MHz, CDCl$_3$, 25°C, TMS): δ=160.7 (C$_q$), 154.6 (C$_q$), 150.3 (C$_q$), 124.9 (2 × CH), 124.3 (2 × CH), 86.3 (C$_q$), 28.0 (3 × CH$_3$); HR-MS (ESI) calculated for C$_{11}$H$_{13}$N$_3$O$_4$ [M$^+$ + Na$^+$]: 274.0798 u, found: 274.0792 u.

4-Bromobenzenediazonium tetrafluoroborate: The diazonium compound was synthesized according to the literature.[3] 100 mmol of 4-bromoaniline was dissolved in 100 mL of 25 % tetrafluoro bononric acid and added to a solution of 100 mmol NaNO$_2$ in 10 ml water at 0 °C. After mixing both solutions for approximately 30 minutes the precipitation was filtered off and re-dissolved in 50 mL acetone. The final product was precipitated again by the addition of 50 mL of diethyl ether, filtered and vacuum dried.
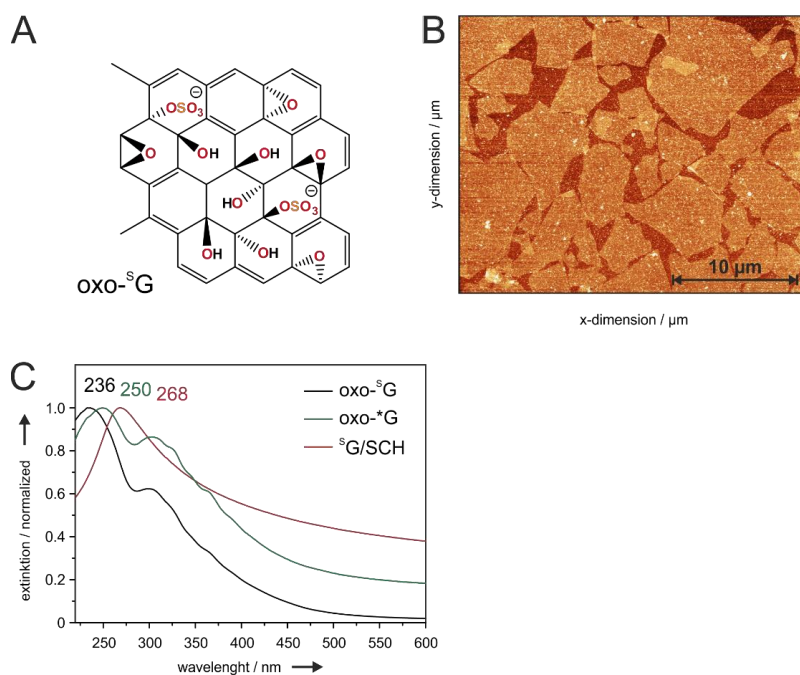
Figure S1: (A) Structure of oxo-^{S}G. (B) AFM image of oxo-G deposited on 300 nm SiO$_2$/Si wafer by Langmuir-Blodgett technique. (C) Normalized UV-vis spectra of aqueous dispersions of oxo-^{S}G, oxo-*G and ^{S}G/SCH.
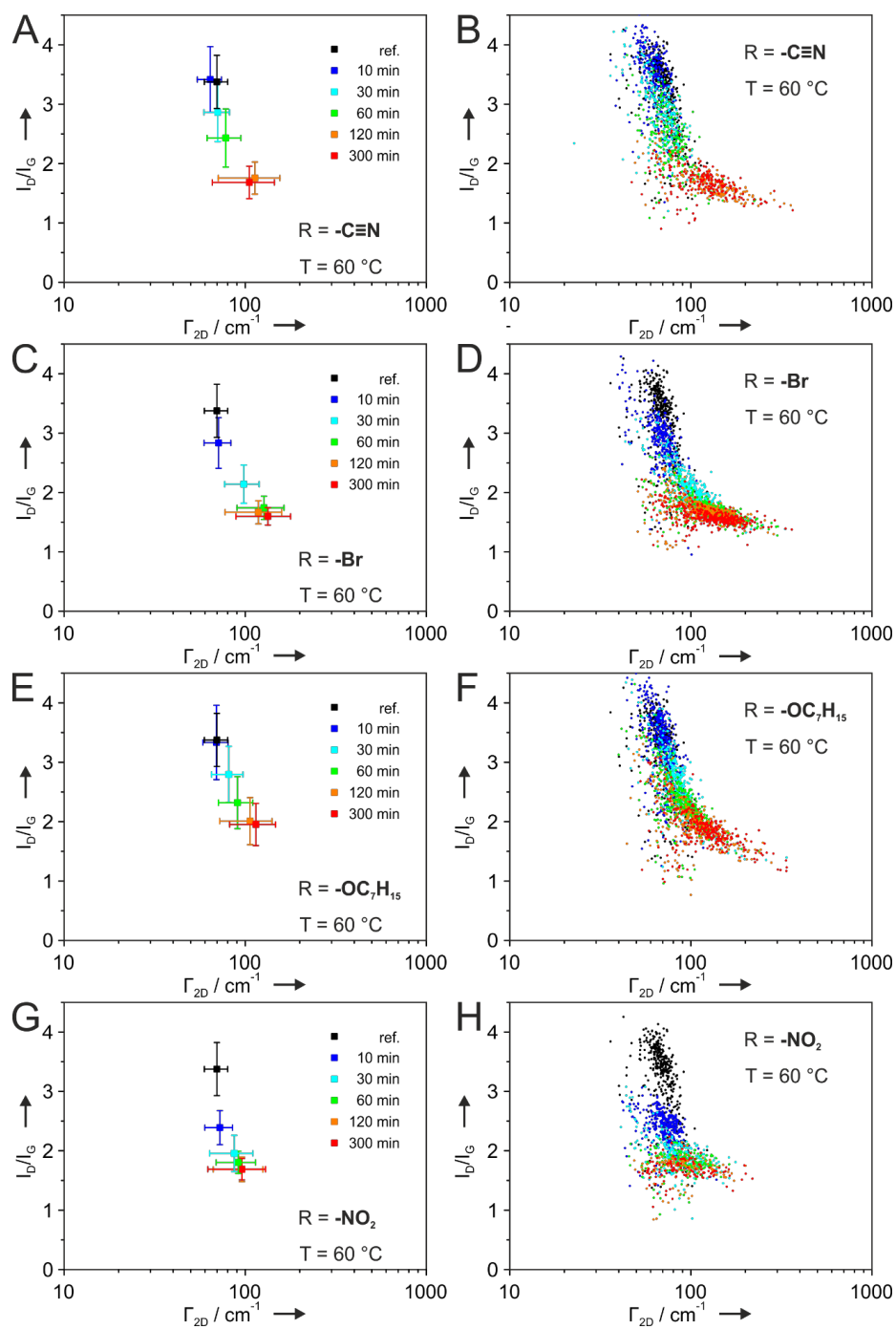
Figure S2: Statistical Raman analysis of functionalized graphene sheets deposited on 300 nm SiO_2/Si wafer. The temperature was 60 °C and the concentration of the 4-phenylazocarboxylic ester was set to 2 mM.
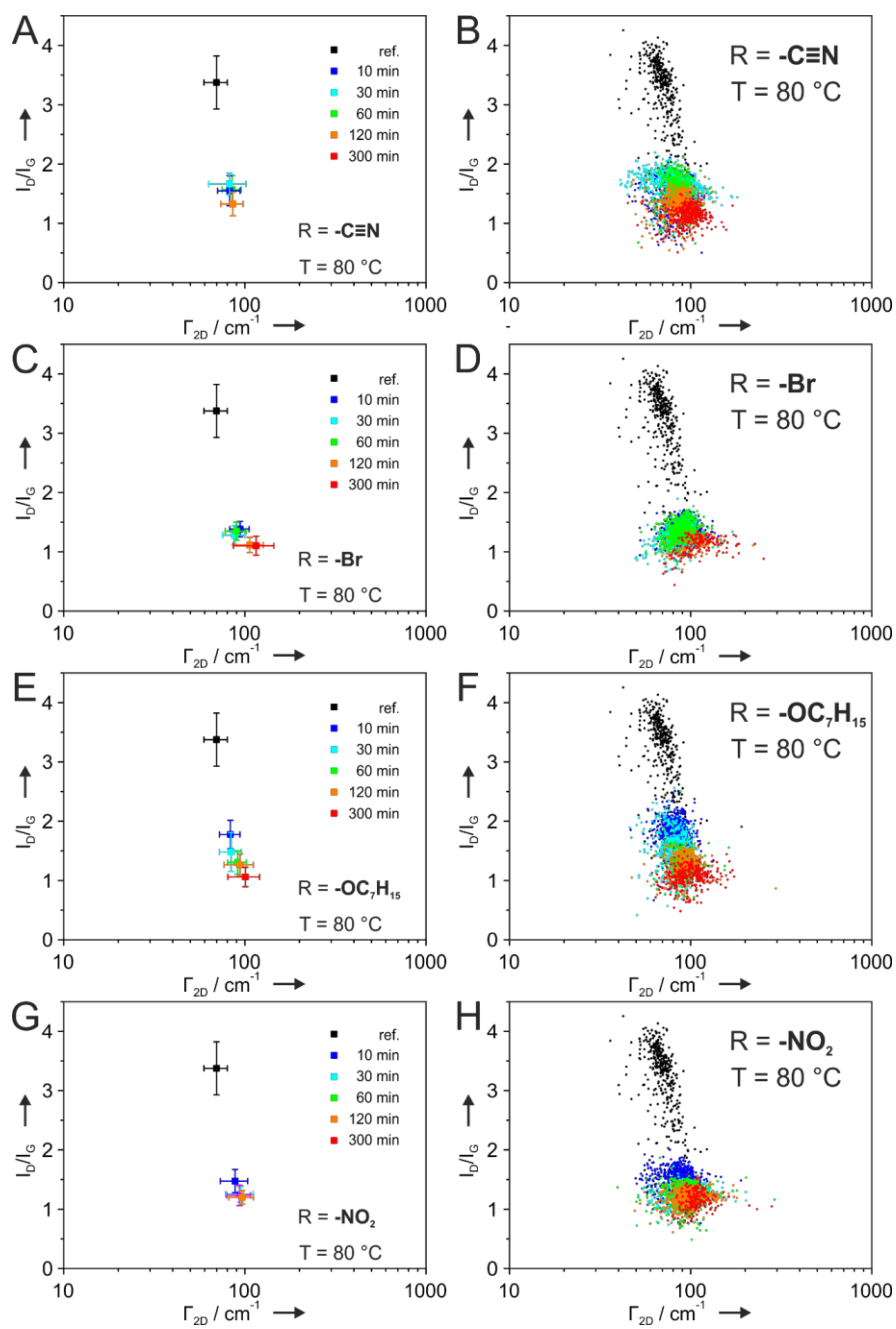
Figure S3: Statistical Raman analysis of functionalized graphene sheets deposited on 300 nm SiO$_2$/Si wafer. The temperature was 80 °C and the concentration of the 4-phenylazocarboxylic was set to 2 mM.
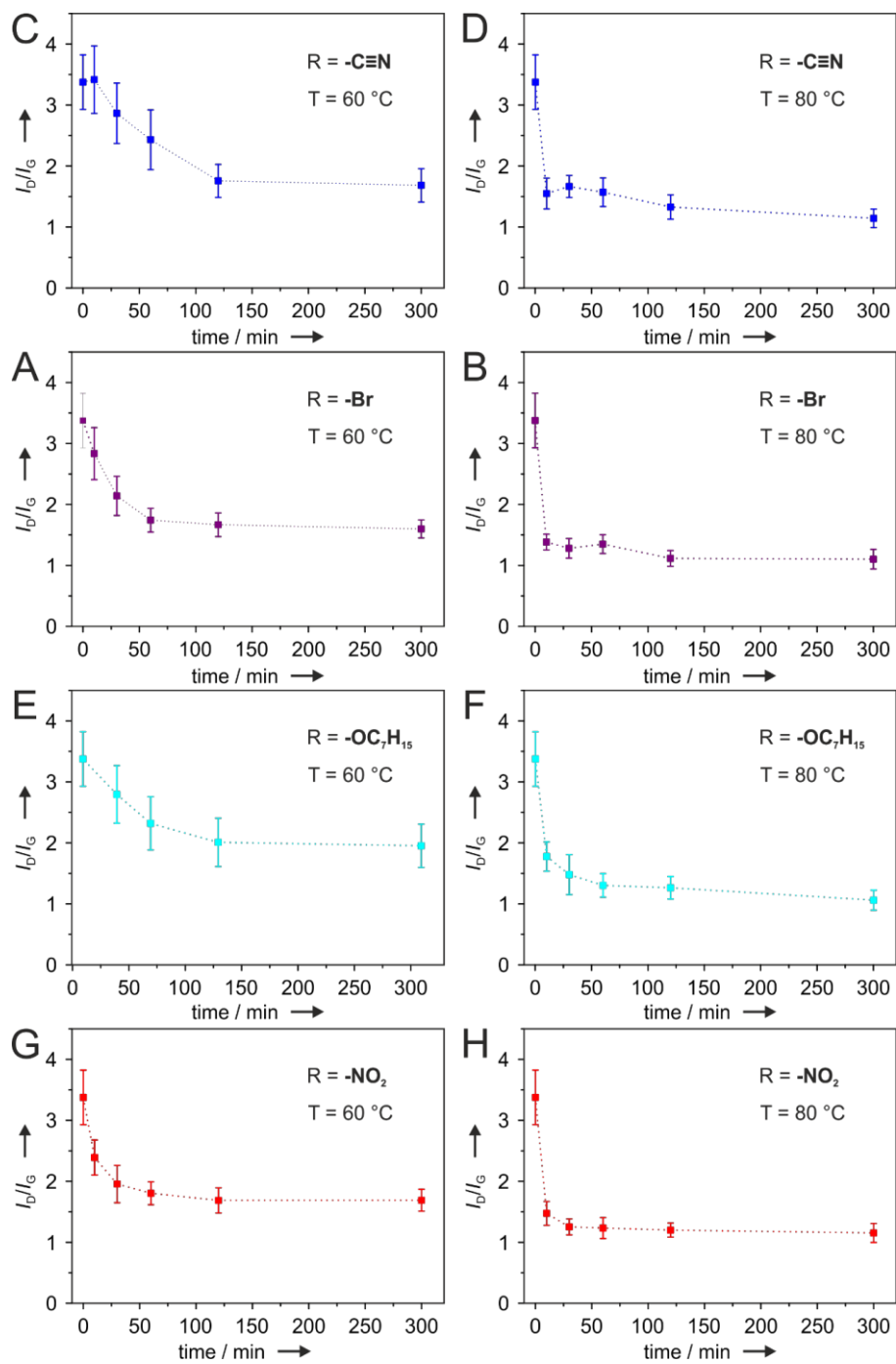
Figure S4: Statistical Raman analysis of functionalized graphene sheets deposited on 300 nm SiO_2/Si wafer after each time step. The temperature was 60 °C (left) and 80 °C (right). The concentration of the 4-phenylazocarboxylic was set to 2 mM.
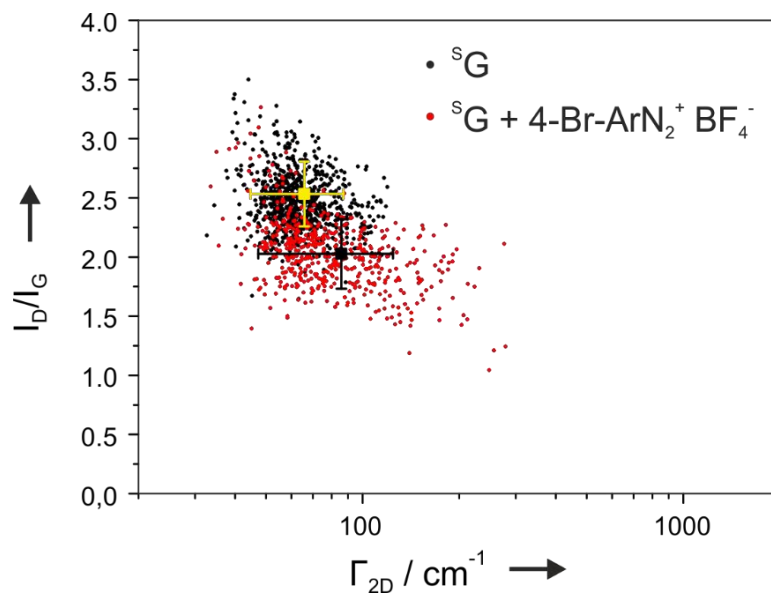
Figure S5: Statistical Raman analysis of functionalized graphene before and after functionalization by 4-Bromobenzenediazonium tetrafluoroborate.
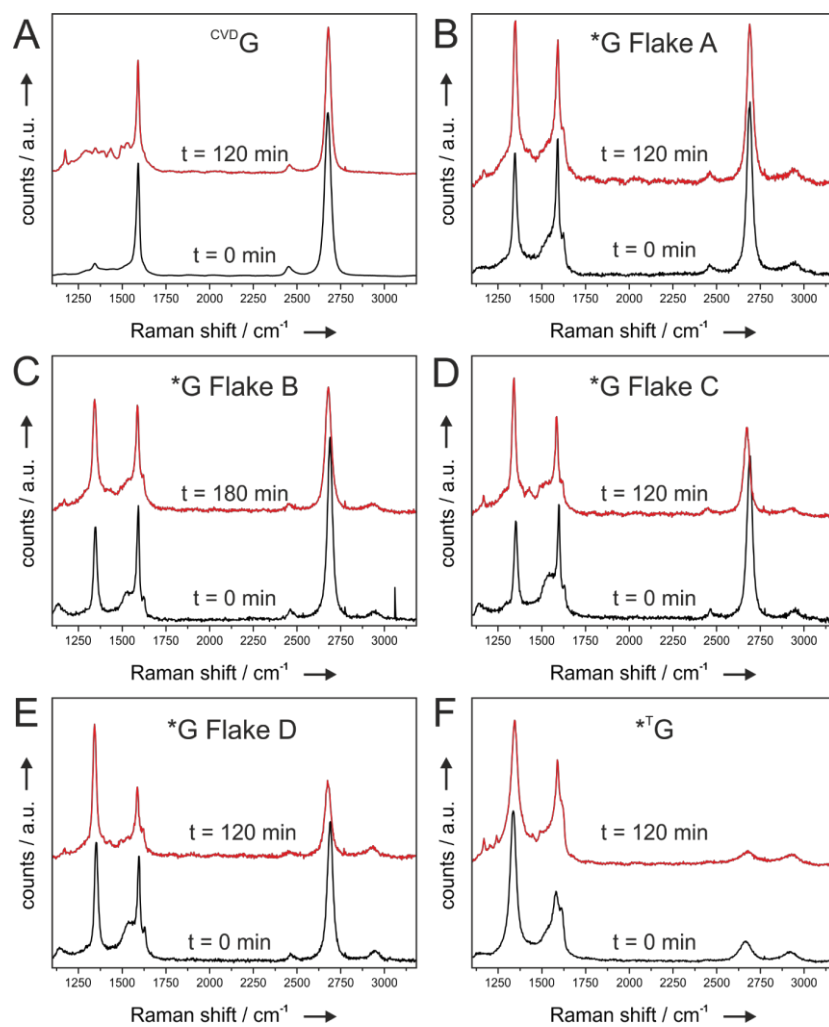
Figure S6: Representative spectra of all recorded flakes of *G and *TG before and after functionalization at 60°C. The reaction times are given in the diagram.
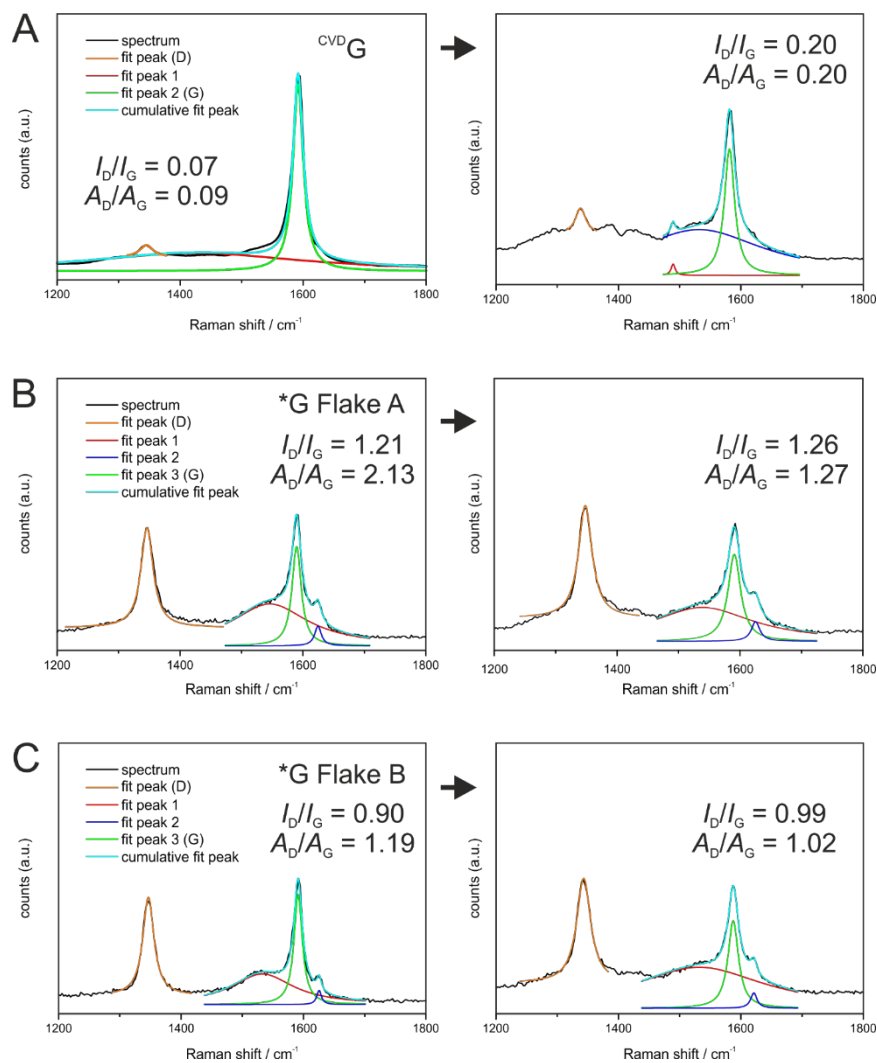
Figure S7: Magnification into the region of the D and G mode of the spectra shown in figure S7. The left spectrum corresponds to the initial flake of *G or *TG, respectively, and the right to the functionalized material. Colored curves represent fits of the individual Raman modes. Corresponding I_D/I_G and A_D/A_G ratios are given for each spectrum.

70
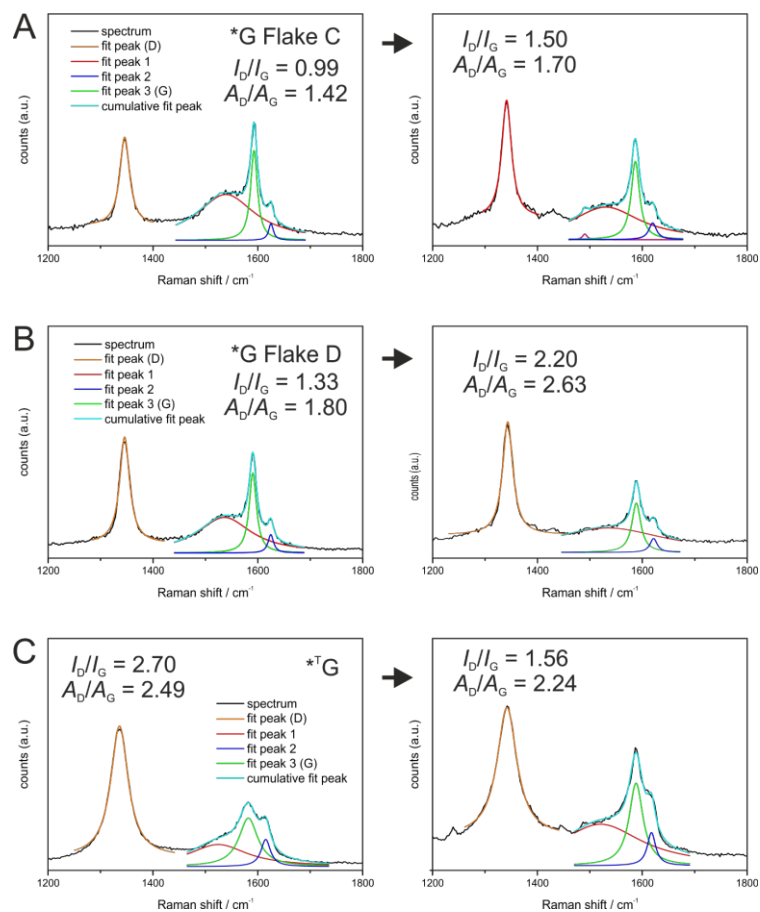
Figure S8: Magnification into the region of the D and G mode of the spectra shown in figure S7. The left spectrum corresponds to the initial flake of *G or ^{*T}G, respectively, and the right to the functionalized material. Colored curves represent fits of the individual Raman modes. Corresponding I_D/I_G and A_D/A_G ratios are given for each spectrum.
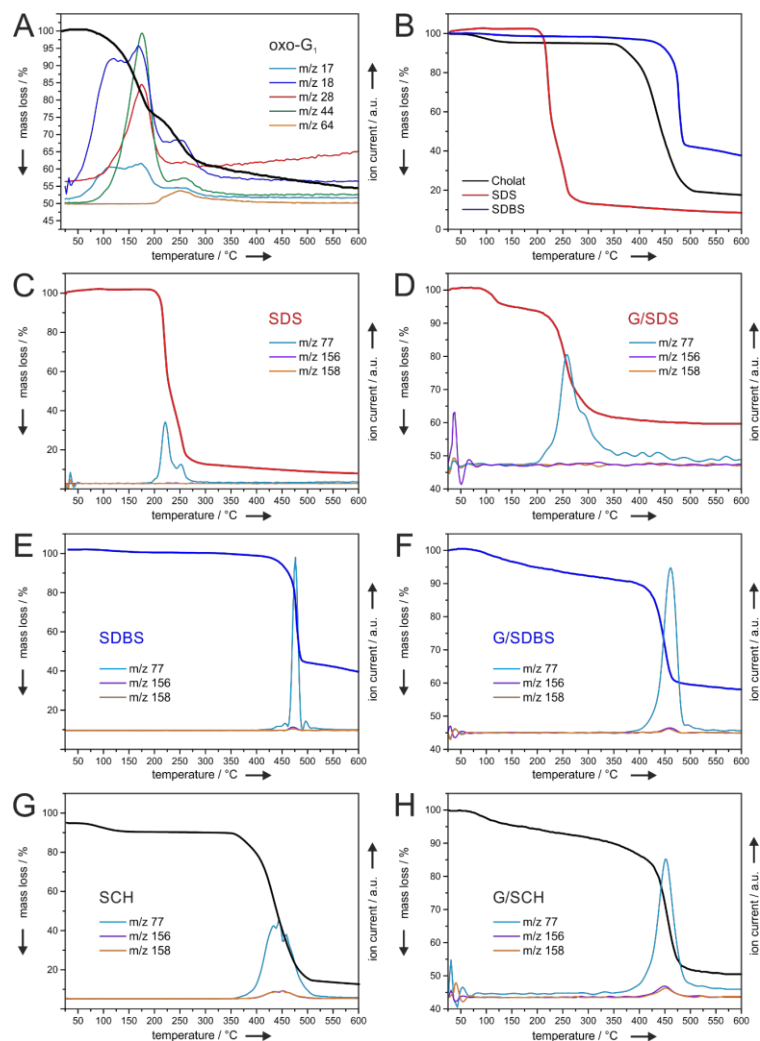
Figure S9: TGA-MS of oxo-G$_1$, thereout produced G/Surfactant compounds used for functionalization and the pure surfactants as references: (A) initial oxo-G: TG-curve (black) and corresponding ion currents (colored). (B) TGA of SDS, SDBS and SCH. **(C-H)** Pairs of surfactants (SDS, SDBS and SCH) and their corresponding graphene-surfactant-compound. The fragments shown by their m/z values 77/156/158 can either be referred to cleaved aromatic fragments after functionalization and also to decomposition products of the used surfactants and therefore shown in each diagram.
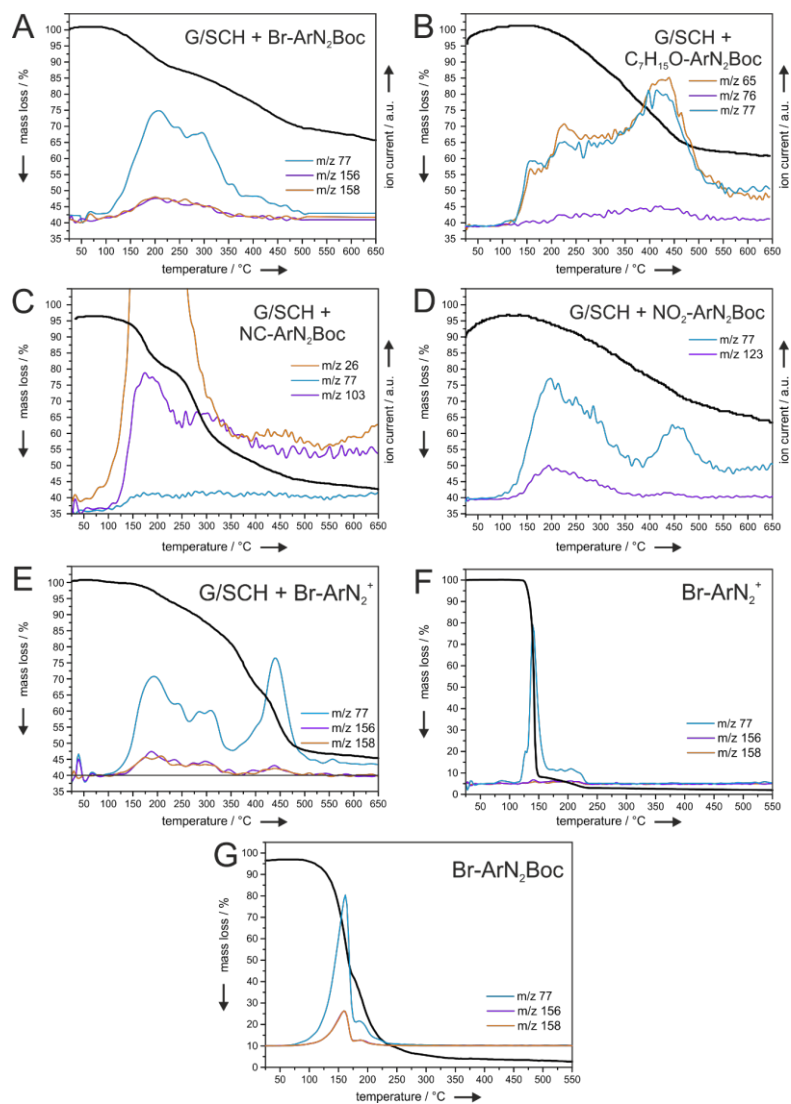
Figure S10: TGA-MS of all arylated graphene-surfactant-compounds in bulk. (A) graphene functionalized with 4-bromophenyl azocarboxylic ester, (B) 4-heptyloxy phenyl azocarboxylic ester, (C) 4-nitrophenyl azocarboxylic ester, (D) 4-nitrophenyl azocarboxylic ester. (E) Graphene functionalized with 4-bromobenzenediazonim tetrafluoroborate as a reference. (F-G) TGA-MS profiles of the initially used 4-bromobenzenediazonium tetrafluoroborate and 4-bromophenylazocarboxylic ester.
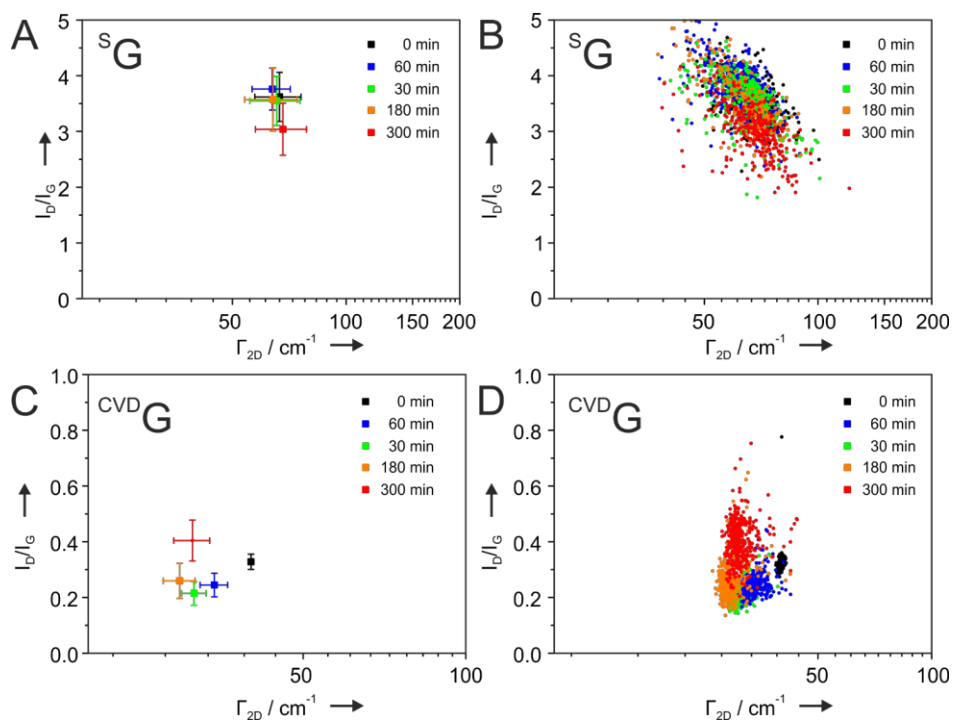
Figure S11: Statistical Raman analysis of ^{CVD}G and ^{S}G, placed in acetonitrile-water mixture (50:50) and trifluoro acetic acid and stored for up to 300 minutes at 60 °C. The reaction conditions are similar to the conditions used to functionalize the graphene derivatives, but without any functionalization agent.

Table S1: Overview of the evaluated spectra obtained by (statistical) Raman spectroscopy for all synthesized and functionalized graphene-based compounds on 300 nm SiO2/Si surfaces. The reaction conditions are annotated in the superscript and the reaction time was 120 minutes. The substituent in para-position of the used ArN2Boc is named first followed by the reaction temperature (60 °C or 80 °C). The degree of functionalization for oxo-G is estimated from elemental analysis and for and oxo-*G taken from the literature.

compound	I_D/I_G	Γ_{2D} [cm-1]	L_D (nm)	Θ
oxo-^{S}G	1.11±0.04	200±54	<< 1	> 50 %
oxo-*G	0.98	>150	<< 1	~ 4 %
^{S}G/SCH	1.98	>150	1.7	0.93 %
*^{T}G	2.70	81	2.0	0.7 %
^{S}G	3.38±0.45	70±10	2.3	0.5 %
*G (average)	1.10	36	10.8	0.02 %
^{CVD}G	0.12	39	34.7	0.002 %
*G^{Br-60}	1.49	40	9.1	0.032 %
*$^TG^{Br-60}$	1.56	89	1.4	1.14 %
$^{CVD}G^{Br-60}$	0.20	32	26.8	0.0036 %
$^SG^{Br-60}$	1.67±0.19	118±41	1.6	1.09 %
$^SG^{Br-80}$	1.12±0.13	106±20	1.4	1.43 %
$^SG^{NO2-60}$	1.68±0.21	96±29	1.6	1.08 %
$^SG^{NO2-80}$	1.19±0.12	97±15	1.4	1.36 %
$^SG^{CN-60}$	1.76±0.27	113±42	1.6	1.05 %
$^SG^{CN-80}$	1.33±0.20	86±12	1.4	1.28 %
$^SG^{OC7H15-60}$	2.00±0.40	106±34	1.7	0.94 %
$^SG^{OC7H15-80}$	1.27±0.18	94±17	1.4	1.31 %

[1] a) C. E. Halbig, T. J. Nacken, J. Walter, C. Damm, S. Eigler, W. Peukert, Carbon 2016, 96, 897; b) H. Pieper, S. Chercheja, S. Eigler, C. E. Halbig, M. R. Filipovic, A. Mokhir, Angew. Chem. Int. Ed. 2016, 55, 405; c) C. E. Halbig, P. Rietsch, S. Eigler, Molecules 2015, 20, 21050.

[2] Organic Syntheses 1939, 19, 40.

[3] P. S. Gribanov, M. A. Topchiy, Y. D. Golenko, Y. I. Lichtenstein, A. V. Eshtukov, V. E. Terekhov, A. F. Asachenko, M. S. Nechaev, Green Chemistry 2016, 18, 5984.

tert-Butyl 2-(4-cyanophenyl) azocarboxylate (^{1}H and DEPTQ NMR in CDCl$_3$)
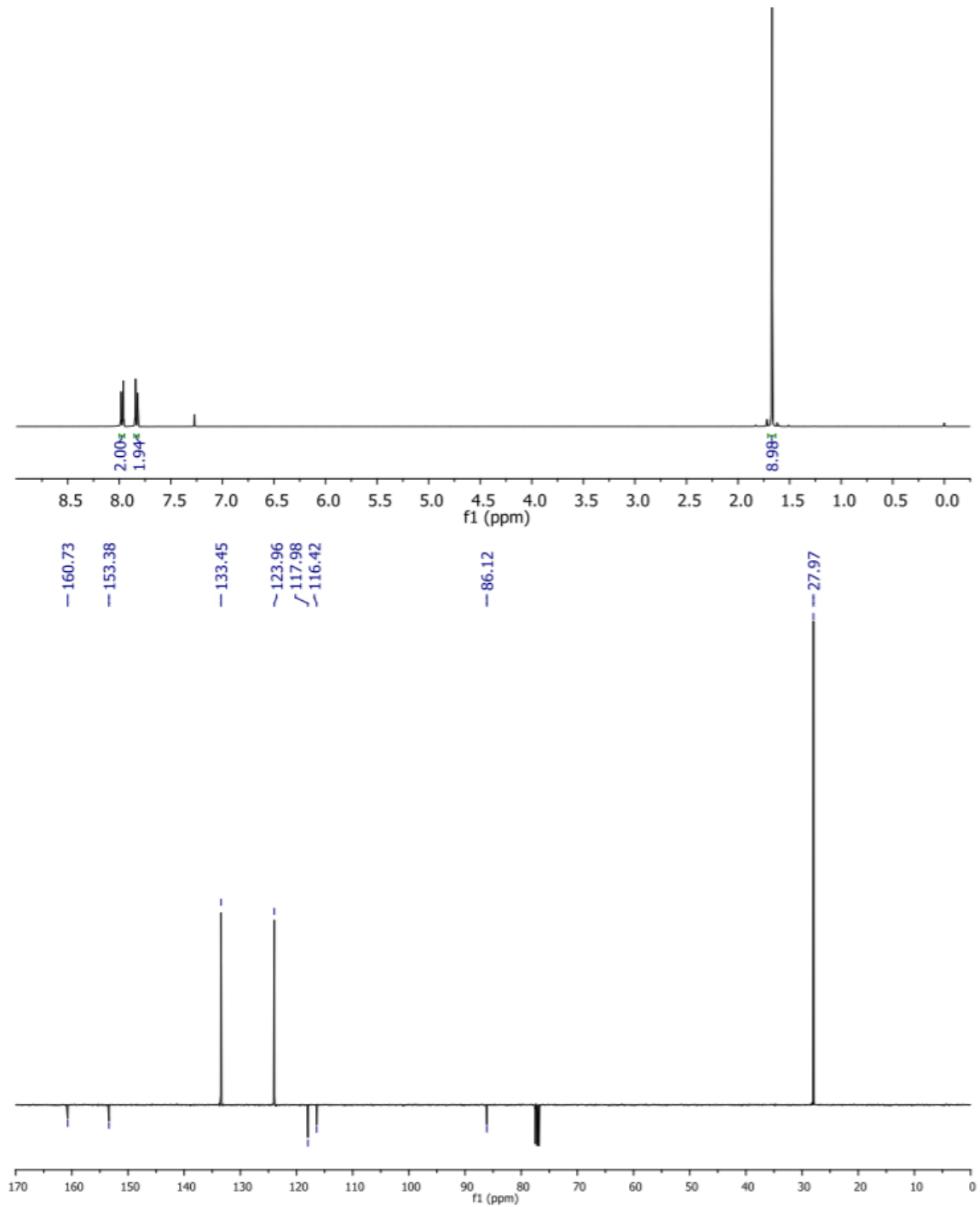
tert-Butyl 2-(4-bromophenyl) azocarboxylate (^{1}H and DEPTQ NMR in CDCl$_3$)
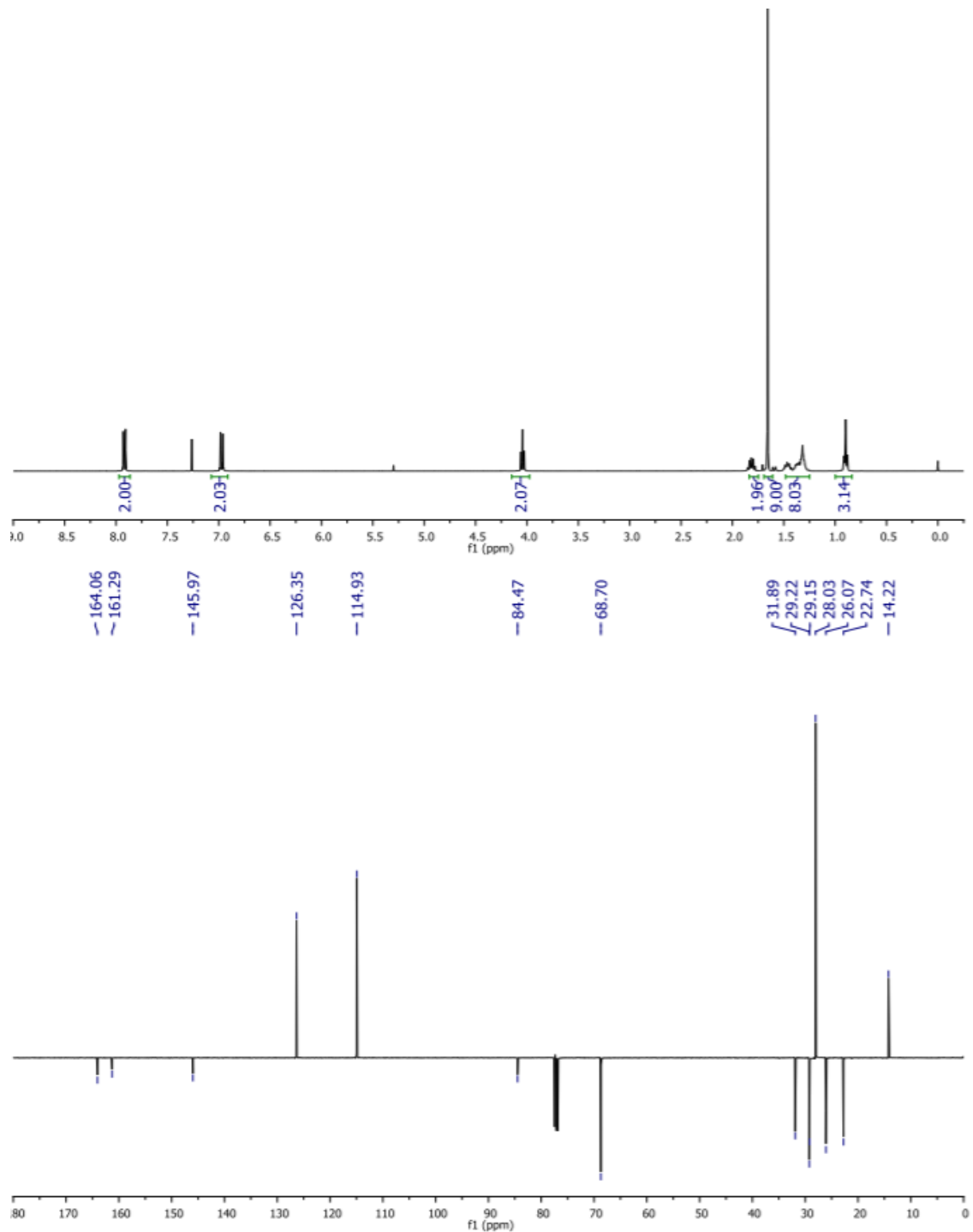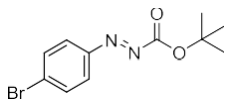
tert-Butyl 2-(4-(heptyloxy) phenyl) azocarboxylate (^{1}H and DEPTQ NMR in CDCl$_3$)
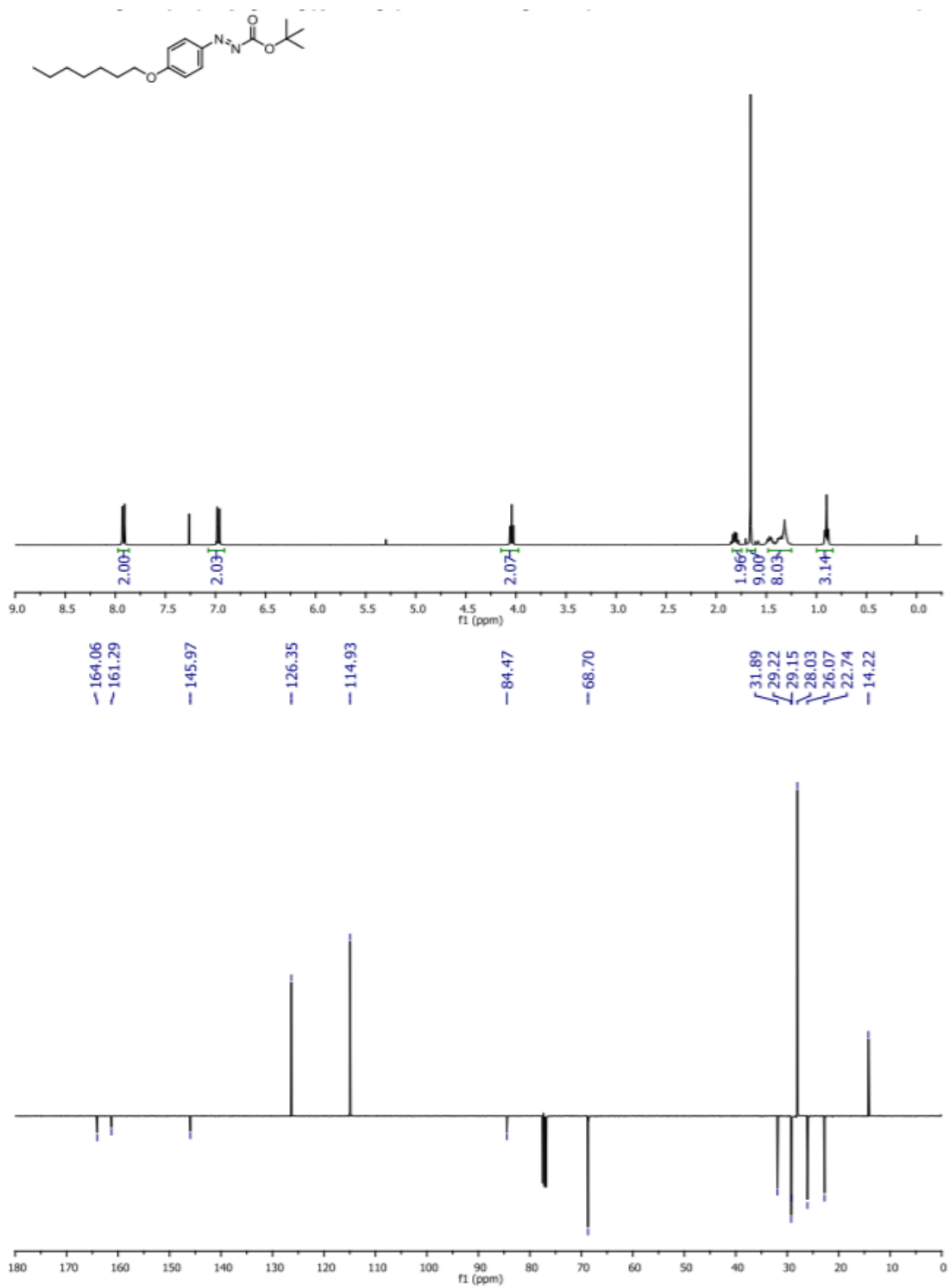
tert-Butyl 2-(4-nitrophenyl) azocarboxylate (^{1}H and DEPTQ NMR in CDCl$_3$)
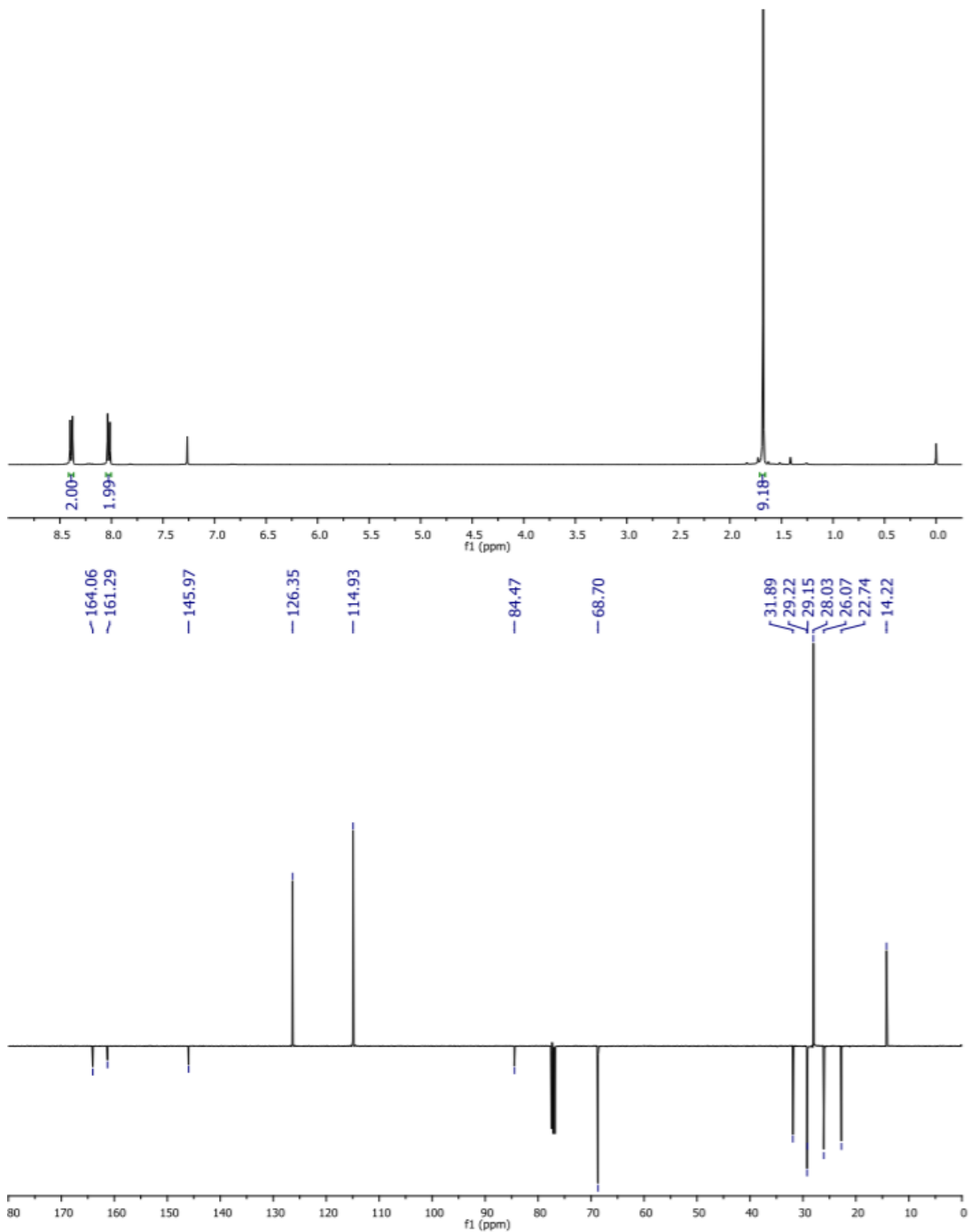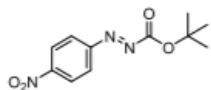
4.1.2. Functionalization of oxo-G by non-covalently bound π-Systems

Title:	Evidence for Electron Transfer between Graphene and Non-covalently Bound π-Systems
Authors	Steffen M. Brülls, Valentina Cantatore, Zhenping Wang, Pui Lam Tam, Per Malmberg, Jessica Stubbe, Biprajit Sarkar, Itai Panas, Jerker Mårtensson and Siegfried Eigler
Under review	Chem. Eur. J. A
Detailed scientific contribution	Preparation of reduced-oxo-G field effect transistors for electrical transport measurements was finished by me. AFM and electrical transport characterizations were done by me. The description of electrical performance in the manuscript was finished by me.
Estimated own contribution	~ 20%

Evidence for Electron Transfer between Graphene and Non-covalently Bound π-Systems

Steffen M. Brülls,[a] Valentina Cantatore,[a] Zhenping Wang,[b] Pui Lam Tam,[c] Per Malmberg,[a] Jessica Stubbe,[d] Biprajit Sarkar,[d],[e] Itai Panas,[a] Jerker Mårtensson,[a] and Siegfried Eigler*[b]

Abstract: Hybridizing graphene and molecules possess a high potential for developing materials for new applications. However, new methods to characterize such hybrids must be developed. Herein, we present the wet-chemical non-covalent functionalization of graphene with cationic π-systems and characterize the interaction between graphene and the molecules in detail. A series of tricationic benzimidazolium salts with various steric demand and counterions was synthesized, characterized and used for the fabrication of graphene hybrids. Subsequently, the doping effects were studied. The molecules are adsorbed onto graphene and studied by Raman spectroscopy, XPS as well as ToF-SIMS. The charged π-systems show a p-doping effect on the underlying graphene. Consequently, the tricationic molecules are reduced *via* a partial electron transfer process from graphene, a process which is accompanied by the loss of counterions. DFT calculations support this hypothesis and the strong p-doping could be confirmed in fabricated monolayer graphene/hybride FET devices. The results are the basis to develop sensor applications, which are based on analyte/molecule interactions and effects on doping.

Introduction

[a]   M. Sc. Steffen Marc Brülls, Dr. Valentina Cantatore, Dr. Per Malmberg, Prof. Dr. Itai Panas, Prof. Dr. Jerker Mårtensson
Department of Chemistry and Chemical Engineering
Chalmers University of Technology
Kemivägen 10, 41296 Gothenburg (Sweden)

[b]   Prof. Dr. Siegfried Eigler, M. Sc. Zhenping Wang
Institut für Chemie und Biochemie
Freie Universität Berlin
Takustraße 3, 14195 Berlin (Germany)
E-mail: siegfried.eigler@fu-berlin.de

[c]   Dr. Pui Lam Tam
Department of Industrial and Materials Science
Chalmers University of Technology
Rännvägen 2A, 41296 Gothenburg (Sweden)

[d]   M. Sc. Jessica Stubbe, Prof. Dr. Biprajit Sarkar
Institut für Chemie und Biochemie
Freie Universität Berlin
Fabeckstraße 34/36, 14195 Berlin (Germany)

[e]   Prof. Dr. Biprajit Sarkar
Institut für Anorganische Chemie
Universität Stuttgart
Pfaffenwaldring 55, D-70569 Stuttgart (Germany)

     Supporting information for this article is given via a link at the end of the document.

Graphene is part of growing interdisciplinary research, bridging natural sciences and material sciences.[1] In a graphite crystal, several sheets of graphene are stacked on top of each other with an interlayer distance of 3.35 Å.[2] Single graphene sheets, a two-dimensional (2D) material, can be exfoliated from graphite. In analogy, other 2D materials can be produced by exfoliation. Up to now, graphene is the best studied 2D material.[3] Graphene is characterized by its unique properties such as mechanical strength,[4] electrical,[5] optical and magnetic properties, which are linked to its chemical structure. Its broad spectrum of properties allows graphene to be used in a series of applications, including amongst others high-frequency transistors,[6] high-performance capacitors,[7] transparent electrodes,[8] the field of sensors[9] and energy applications.[10] Moreover, 2D materials can form van der Waals heterostructures, by stacking different 2D materials on top of each other by single layer flake transfer.[11] These artificially assembled layered structures form systems analogous to pristine layered 2D materials.[12] The resulting properties of stacks differs from those of the individual 2D materials. By using molecules attached to 2D materials, the horizon of van der Waals heterostructures broadens,[13] because the individual design of molecules leads to materials with desired electronic, optical and magnetic properties. Molecules affect the electronic properties of the 2D materials strongly,[14] in contrast to adsorbed molecules on e.g. graphite, where molecules change the interface properties, but not the bulk properties of graphite. The interface between the 2D materials and the molecules plays an important role in the performance of an electronic device.
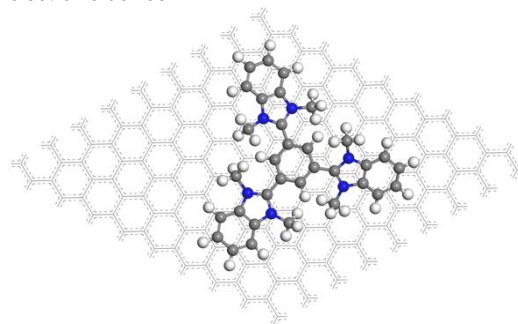

Figure 1. Optimized structure for tricationic molecule **6** (without counterions) non-covalently attached to a 9 × 9 supercell of graphene in top-view.

Although a plethora of 2D materials is currently in the focus of research and many more can be imagined to exist,[15] the number of accessible molecules is orders of magnitude larger. The field of

graphene organic hybrid electronics is growing,[16] however not fully developed and the materials produced are not extensively characterized. Here we report on the wet-chemical non-covalent functionalization of graphene using star-shaped cationic *N*-hetero-π-systems (**Figure 1**). These aromatic conjugated systems form a stable molecular layer on graphene. A partial electron transfer from graphene to the underlying graphene results in a p-doping of the graphene. The results are confirmed by DFT calculations, AFM, XPS, ToF-SIMS, cyclic voltammetry and electrical transport measurements.

Results and Discussion

Star-shaped cationic *N*-hetero-π-systems were synthesized with different counterions, namely 1,3,5-tris-benzimidazolium benzene derivatives with I⁻, BF₄⁻ and OTf⁻, respectively. As depicted in **Scheme 1A** and described in literature,[17] trimesic acid **1** was condensed with either *o*-phenyldiamine **2** or *N*-methyl phenyldiamine **3** in phosphoric acid to yield 1,3,5-tris(benzimidazolyl) benzene **4** or 1,3,5-tris (*N*-methyl-benzimidazolyl) benzene **5**, respectively.
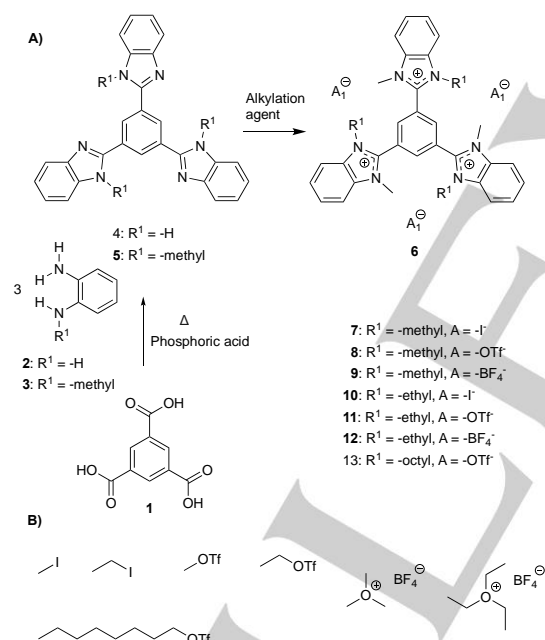
Scheme 1. A) Synthesis of cationic molecules from either 1,3,5-tris (benzimidazolyl)benzene **4** or 1,3,5-tris(*N*-methyl benzimidazolyl)benzene **5** in the presence of various B) alkylation agents to introduce methyl, ethyl, and octyl substituents with either iodide, tetrafluoroborate or triflate counterions.

Both compounds were converted into trications **6** *via* *N*-quaternization using alkylation agents to introduce various substituents and counterions (**Scheme 1B**). The synthetic protocols and the characterization of all compounds shown in Scheme 1, including NMR and

MS are summarized in the supporting information (**Figure S1-S23**). The obtained molecules (**7-13**, **Scheme 1**) where used to non-covalently functionalize graphene. Both, graphene prepared by CVD (chemical vapor deposition) method[18] and graphene prepared by chemical reduction of oxo-functionalized graphene (r-oxo-G) samples were used to enable reliable and complementary analyses.[19] We introduced oxo-G in recent years and the material differs from common graphene oxide by a more defined surface chemistry and by a controlled density of in-plane lattice defects, by minimized over-oxidation. The here used r-oxo-G is graphene with a density of lattice defects of about 0.5-0.8%, according to statistical Raman spectroscopy. The non-covalent modification of graphene was accomplished by incubating a silicon wafer with deposited graphene, either CVD graphene or r-oxo-G, in a 12 mM methanol solution of the respective tricationic molecule for 2 hours at 4 °C. After incubation, the functionalized graphene wafer was removed from the incubation solution and rinsed with methanol to remove excess of the tricationic molecules. An overview of different sample preparations is summarized in the supporting information.
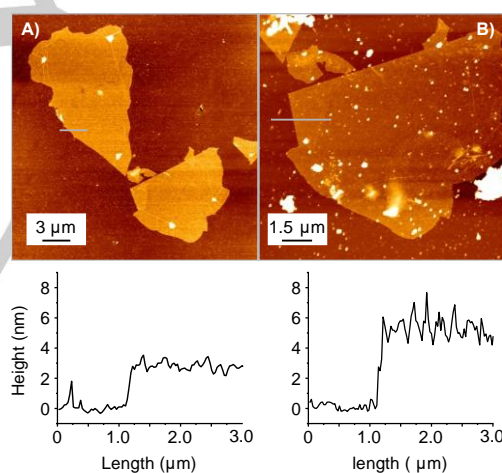
Figure 2. AFM image from r-oxo-G flake A) before and B) after functionalization with **8**. Height profiles along grey lines are shown below the AFM images.

To determine the topology of the functionalized graphene samples, AFM studies were performed (**Figure 2**). Before functionalization, the thickness of flakes of r-oxo-G is about 2.5 nm (**Figure 2A**).[20] After non-covalent functionalization, the thickness of the r-oxo-G/hybrid increases to about 5 nm, as shown in the height-profile of **Figure 2B**. We note that the reference experiment using the uncharged compound **4** for non-covalent functionalization of r-oxo-G also results in an increase of thickness from 2.5 nm to about 3.5 nm (**Figure S36**). Due to the

polar nature of the benzimidazole moiety and hydrogen-bond acceptor function, it seems likely that water molecules or methanol molecules can be adsorbed under ambient conditions. Although some contaminants are visible on the surface of the flakes of the r-oxo-G/hybrid the roughness and measured height is overall homogeneous after functionalization. Thus, the AFM results indicate that molecules form indeed films and do not cluster to aggregates.

The existence of the tricationic molecules on the surface of r-oxo-G/hybrid was further studied by Time-of-Flight secondary ion mass spectrometry (ToF-SIMS) analysis. The adsorbed tricationic molecules can be identified by ToF-SIMS analysis. An area of 150 µm x 150 µm of a film of flakes of r-oxo-G/**8** (notation: material on bottom and molecules on top) was scanned in positive mode. The most prominent signal observed was m/z = 811.16, which can be related to **8** through the loss of one of its counterions. As shown in **Figure 3A** (red color) the flake-like pattern is revealed. The appearance of the m/z signal all over the flake with almost constant intensity confirms the homogeneous non-covalent functionalization of the r-oxo-G. In addition, no signal is found on the bare SiO_2 surface, indicating that molecules are only adsorbed on the r-oxo-G flake. Thus, these observations corroborate the height profiles obtained by AFM measurements. Also, although with lower signal intensity, signals were observed at m/z = 662.73 and m/z = 513.28 corresponding to the mass of the trication without 2 and 3 counterions, respectively, (**Figure S31-S35**). In addition, ToF-SIMS was conducted in negative ion mode to detect the triflate counterion with m/z = 148.95. The map of **Figure 3B** depicts also that triflate ions are located on the r-oxo-G flakes (red color).
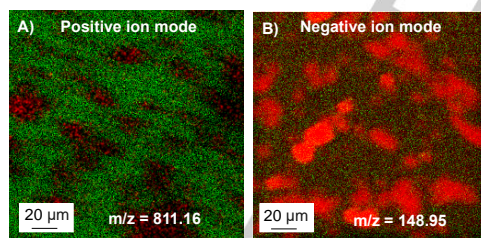
Figure 3. A) ToF-SIMS image in positive ion mode showing the once reduced **8** on reduced oxo-G on silicon substrate in a flake-like pattern. Red: m/z 811.16, green: Si+. B) ToF-SIMS image in negative mode showing the triflate anion from **8** on reduced oxo-G on silicon substrate in a flake-like pattern. Red: m/z 148.95, green: Si-.

Raman spectray were recorded to monitore signatures of the molecules on SiO_2 surface and on graphene surface.[21] The Raman spectra of 1,3,5-tris(*N*-methylbenzimidazolyl) benzene **8** on SiO_2 substrate (**Figure 4A**) show aromatic C-H bond vibrations in the region between 2980-3020 cm⁻¹ , C=N bond vibrations between 1610-1680 cm⁻¹ and aromatic ring vibrations between 1450-1610 cm⁻¹. The bond vibrational signals at 1170-1410 cm⁻¹ and

between 670-780 cm⁻¹ stem from the C-F and C-S bonds, respectively, in the triflate counterions.[22] Neat graphene shows two distinct Raman peaks, the G peak at about 1584 cm⁻¹ and the 2D peak at around 2700 cm⁻¹ (**Figure 4B, S24**).[23] For this study, CVD graphene was used because its Raman peaks are sharper compared to the peaks for r-oxo-G. Thus, the choice of CVD graphene reduced the interfering overlap with other peaks in the subsequent analysis. Raman spectra from non-covalently functionalized graphene show the presence of broad and overlapping signals between 1200-1600 cm⁻¹, which stem from molecule **8** (**Figure 4C**). Raman spectra for the systems composed of trication **8** (without counterions, 8^{3+}) or the reduced form of **8** (dicationic species 8^{2+}, without counter ions) on graphene computed on the density functional theory (DFT) level of theory support this interpretation (**Figure S39**). Reference Raman measurements on r-oxo-G/**8** indicate, in agreement with the ToF-SIMS results, that molecules are only adsorbed on the graphene flakes and not on the bare SiO_2. Raman spectra recorded on CVD graphene and CVD graphene/**8** reveals that **8** is adsorbed on graphene. Analysis of the shift of the position of the G peak, which is sensitive to doping,[24] is not reliable due to overlapping signals (**S25**). Instead, the 2D peak is analyzed statistically for CVD graphene and CVD graphene/**8**, respectively (**Figure S26**).
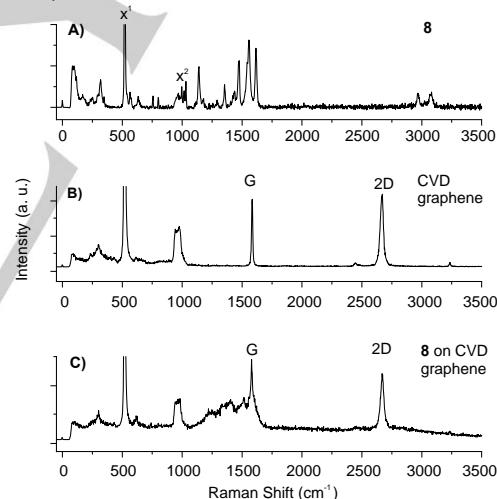

Figure 4. Raman spectra of A) tricationic molecule **8**, B) CVD graphene and C) trication molecule **8** on CVD graphene. As substrate for all samples silicon wafer (300nm of SiO_2 on surface) were used showing at x^1 = 520 cm⁻¹ the signal for crystalline silicon and at x^2 = 900-1000 cm⁻¹ the signal for amorphous silicon dioxide on the silicon surface.[25] The signal intensities from x^1 are not fully shown.

XPS was used to analyze the composition of the surface of r-oxo-G/hybrid materials.[26] In accordance with the fact that the graphene lattice contains only chemically equivalent carbon (C), the XPS spectrum of pristine graphene on silicon substrate shows

83

a C 1s peak centered at 284.6 eV (**Figure S27**).[27] The observed binding energy is consistent with the sp[2]-hybridized character of the carbon present in graphene, together with minor contribution from certain oxidized states that cannot be completely avoided during the preparation.[27-28] Other observed signals correspond to silicon (Si) and oxygen (O), at 104 eV and 533 eV, respectively,[29] originating from the SiO_2-intersurface in between the graphene layer and silicon substrate. The nitrogen (N) signal observed at 400 eV,[29] likely corresponding to adsorbed molecular nitrogen, is very weak in the case of silicon substrate and is expected to give negligible effects on the latter molecular analysis. Still, this element is of interest for the analysis of those graphene hybrids (i.e. the molecular adsorbates) that contain nitrogen. Depending on the kind of counterion, the adsorbed materials also contain either iodine (I), (i.e. **7**), oxygen (O) and sulfur (S), (i.e. **8, 11**) or boron (B) and fluorine (F) (i.e. **9**, **12**). Comparison among the XPS spectra of pristine graphene, functionalized graphene and the neat molecules on silicon confirms the non-covalent adsorption of the molecular systems on graphene. XPS samples with the neat molecules on substrates were prepared by drop casting a methanol solution of the respective tricationic molecule on a silicon wafer. The preparation of non-covalent modified graphene was described previously.

The XPS spectrum of the neat neutral molecule **4** on silicon shows two binding energies for nitrogen at 398.6 eV and 400.5 eV (**Figure 5A**), respectively. This corresponds to the two chemically different nitrogen atoms in this molecule, i.e. an imine type of nitrogen ($R_2C=NR$) and a secondary amine type of nitrogen atom (R_2-NH). The binding energies for these two nitrogen atoms increase slightly to 399.0 eV and 401.0 eV, respectively, when the molecule **4** is adsorbed on graphene (**Figure 5B**). This implies that the electron density on the neutral molecule is less when adsorbed on CVD graphene as compared to when it is adsorbed on the silicon wafer. This leads to a stronger electron attraction within the molecule chemisorbed on CVD graphene. The corresponding carbon peak position has also increased from 284.7 eV to 285.1 eV when the substrate is CVD graphene (**Figure S28**). The tricationic molecule **8** however shows a different behavior when non-covalently bound to graphene. Due to quaternization, only one N1s signal is expected, i.e. all six nitrogen atoms are chemically equivalent (i.e. iminium type of nitrogen). The XPS data recorded for the tricationic molecule **8** on silicon agrees with this picture (**Figure 6A)**. It shows one major peak at the binding energy 402.1 eV, consistent with imidazolium nitrogen atoms. [30] A second peak of much lower intensity at 400.1 eV is also observed but so far unaccounted for. As this minor peak is also present in the XPS spectra of tricationic molecules **7** and **11** on silicon, it could possibly correspond to an ensemble of tricationic molecules binding to the silicon surface in a distinctly different mode compared to the vast majority. On the other hand, the XPS spectrum obtained for the sample with the tricationic molecule **8** on CVD graphene

show one very broad signal that can be fitted by two components of equal intensity (**Figure 6B**) what is consistent with the presence of two sets of nitrogen atoms in equal amounts but in different states. In accordance with the peak positions, the N1s component around 399.7 eV corresponds to an iminium type state and the other component located around 401.7 eV agrees with the expected imidazolium nitrogen state. As will be discussed later, the two components may correspond to two various nitrogen atoms either facing or pointing away from the graphene. The change in the ratio of the N1s signals also gives information about the doping of graphene by non-covalently molecules. Both p-[31] and n-doping[32] of non-covalently bound molecules on graphene has been shown previously with XPS studies.
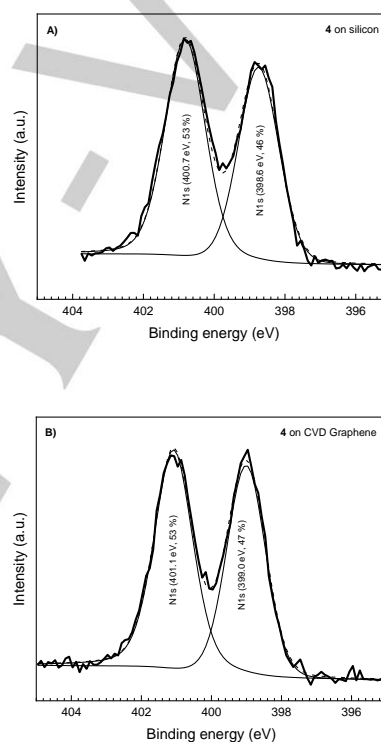

Figure 5. High resolution scan at the N1s region for A) neutral **4** on CVD graphene substrate and B) on silicon substrate.

Doping or charge transfer from graphene to the molecule results in an expanded delocalization of the positive charge into the valence band of graphene and reduced charge density on the molecule. This decreases the coulomb attraction between the anionic counterions and the cationic molecules, which potentially could be observed as an increase in trication to counterion ratio. Thus, we determined the ratios between the trications (i.e. N) and counterions (i.e. I, O, S, B and F) in the samples. The XPS spectrum recorded for trication **8** on silicon gives a ratio among

fluorine, nitrogen and sulphur (F:N:S) of 3:2:1. This is in agreement with an assembly of one trication and three counterions, which corresponds to the molecular formula $C_{36}H_{33}F_9N_6O_9S_3$. After non-covalent binding of **8** to graphene, this ratio changes to 1:3:0. The signal for the sulfur atoms is below the detection limit. The decrease of fluorine and sulfur, which originate from the triflate counterion, indicates that the triflate counterions become more exchangeable and possibly even superfluous. The XPS data recorded for **7**, **11** and **12** on CVD graphene show similar trends (**Figure S29, S30**).

Table 1. Overview of binding energies of the N1s peaks from all with XPS studied tricationic molecules and their graphene/hybrids.

Sample on substrate	Relative intensity (%) / Binding energy (eV)							Atomic ratio
	398.5	399	399.5	400	400.5	401	401.5	
	Imine [30]		Iminium		2nd amine [30]	Imidazol-ium+ [30]		
4 Si		45			55			(n.a.)
CVD	47				53			
7 Si			12			88		N:I 5:4
CVD			41			59		7:1
8 Si				9			91	F:N:S 3:2:1
CVD			52			48		1:3:0
11 Si				4		96		F:N:S 3:2:1
CVD	63					37		1:3:0

Figure 6. High resolution scan at the N1s region for A) neutral **8** on silicon substrate and B) on CVD graphene substrate.

Charge transfer from graphene to the non-covalently bound molecules could explain this observation. Due to the weaker Coulomb attraction some of the counter ions could potentially be removed by rinsing the sample with methanol during the sample preparation, or exchanged by some negatively charged species in the methanol solvent, e.g. methoxide ions. A summary of all tested molecules, depicted in **Scheme 1** (on silicon and on graphene) with their respective binding energies and the elemental content of certain elements is shown in **Table 1**. For all tested tricationic molecules, the elements which are present in the counterions are decreased when adsorbed on CVD graphene.

The redox properties of **9** and **12** were investigated by cyclic voltammetry in acetonitrile (**Figure S40, S41**). Both compounds show several reduction events. The first one-electron reduction of **12** corresponds to a reversible one-electron transfer at $E_{red,1}$ = -1.65 V (**Figure 7A**). These results show that the tricationic molecules are stable after receiving one electron. To support these observations, in situ UV-Vis-NIR spectroelectrochemistry with **12** in acetonitrile was performed. The native form of **12** displays its main absorption bands in the UV region. On one-electron reduction several long wavelength bands in the visible and the NIR region appear **(Figure S42)**. Such long wavelength bands are usually a sign for the generation of radical species.

Figure 7B shows both, the absorption spectrum for the native **12** and for the reoxidized species of **12**. The uniform overlap of both spectra indicates that the same species was analyzed and that the first reduction event is reversible.
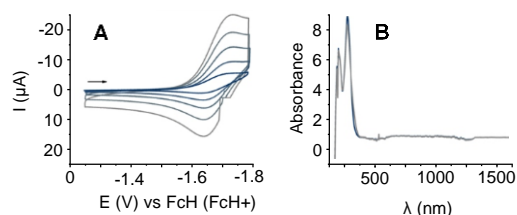
Figure 7. A) Cyclic voltammogram of first reduction peak from **12** at $E_{red,1}$ = -1.65 V) (different scan rates 25-1000 mVs^{-1}) in ACN with 0.1 M (Bu$_4$NPF$_6$) vs. FcH/FcH$^+$. B) UV-Vis-NIR spectroelectrochemistry of **12** in ACN showing both, the absorption spectrum of the native species of **12** (blue) and of the reoxidized species of **12** (grey).

For the purpose of rationalizing the experimental observations, computational quantum mechanical modelling was performed to gain insight into the interaction between tricationic molecules and graphene. A single molecule of **8** (without counterions) on top of a 9 × 9 supercell of graphene served as the unit cell in our model system. Density functional theory with periodic boundary calculations was used to study the overall electron distribution in the system. The optimized geometry of **8** alone at the same level of sophistication is propeller shaped, characterized by an average dihedral angle of 53.2° (44.7°, 55.9°, 59.02°) between the central benzene ring and the appended benzimidazolium moieties (**Figure 8A**). These dihedral angles are reduced markedly, to 24.4° (19.35°, 24.17°, 29.64°), when one additional electron is added to the trication, in its LUMO, reducing the molecular charge from +3 to +2. The optimized geometry of the **8**$^{2+}$ species is considerably more planar and has a larger resemblance to the optimized molecular geometry obtained for the trication–graphene unit cell (**Figure 8B**) than that of the trication itself (**Figure 8A**). This indicates that binding of the trication to the graphene surface may be accompanied by transfer of some electron density from graphene to the trication.

A) 8

B) 8 on Graphene
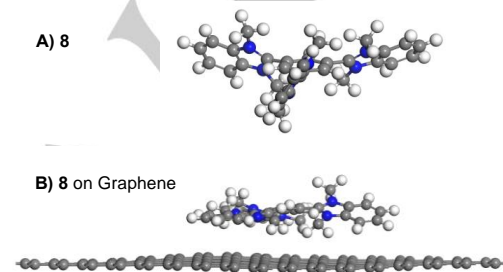
Figure 8. Optimized geometry of A) tricationic **8** (without counterions) and B) **8** non-covalent attached to graphene.

To identify the effect of electron transfer, calculations were performed with different overall charges (neutral, **8**$^{1+}$, **8**$^{2+}$ and **8**$^{3+}$) of the unit cell (**Table 2**). For the overall **8**$^{3+}$ charged unit cell the calculations show that graphene donates substantial electron density, approximately corresponding to half an electron, into the LUMO of the tricationic molecule. The LUMO orbital of the trication is mainly localized on the central benzene ring and it is bonding between this ring and (two of the three) the peripheral benzimidazolium moieties. From a stabilizing point of view the effect of this partial electron transfer is twofold: First, the increased electron density at the central benzene ring decreases the coulombic repulsion between the cationic benzimidazolium moieties via a screening effect.

Table 2. Supercell starting charge and overall electron distribution of molecule **8** (without counterions), when non-covalently attached to graphene.

Supercell starting charge	Graphene final charge (e)	Molecule final charge (e)	Charge transferred from Graphene (e)
8	-1.93	+1.72	~ −1.18
8^{1+}	-0.94	+2.02	~ −1.02
8^{2+}	-0.32	+2.21	~ −0.74
8^{3+}	+0.61	+2.48	~ −0.55

Second, the bonding traits of the LUMO results in a planarization of the overall molecular structure when electron density is fed into the orbital. The later contributes favorably to the bonding interaction by allowing for a shorter bonding distance and an increase in the surface area exposed to graphene by the trication. The more dense deposition of molecules in the physical samples compared to the unit cell explored in the calculations may disturb the system causing some molecules on the graphene surface to possess more **8**$^{2+}$ character and others to be more like **8**$^{3+}$. This could explain why the adsorbed molecules display broad/overlapping nitrogen signals in XPS. Another reason could be that the strong binding in combination with the propeller shaped molecular structure results in two chemically distinctly

different sets of nitrogen: the set of three nitrogen atoms close to the graphene surface and the set of those on the molecular face opposite to the graphene surface. All six nitrogen atoms in the free cation are chemically equivalent and should, as observed for the pristine silicon/silicate substrate, only give one peak in XPS. The single main peak may in fact indicate that the interaction between the trication and the silicon/silicate surface is so weak that it does not significantly disturb the molecular properties.

The same LUMO orbital, responsible for the stabilization effect discussed for the 8^{3+} charged unit cell, is the one accepting a substantial amount of the charge density of the additional electron in the 8^{2+} charged unit cell (it can be pictured as a unit cell assembled from a trication and a monoanionic supercell of graphene, **Figure 9, S38**). The computed electron densities show that the charge of graphene is only slightly negative and that the charge of the molecule is close to 8^{2+}. Further decrease of overall charge of the unit cell in the calculations shows consistently a charge density on the molecule approximately corresponding to a 8^{2+} species. The charge density corresponding to the additional electron instead builds up on graphene (**Table 2**).
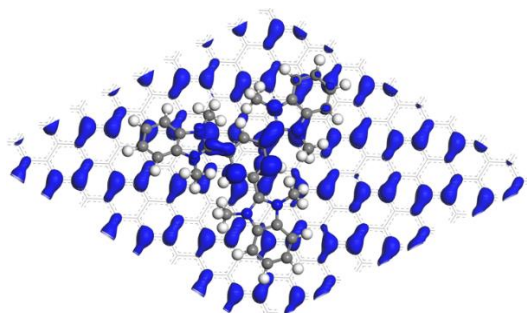
Figure 9. Partial charge density of HOMO for optimized geometry of 8^{3+} charged graphene–trication unit cell. It shows a large charge density localized on the central benzene ring of the **8** trication (without counterions). The charge density localized on the molecule corresponds to the LUMO orbital for the isolated trication.

Charge transfer from graphene to the trication and the formation of a highly delocalized positive charge could rationalize the decrease in the amount of counterions observed in XPS. To better understand the nature of the charge transfer we have, moreover, calculated the electron affinity of tricationic **8** (-4.1 eV) and the ionization potential of graphene (exp 7.20-7.30 eV). The mismatch between the two values justifies the partial transfer of charge (not a full electron) between graphene and trication in case of the 8^{3+} unit cell.

Transport measurements: To better investigate the p-doping effect of **8** on graphene, r-oxo-G was used to fabricate a monolayer field-effect transistor device (FET) (**Figure 10A**). In recent investigations, we evaluated the transport properties of reduced oxo-G with different densities of defects and the effect of the substrate.[19, 33] Here, the FET device was tested before and after non-covalent modification. The electrical transport measurements were performed in a two-probe configuration at ambient conditions. The Si/300 nm SiO$_2$ substrate was used as back gate and source-drain voltage (V_{ds}) was constant at 10 mV. Transfer curves (I_{ds}–V_{ds}) with unipolar character are shown in **Figure 10B**. The hysteresis effect of the monolayer r-oxo-G on SiO$_2$ is observed after sweeping continuously from -50 to 50 V and then back to -50 V. From the dashed lines (on black curve in **Figure 10B**), a hole mobility (μ_h) of 28.6 cm^2 V^{-1}s^{-1} is obtained at ambient conditions, calculated by the equation $\mu = (L/W) \times (1/(C_{ox}V_{ds})) \times (dI_{ds}/dV_{bg})$, where C_{ox} =1.15×10^{-8} F/ cm^{-2}. After doping r-oxo-G with **8** I_{ds}–V_{ds} curves still keep the unipolar character, but these curves lean to a higher p-doped direction. The hole mobility decreased to 20.7 cm^2 V^{-1}s^{-1}. In addition, we found the hysteresis effect increased indicating that more carriers were trapped between r-oxo-G and the SiO$_2$ interfaces. The resistance of monolayer r-oxo-G device (with length 3 μm) before and after doping varies only slightly from 6.0 to 5.8 kΩ with a channel width of 20 μm and length of 3 μm.
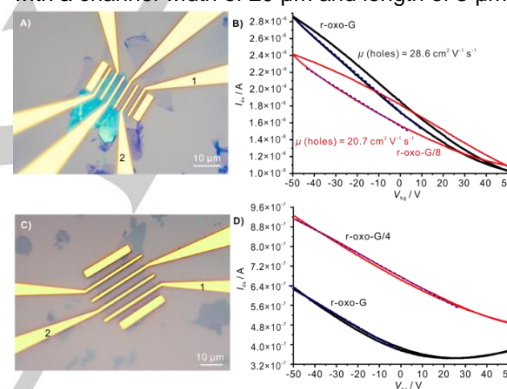
Figure 10. Transport measurements of monolayer r-oxo-G-based FET. A) Optical image of the fabricated graphene device. A channel width of 20 μm and length of 3 μm between electrode 1 and 2. B) Transfer characteristics of the monolayer graphene before and after doping with **8**. Transport measurements of monolayer r-oxo-G-based FET. V_{ds} = 10 mV. C) Optical image of the fabricated r-oxo-G device. A channel width of 10 μm and length of 4.5 μm between electrode 1 and 2. D) Transfer characteristics of the monolayer r-oxo-G before and after doping with **4**. V_{ds} = 10 mV.

We note that the reference experiment using the uncharged compound **4** for non-covalent functionalization of r-oxo-G also results in p-doping of the underlying graphene (**Figure 10C**). Transfer curves (I_{ds}–V_{ds}) in **Figure 10D** show a Dirac point at 20 V, which indicates that r-oxo-G itself possessing p-doping feature. We also observe a negligible hysteresis effects from the measurements with **4**, compared with the measurements from **8**. After doping with **4**, the transfer curves become unipolar, suggesting a stronger p-doping character of r-oxo-G. Hole mobility (μ_h) of the r-oxo-G before and after doping decreases

from 20.4 cm^2 V^{-1}s^{-1} to 18.9 cm^2 V^{-1}s^{-1}. The corresponding resistance of the r-oxo-G before and after doping decreases from 27.2 to 18.9 kΩ at V_{ds}=10 mV, V_{bg}= 0 V with a channel width of 10 μm and length of 4.5 μm. Comparing both FET devices with each other, a stronger decrease in hole mobility can be observed for **8**. This can be explained by a stronger interaction between **8** and r-oxo-G compared with **4** and r-oxo-G, which leads simultaneously to a stronger p-doping effect on the underlying graphene for **8**.

Conclusion

Through a concise synthetic strategy, we synthesized a series of cationic N-hetero-π-systems, which were used to non-covalently functionalize graphene forming graphene/molecular hybrid structures. The cationic molecules form a stable molecular layer and interact strongly with graphene. This results in a reversible one-electron transfer between the molecules and the underlying graphene, which leads to p-doping of the graphene. The functionalization of graphene and the one-electron transfer was studied by AFM, XPS, ToF-SIMS and Raman spectroscopy. The performed measurements did not show any influence of the various counterions. DFT-calculations confirmed the observed effects from the performed experiments. With the reported wet-chemical method of graphene functionalization, we were able to fabricate monolayer graphene FET devices. Comparing both FET devices with each other, a stronger decrease in hole mobility can be observed for the tricationic molecules **8** compared to the neutral precursor **4**. This can be explained by a stronger interaction between **8** and r-oxo-G compared with **4** and r-oxo-G, which leads simultaneously to a stronger p-doping effect on the underlying graphene for trication **8**.

Both, the novel series of compounds as well as the described method help to understand the non-covalent functionalization of graphene in more detail. In the future, based on FET devices novel sensors can be fabricated for selective sensing, if the analyte interacts with the cationic molecules adsorbed to the surface.

Conflict of interest

The authors declare no conflict of interest.

References

[1] a) K. S. Novoselov, A. K. Geim, S. V. Morozov, D. Jiang, Y. Zhang, S. V. Dubonos, I. V. Grigorieva, A. A. Firsov, *Science* **2004**, *306*, 666-669; b) M. J. Allen, V. C. Tung, R. B. Kaner, *Chem. Rev.* **2010**, *110*, 132-145.

[2] D. D. L. Chung, *J. Mater. Sci.* **2002**, *37*, 1475-1489.

[3] K. S. Novoselov, D. Jiang, F. Schedin, T. J. Booth, V. V. Khotkevich, S. V. Morozov, A. K. Geim, *Proc. Natl. Acad. Sci. U.S.A.* **2005**, *102*, 10451-10453.

[4] C. Lee, X. D. Wei, J. W. Kysar, J. Hone, *Science* **2008**, *321*, 385-388.

[5] I. Meric, M. Y. Han, A. F. Young, B. Ozyilmaz, P. Kim, K. L. Shepard, *Nat. Nanotechnol.* **2008**, *3*, 654-659.

[6] D. Neumaier, H. Zirath, *2D Mater.* **2015**, *2*, 030203.

[7] J. Bae, O. S. Kwon, C. S. Lee, *Recent Pat. Nanotech.* **2017**, *11*, 93-100.

[8] Y. H. Xu, J. Q. Liu, *Small* **2016**, *12*, 1400-1419.

[9] a) D. Chen, H. B. Feng, J. H. Li, *Chem. Rev.* **2012**, *112*, 6027-6053; b) Z. G. Zhu, L. Garcia-Gancedo, A. J. Flewitt, H. Q. Xie, F. Moussy, W. I. Milne, *Sensors* **2012**, *12*, 5996-6022; c) F. Schedin, A. K. Geim, S. V. Morozov, E. W. Hill, P. Blake, M. I. Katsnelson, K. S. Novoselov, *Nat. Mater.* **2007**, *6*, 652-655.

[10] a) L. M. Dai, *Abstr. Pap. Am. Chem. Soc.* **2016**, *252*; b) S. H. Hur, J. N. Park, *Asia-Pac. J. Chem. Eng.* **2013**, *8*, 218-233; c) B. Luo, S. M. Liu, L. J. Zhi, *Small* **2012**, *8*, 630-646.

[11] P. J. Zomer, S. P. Dash, N. Tombros, B. J. van Wees, *Appl. Phys. Lett.* **2011**, *99*, 232104.

[12] J. Q. Liu, J. G. Tang, J. J. Gooding, *J. Mater. Chem.* **2012**, *22*, 12435-12452.

[13] M. Gobbi, E. Orgiu, P. Samori, *Adv. Mater.* **2018**, *30*, e1706103.

[14] a) C. R. Dean, L. Wang, P. Maher, C. Forsythe, F. Ghahari, Y. Gao, J. Katoch, M. Ishigami, P. Moon, M. Koshino, T. Taniguchi, K. Watanabe, K. L. Shepard, J. Hone, P. Kim, *Nature* **2013**, *497*, 598-602; b) L. A. Ponomarenko, R. V. Gorbachev, G. L. Yu, D. C. Elias, R. Jalil, A. A. Patel, A. Mishchenko, A. S. Mayorov, C. R. Woods, J. R. Wallbank, M. Mucha-Kruczynski, B. A. Piot, M. Potemski, I. V. Grigorieva, K. S. Novoselov, F. Guinea, V. I. Fal'ko, A. K. Geim, *Nature* **2013**, *497*, 594-597; c) B. Hunt, J. D. Sanchez-Yamagishi, A. F. Young, M. Yankowitz, B. J. LeRoy, K. Watanabe, T. Taniguchi, P. Moon, M. Koshino, P. Jarillo-Herrero, R. C. Ashoori, *Science* **2013**, *340*, 1427-1430.

[15] M. Ashton, J. Paul, S. B. Sinnott, R. G. Hennig, *Phys. Rev. Lett.* **2017**, *118*, 106101.

[16] C. H. Kim, I. Kymissis, *J. Mater. Chem. C* **2017**, *5*, 4598-4613.

[17] a) N. Chandrashekhar, B. Thomas, V. Gayathri, K. V. Ramanathan, N. M. N. Gowda, *Magn. Reson. Chem.* **2008**, *46*, 769-774; b) H. Y. Lee, J. Park, M. S. Lah, J. I. Hong, *Chem. Commun.* **2007**, 5013-5015; c) J. F. Xiong, S. H. Luo, J. P. Huo, J. Y. Liu, S. X. Chen, Z. Y. Wang, *J. Org. Chem.* **2014**, *79*, 8366-8373; d) B. Zhang, Y.

Gao, J. L. Li, Z. Shi, *Chin. Chem. Lett.* **2006**, *17*, 1165-1168.

[18] a) J. H. Zhai, A. Wan, W. B. Wu, *Mod. Phys. Lett. B* **2015**, *29*; b) Y. Zhang, L. Y. Zhang, C. W. Zhou, *Acc. Chem. Res.* **2013**, *46*, 2329-2339.

[19] S. Eigler, M. Enzelberger-Heim, S. Grimm, P. Hofmann, W. Kroener, A. Geworski, C. Dotzer, M. Rockert, J. Xiao, C. Papp, O. Lytken, H. P. Steinrück, P. Müller, A. Hirsch, *Adv. Mater.* **2013**, *25*, 3583-3587.

[20] S. Eigler, F. Hof, M. Enzelberger-Heim, S. Grimm, P. Müller, A. Hirsch, *J. Phys. Chem. C* **2014**, *118*, 7698-7704.

[21] M. S. Dresselhaus, A. Jorio, R. Saito, *Annu. Rev. Condens. Matter Phys., Vol 1* **2010**, *1*, 89-108.

[22] G. Socrates, *Infrared and Raman Characteristic Group Frequencies: Tables and Charts*, **2004**, Wiley, ISBN: 978-0-470-09307-8.

[23] A. C. Ferrari, *Solid State Commun.* **2007**, *143*, 47-57.

[24] A. Das, S. Pisana, B. Chakraborty, S. Piscanec, S. K. Saha, U. V. Waghmare, K. S. Novoselov, H. R. Krishnamurthy, A. K. Geim, A. C. Ferrari, A. K. Sood, *Nat. Nanotechnol.* **2008**, *3*, 210-215.

[25] K. Uchinokura, T. Sekine, E. Matsuura, *Solid State Commun.* **1972**, *11*, 47-49.

[26] M. P. Seah, *Vacuum* **1984**, *34*, 463-478.

[27] C. K. Chua, M. Pumera, *Chem.-Eur. J.* **2013**, *19*, 2005-2011.

[28] T. I. T. Okpalugo, P. Papakonstantinou, H. Murphy, J. McLaughlin, N. M. D. Brown, *Carbon* **2005**, *43*, 153-161.

[29] W. F. S. J. F. Moulder, P. E. Sobol and K. D. Bomben, *Perkin-Elmer Corp., Norwalk* **1995**.

[30] D. Q. Yang, E. Sacher, *Surf. Sci.* **2003**, *531*, 185-198.

[31] C. Tengstedt, M. Unge, M. P. de Jong, S. Stafstrom, W. R. Salaneck, M. Fahlman, *Phys. Rev. B* **2004**, *69*, 165208.

[32] a) C. Bellitto, M. Bonamico, V. Fares, P. Imperatori, S. Patrizio, *J. Chem. Soc., Dalton Trans.* **1989**, 719-727; b) L. Valade, J. Fraxedas, D. de Caro, J. P. Savy, I. Malfant, C. Faulmann, M. Almeida, *J. Low Temp. Phys.* **2006**, *142*, 141-146.

[33] a) Z. Wang, Q. Yao, S. Eigler, *Chem.-Eur. J.* **2020**, DOI: 10.1002/chem.201905252; b) Z. P. Wang, Q. R. Yao, Y. L. Hu, C. Li, M. Hussmann, B. Weintrub, J. N. Kirchhof, K. Bolotin, T. Taniguchi, K. Watanabe, S. Eigler, *RSC Adv.* **2019**, *9*, 38011-38016.

Evidence for Electron Transfer between Graphene and Non-covalently Bound π-Systems

Steffen M. Brülls,[a] Valentina Cantatore,[a] Zhenping Wang,[b] Pui Lam Tam,[c] Per Malmberg,[a] Jessica Stubbe,[d] Biprajit Sarkar,[d],[e] Itai Panas,[a] Jerker Mårtensson,[a] and Siegfried Eigler*[b]

Abstract: Hybridizing graphene and molecules possess a high potential for developing new applications. However, new methods to characterize such hybrids must be developed. Herein, we present the wet-chemical non-covalent functionalization of graphene with cationic π-systems and characterize the interaction between graphene and the molecules in detail. A series of tricationic benzimidazolium salts with various steric demand and counterions was synthesized, characterized and used for the fabrication of graphene hybrids. Subsequently, the doping effects were studied. The molecules are adsorbed onto graphene and studied by Raman spectroscopy, XPS as well as ToF-SIMS. The charged π-systems show a p-doping effect on the underlying graphene. Consequently, the tricationic molecules are reduced *via* an one electron transfer process from graphene, a process which is accompanied by the loss of counterions. DFT calculations support this process and the strong p-doping could be confirmed in fabricated monolayer graphene/hybride FET devices. The results are the basis to develop sensor applications, which are based on analyte/molecule interactions and effects on doping.

[a] M. Sc. Steffen Marc Brülls, Dr. Valentina Cantatore, Dr. Per Malmberg, Prof. Dr. Itai Panas, Prof. Dr. Jerker Mårtensson
Department of Chemistry and Chemical Engineering
Chalmers University of Technology
Kemivägen 10, 41296 Gothenburg (Sweden)

[b] Prof. Dr. Siegfried Eigler, M. Sc. Zhenping Wang
Institut für Chemie und Biochemie
Freie Universität Berlin
Takustraße 3, 14195 Berlin (Germany)
E-mail: siegfried.eigler@fu-berlin.de

[c] Dr. Pui Lam Tam
Department of Industrial and Materials Science
Chalmers University of Technology
Rännvägen 2A, 41296 Gothenburg (Sweden)

[d] M. Sc. Jessica Stubbe, Prof. Dr. Biprajit Sarkar
Institut für Chemie und Biochemie
Freie Universität Berlin
Fabeckstraße 34/36, 14195 Berlin (Germany)

[e] Prof. Dr. Biprajit Sarkar
Institut für Anorganische Chemie
Universität Stuttgart
Pfaffenwaldring 55, D-70569 Stuttgart (Germany)

Supporting information for this article is given via a link at the end of the document

Table of Contents

Experimental Procedures

All starting materials were purchased as reagent grade from *Sigma- Aldrich*. The reagents were used as received. Dry acetonitrile was purchased from *Acros* and stored under N_2-atmosphere. Octyltriflate[1] and *1,3,5-tris(benzimidazolyl)benzene* **3**[2] *and* **4**[2] were prepared according to literature procedures. Thin layer chromatography (TLC) was performed on plates from *Merck* (silica gel 60, F254). Substances were visualized under UV light (wavelength λ = 254 nm). Solvents and R_f values are stated in the experimental part. Column chromatography was performed on silica gel from *Merck* (35-70 micron). Some purifications were performed *via* automated column chromatography on a Biotage IsoleraTM Spektra One flash chromatography system usingBiotage SNAP-50 g KP-sil columns. The CVD graphene was purchased from *Graphenea*. Its quality was checked by analysis of the G and 2D peaks *via* Raman spectroscopy. Air-sensitive reactions were carried out in flame-dried glassware and under an inert N_2-atmosphere using Schlenk techniques. Melting points were determined on a Büchi B-545 melting-point apparatus in open capillaries and are reported uncorrected. "Decomp" refers to decomposition.

2D material sample preparation

The sample preparation of non-covalent functionalized graphene for HR-MS, Raman spectroscopy, XPS, AFM and electrical transport measurements was always the same. A silicon wafer *with deposited graphene, either CVD graphene or r-oxo-G was incubated in a 12 mM methanol solution of the respective tricationic molecule for 2 hours at 4 °C. After incubation, the functionalized graphene wafer was removed from the incubation solution and rinsed with methanol to remove excess of the tricationic molecules.* XPS samples and Raman spectroscopy samples of neat molecules/adsorbates without graphene were prepared by drop-casting 3 drops of a *12 mM methanol solution of the respective tricationic molecule onto a* silicon wafer and allow the solvent to evaporate.

Nuclear magnetic resonance spectroscopy

^{1}H NMR, ^{13}C NMR and ^{19}F spectra were recorded on a Agilent 400 spectrometer (400.1 MHz for ^{1}H, 100.6 MHz for ^{13}C and 376.3 MHz for ^{19}F). Chemical shifts (δ) are reported in ppm and were referenced to the residual solvent signal as an internal reference (DMSO-d_6: 2.50 ppm for ^{1}H, 39.52 for ^{13}C; ACN-d_3: 1.94 ppm for ^{1}H, 1.32, 118.26 for ^{13}C; CD_2Cl_2: 5.32 ppm for ^{1}H, 53.84 for ^{13}C). Coupling constants (*J*) are given in Hertz (Hz) and the apparent resonance multiplicity is reported as singlet (s), doublet (d), triplet (t), quartet (q) or multiplet (m).

High resolution mass spectroscopy

High resolution mass spectroscopy data was obtained on an Agilent 6520 QTOF LC/MS coupled with an Agilent 1290 Infinity LC system. The signal of the molecular ion [M]$^+$ is reported in m/z units. The submitted samples (1 mg) were diluted to ca. 10 µg/ml in acetonitrile. The sample was analyzed using an Agilent 1290 infinity LC system equipped with autosampler tandem. HRMS spectra were recorded with a 0.3 ml/min flow rate using an isocratic method (50% MPA/50% MPB). Mobile Phase A (MPA): Water with 0.04% formic acid. Mobile Phase B (MPB): MeOH with 0.04% Formic acid. All samples were initially analyzed using an ESI source in positive mode (scan range 100-1200 m/z). Samples were also analyzed in negative mode to detect anionic molecules and fragments (scan range 50-1200 m/z).

Raman spectroscopy

Raman spectroscopy data was obtained on a WITec alpha300 R instrument using an excitation wavelength of 532 nm. The laser intensity was kept at 12 mW for all performed measurements unless stated otherwise. The integration time was between 0.1 s and 1.0 s. single spectra were four times accumulated. For most measurements a grating of 600 g/mm was chosen and the spectral center was set to 1900 cm^{-1}. For a grating of 1800 g/mm, the spectral center was set to 1350 cm^{-1}. The sample was placed on a motorized x,y table and focused before each measurement. For larger areas it was ensured that the focus of the excitation laser was constant. The data analysis was performed with the Project Manager software from WITec and visualized with OriginPro 9. The G and the 2D peaks were fitted by one Lorentzian function each. The graphene samples were analyzed via Raman spectroscopy before and after non-covalent modification.

X-ray photoelectron spectroscopy

X-ray photoelectron spectroscopy (XPS) experiment was conducted in a PHI5000 VersaProbe III Scanning XPS Microprobe system. The X-ray source was a monochromated Al anode (E = 1486.6 eV) with the beam diameter 100 μm (Energy resolution: 0.646 eV). Dual charge compensation was conducted by using argon ion gun (+ve) and electron neutralizer (-ve) for non-conductive materials. The survey scan was performed in the range between 0 and 1250 eV (step size: 1.0 eV) for compositional analysis. The high resolution narrow scan for the selected regions was performed with the step size of 0.1 eV for chemical state analysis. The energy scale calibration (ISO 15472) was performed by aligning the core level peaks of $Au4f_{7/2}$, $Ag3d_{5/2}$ and $Cu2p_{3/2}$ at 83.96 eV, 368.21 eV and 932.62 eV, respectively. The sample was adhered on the platen with double-sided tape, and the surface contaminant was removed by blowing with dry N_2 gas. The analyzing chamber was kept under UHV condition with pressure lower than 3.0×10^{-6} Pa. The data analysis was performed with MultiPak software (Ver. 9.7.0.1). To ease data analysis, three energy states, including C1s at 284.6 eV[3] for the sp^2-hybridised carbon in graphene (i.e. C=C bond), Si2p at 103.6 – 104.0 eV and O1s at 532.6 – 533.0 eV for the native SiO_2 layer on silicon wafer, are used accordingly as the reference positions in this study. The used CVD graphene just showed the elemental signals for carbon, oxygen and silicon (from the wafer) in the measurements (see **Figure S27**).

Imaging time-of-Flight Secondary Ion Mass Spectrometry

ToF-SIMS data were obtained with a TOF.SIMS 5 instrument (ION-TOF GmbH, Münster, Germany). The instrument is equipped with a 25 keV Bi_3^+ cluster ion gun as the primary ion source and a 10 keV C_{60}^+ ion source for sputtering and etching. The samples were analyzed using a pulsed primary ion beam (Bi_3^{++}, 0.14 pA at 50 keV) at a field of view of 150 μm × 150 μm. All spectra were acquired and processed with the Surface Lab software (version 6.4, ION-TOF GmbH). Low-energy electrons were used for charge compensation during analysis.

Oxo-Graphene and electrical measurements

The electrical transport measurements were performed in a two-probe configuration at ambient conditions. Oxo-Graphene flakes were deposited onto the Si/SiO_2 (300 nm) substrate by Langmuir–Blodgett technique (LB, Kibron μtrough). Reduction was performed by vapor of hydriodic acid and trifluoroacetic acid (1/1 mixture by volume) at 80 °C. Reduced oxo- Graphene was cleaned with doubly distilled water (Carl Roth). Patterning of the electrode structure was achieved by standard electron beam lithography processing (Raith PIONEER TWO). The 5/70 nm Cr/Au electrodes were deposited by thermal evaporation (Kurt J. Lesker NANO 36). All electrical measurements were carried out at ambient conditions using a two-probe station with micromanipulated probes and two source-measurement units (Keithley 2450).

Atomic Force microscopy

AFM characterization was performed using a JPK Nanowizzard 4 atomic force microscope in tapping mode at room temperature.

Density functional theory calculations

For all the results presented in this work, a 9 × 9 graphene supercell (162 atoms) with the molecule M adsorbed on top was employed. All the results were obtained using the CASTEP program package within the Material Studio 2017 framework in conjunction with the PBE functional including the semi-empirical dispersion-corrected DFT approach (DFT-D2 [19]) of Grimme. Core electrons were described by on-the-fly ultrasoft pseudopotentials and 517 eV cut-off energy. Atomic positions were optimized with the BFGS algorithm using delocalized internal coordinates. The evaluation of the partial atomic charges on the graphene and on the molecule was made based on Mulliken population analysis provided by the DFT calculations.

CV/UV-Vis-NIR spectroelectrochemistry:

Cyclic voltammetry was carried out in 0.1 M Bu_4NPF_6 solution using a three-electrode configuration (glassy carbon working electrode, Pt counter electrode, Ag wire as pseudoreference) and PAR VersaSTAT 4 potentiostat. The ferrocene/ferrocenium (Fc/Fc+) couple served as internal reference. Spectroelectrochemical measurements were carried out in an optically transparent thin-layer electrochemical (OTTLE)[4] cell (CaF_2 windows) with a platinum-mesh working electrode, a platinum-mesh counter electrode, and a silver-foil pseudoreference electrode. Anhydrous and degassed ACN with 0.1 M NBu_4PF_6 as electrolyte was used as the solvent.

Synthetic procedures

2,2',2''-((benzene-1,3,5-triyl)tris(1,3-dimethyl-1*H*-benzo[*d*]imidazol-3-ium)triflate (8)
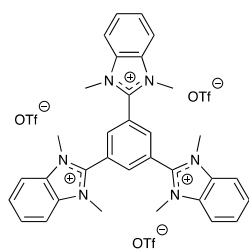
Method A: 1,3,5-tris(1-methyl-1*H*-benzo[*d*]imidazol-2-yl)benzene[1] (100 mg, 0.21 mmol, 1.0 equiv.) was suspended in 10 ml dry acetonitrile under a dry nitrogen atmosphere. Methyl trifluoromethansulfonate (114 mg, 0.70 mmol, 3.3 equiv.) was added and the reaction mixture was stirred at room temperature for 24 h. Acetonitrile was removed under reduced pressure. The product was precipitated from methanol/diethyl ether to give 175 mg of product in 87% yield as white solid. Method B: 1,3,5-tris(1*H*-benzo[*d*]imidazol-2-yl)benzene[1] (50.0 mg, 0.12 mmol, 1.0 equiv.) and potassium carbonate (50.0 mg, 0.36 mmol, 3 equiv.) were suspended in 10 ml dry acetonitrile and stirred at room temperature for 30 minutes under a dry nitrogen atmosphere. Methyl trifluoromethansulfonate (0.16 ml, 1.40 mmol, 12.0 equiv.) was added by a syringe and the reaction mixture stirred for 90 minutes at 50 °C. After allowed to cool down to room temperature acetonitrile was removed under reduced pressure. The crude product was redissolved in methanol and precipitated by slow addition of diethyl ether to give 120 mg of product in 60% yield as a white solid.

¹H NMR (400 MHz, acetonitrile-d₃) δ 4.07 (s, 18H, N-C*H₃*), 7.81–7.88 (m, 6H, Ar*H*), 7.98–8.05 (m, 6H, Ar*H*), 8.58 (s, 3H, Ar*H*);

¹³C NMR (101 MHz, acetonitrile-d₃) δ 34.02, 114.25, 118.32, 125.22, 128.52, 133.26, 138.59, 148.12;

¹⁹F NMR (101 MHz, acetonitrile-d₃) δ -79.41.

HRMS (ESI); Exact mass calculated for cation ($C_{33}H_{33}N_6$)³⁺ [M+3]: 171.0917, Observed Mass: 171.0924.

HRMS (ESI); Exact mass calculated for anion ($C_2H_3F_3O_3S$)⁻ [M-]: 148.9520, Observed Mass: 148.9524.

mp: 290 °C.

2,2',2''-(benzene-1,3,5-triyl)tris(3-ethyl-1-methyl-1*H*-benzo[*d*]imidazol-3-ium)triflate(11)
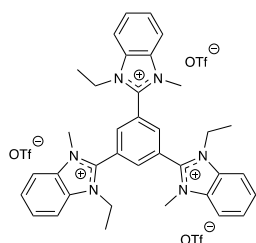
1,3,5-tris(1-methyl-1*H*-benzo[*d*]imidazol-2-yl)benzene[1] (100 mg, 0.21 mmol, 1.0equiv.)) was suspended in 10 ml dry acetonitrile under a dry nitrogen atmosphere. Ethyl trifluoromethansulfonate (125 mg, 0.70 mmol, 3.3 equiv.) was added by a syringe and the reaction mixture was stirred at room temperature for 24 h. Acetonitrile removed under reduced pressure. The crude product was redissolved in methanol and precipitated by slow addition of diethyl ether to give 129 mg of product in 59% yield as a white solid.

¹H NMR (400 MHz, acetonitrile-d₃) δ 1.55 (t, 9H, *J* = 7.3 Hz, 9H, C*H₃*) 4.02 (s, 9H, N-C*H₃*), 4.52 (q, 6H, *J* = 7.3 Hz, 6H, N-C*H₂*-CH₃), 7.83–7.88 (m, 6H, Ar*H*), 7.98–8.11 (m, 6H, Ar*H*), 8.50 (s, 3H, Ar*H*);

¹³C NMR (101 MHz, acetonitrile-d₃) δ 14.21, 33.03, 42.31, 113.59, 117.32, 124.75, 127.72, 131.08, 132.59, 137.08, 146.51;

¹⁹F NMR (101 MHz, acetonitrile-d₃) δ -79.59.

HRMS (ESI); Exact mass calculated for cation ($C_{36}H_{39}N_6$)³⁺ [M+3]: 185.1073, Observed Mass: 185.1078.

HRMS (ESI); Exact mass calculated for anion ($C_2H_3F_3O_3S$)⁻ [M-]: 148.9520, Observed Mass: 148.9525.

mp: 237 °C.

2,2',2''-(benzene-1,3,5-triyl)tris(1-methyl-3-octyl-1*H*-benzo[*d*]imidazol-3-ium)triflate(13)
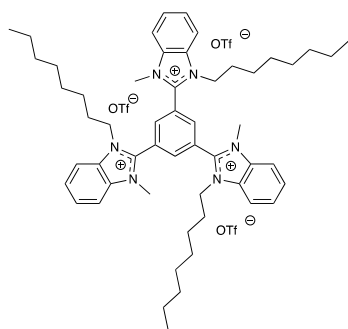
1,3,5-tris(1-methyl-1*H*-benzo[*d*]imidazol-2-yl)benzene[1] (50.0 mg, 0.10 mmol, 1.0 equiv.) was suspended in 10 ml dry acetonitrile under a dry nitrogen atmosphere. Octyltrifluoromethan sulfonate[2] (91.0 mg, 0.33 mmol, 3.3 equiv.) was added by a syringe and the reaction mixture was stirred at room temperature for 24 h. Acetonitrile was removed under reduced pressure. The crude product was redissolved in methanol and precipitated by slow addition of diethyl ether to give 38 mg of product in 30% yield as a white solid.

^{1}H NMR (400 MHz, acetonitrile-d$_3$) δ 0.88 (t, *J* = 7.0 Hz, 9H, C*H*$_3$), 1.19–1.39 (m, 36H, (C*H*$_2$)$_6$), 3.99 (s, 9H, N-C*H*$_3$), 4.41 (t, *J* = 7.7 Hz, 6H, N-C*H*$_2$), 7.82–7.89 (m, 6H, Ar*H*), 7.98–8.08 (m, 6H, Ar*H*), 8.49 (s, 3H, Ar*H*);

^{13}C NMR (101 MHz, acetonitrile-d$_3$) δ 13.37, 22.35, 26,42, 28.94, 29.25, 31.52, 33.12, 46.93, 113.75, 117.01, 124.83, 127.88, 131.39, 132.44, 137.17, 146.29;

^{19}F NMR (101 MHz, acetonitrile-d$_3$) δ -79.39.

HRMS (ESI); Exact mass calculated for cation (C$_{54}$H$_{75}$N$_6$)$^{3+}$ [M+3]: 269.2012, Observed Mass: 269.2018.

HRMS (ESI); Exact mass calculated for anion (C$_2$H$_3$F$_3$O$_3$S)$^-$ [M-]: 148.9520, Observed: 148.9526.

2,2',2''-((benzene-1,3,5-triyl)tris(1,3-dimethyl-1*H*-benzo[*d*]imidazol-3-ium) *tetrafluoroborate (9)*
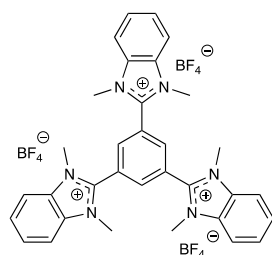
1,3,5-tris(1-methyl-1*H*-benzo[*d*]imidazol-2-yl)benzene[1] (50.0 mg, 0.10 mmol, 1.0 equiv.) was suspended in 10 ml dry acetonitrile under a dry nitrogen atmosphere. Trimethyloxonium tetrafluoroborate (49.0 mg, 0.33 mmol, 3.3 equiv.) was added and the reaction mixture was stirred at room temperature for 24 h. Acetonitrile was removed under reduced pressure. The crude product was redissolved in methanol and precipitated by slow addition of diethyl ether to give 72 mg of product in 88% yield as a white solid.

^{1}H NMR (400 MHz, acetonitrile-d$_3$) δ 4.07 (s, 18H, N-C*H*$_3$), 7.84–7.88 (m, 6H, Ar*H*), 7.99–8.04 (m, 6H, Ar*H*), 8.49 (s, 3H, Ar*H*);

^{13}C NMR (101 MHz, acetonitrile-d$_3$) δ 33.06, 113.39, 117.32, 124.25, 127.74, 132.25, 137.53, 147.11;

^{19}F NMR (101 MHz, acetonitrile-d$_3$) δ -151.78.

HRMS (ESI); Exact mass calculated for cation (C$_{33}$H$_{33}$N$_6$)$^{3+}$ [M+3]: 171.0917, Observed Mass: 171.0924.

HRMS (ESI); Exact mass calculated for anion (BF$_4$)$^-$ [M-]: 87.0035, Observed Mass: 87.0039.

mp: > 350 °C.

2,2',2''-(benzene-1,3,5-triyl)tris(3-ethyl-1-methyl-1*H*-benzo[*d*]imidazol-3-ium) *tetrafluoroborate (12)*
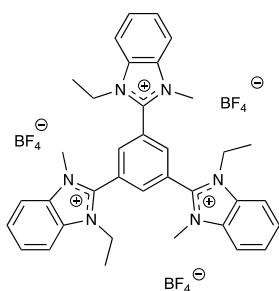
1,3,5-tris(1-methyl-1*H*-benzo[*d*]imidazol-2-yl)benzene[1] (50.0 mg, 0.10 mmol, 1.0 equiv.) was suspended in 10 ml dry acetonitrile under a dry nitrogen atmosphere. Then triethyloxonium tetrafluoroborate (60.0 mg, 0.33 mmol, 3.3 equiv.) was added and the mixture was stirred at room temperature for 24 h. Acetonitrile was removed under reduced pressure. The crude product was redissolved in methanol and precipitated by slow addition of diethyl ether to give 49 mg of product in 58% yield as a white solid.

^{1}H NMR (400 MHz, acetonitrile-d$_3$) δ 1.51 (t, *J* = 7.3 Hz, 9H, CH_3), 3.98 (s, 9H, N-CH_3), 4.48 (q, *J* = 7.2 Hz, 6H, N-CH_2), 7.79–7.84 (m, 6H, Ar*H*), 7.97–8.03 (m, 6H, Ar*H*), 8.44 (s, 3H, Ar*H*);

^{13}C NMR (101 MHz, acetonitrile-d$_3$) δ 15.19, 33.94, 43.25, 114.58, 125.75, 128.76, 132.05, 133.56, 137.98, 147.47;

^{19}F NMR (101 MHz, acetonitrile-d$_3$) δ -151.83.

HRMS (ESI); Exact mass calculated for cation (C$_{35}$H$_{36}$N$_6^{3+}$)$^{3+}$ [M+3]: 185.1073, Observed Mass: 185.1081.

HRMS (ESI); Exact mass calculated for anion (BF$_4$)$^-$ [M-]: 87.0035, Observed Mass: 87.0039.

mp: 200 °C.

2,2',2''-((benzene-1,3,5-triyl)tris(1,3-dimethyl-1*H*-benzo[*d*]imidazol-3-ium) iodide (7)
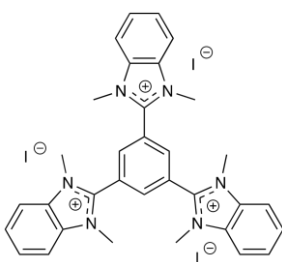
1,3,5-tris(1*H*-benzo[*d*]imidazol-2-yl)benzene[1] (50.0 mg, 0.12 mmol, 1.0 equiv.) and potassium carbonate (50.0 mg, 0.36 mmol, 3.0 equiv.) were suspended in 10 ml dry acetonitrile and stirred at room temperature for 30 minutes under a dry nitrogen atmosphere. Then methyl iodide (0.45 ml, 1.40 mmol, 12.0 equiv.) was added by a syringe and the reaction mixture was stirred for 90 minutes at 50 °C. After cooling down to room temperature acetonitrile was removed under reduced pressure. The crude product was redissolved in methanol and precipitated by slow addition of diethyl ether to give 34 mg of product in 30% yield as a white solid.

^{1}H NMR (400 MHz, DMSO-d$_6$) δ 4.08 (s, 18H, N-CH_3), 7.81–7.86 (m, 6H, Ar*H*), 8.18–8.23 (m, 6H, Ar*H*), 8.83 (s, 3H, Ar*H*). mp: 250 °C (decomp.).

^{13}C NMR (101 MHz, DMSO-d$_6$) δ 33.35, 113.64, 122.98, 127.18, 131.88, 138.01, 147.78;

mp: 250 °C Decomp.

(2-(3,5-bis(3-ethyl-1-methyl-1*H*-3λ^4-benzo[*d*]imidazol-1-ium-2-yl)phenyl)-1-ethyl-1*H*-3λ^4-benzo[*d*]imidazol-1-ium-3-yl)methanide (10)
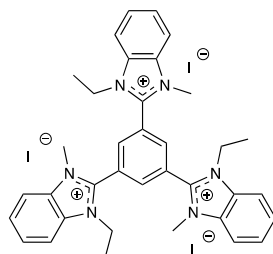
1,3,5-tris(1-methyl-1*H*-benzo[*d*]imidazol-2-yl)benzene[1] (50.0 mg, 0.10 mmol, 1.0 equiv.) was suspended in 10 ml dry acetonitrile under a dry nitrogen atmosphere. Then ethyl iodide (51.5 mg, 0.33 mmol, 3.3 equiv.) was added and the mixture was stirred at room temperature for 24 h. Acetonitrile was removed under reduced pressure. The crude product was redissolved in methanol and precipitated by slow addition of diethyl ether to give 49 mg of product in 58% yield as a white solid.

^{1}H NMR (400 MHz, DMSO-d$_6$) δ 1.44 (t, *J* = 7.3 Hz, 9H, CH_3), 4.04 (s, 9H, N-CH_3), 4.53 (q, *J* = 7.2 Hz, 6H, N-CH_2), 7.83–7.85 (m, 6H, Ar*H*), 8.22–8.27 (m, 6H, Ar*H*), 8.84 (s, 3H, Ar*H*); **^{13}C NMR** (101 MHz, DMSO-d$_6$) δ 14.52, 33.05, 113.77, 3.83, 123.63, 127.10, 127.16, 130.80, 137.31, 147.34, 165.54; **mp**: 250 °C Decomp.

Spectroscopic Characterization of Compounds

Figure S1. *¹H NMR in ACN-d₃ of compound **8***
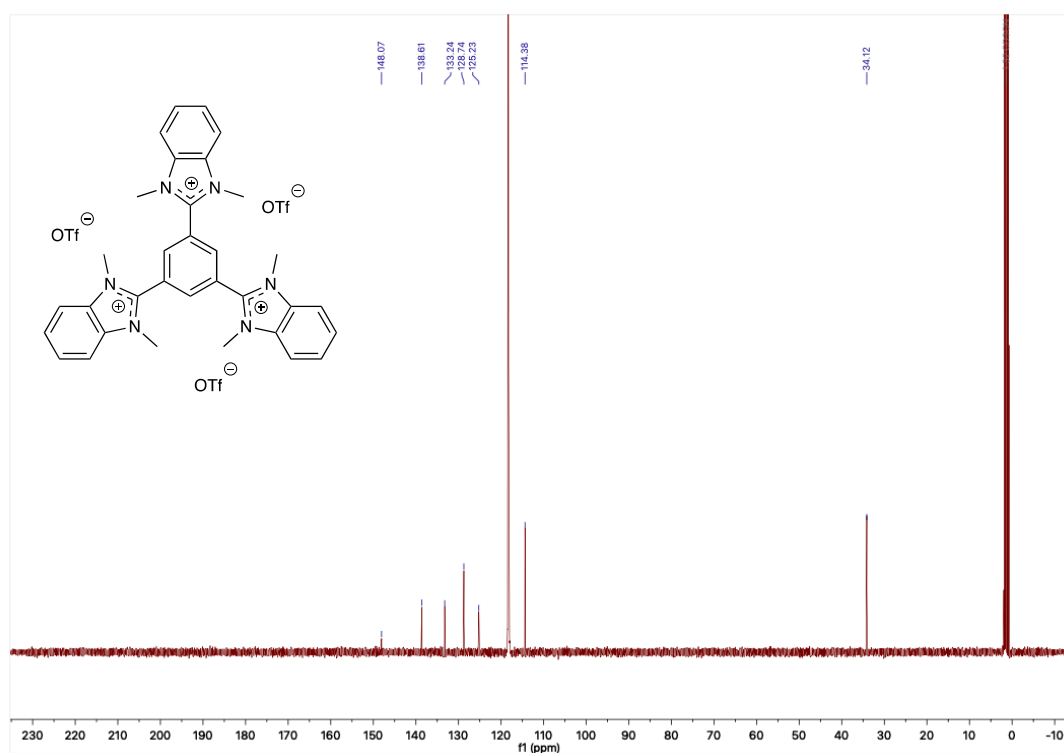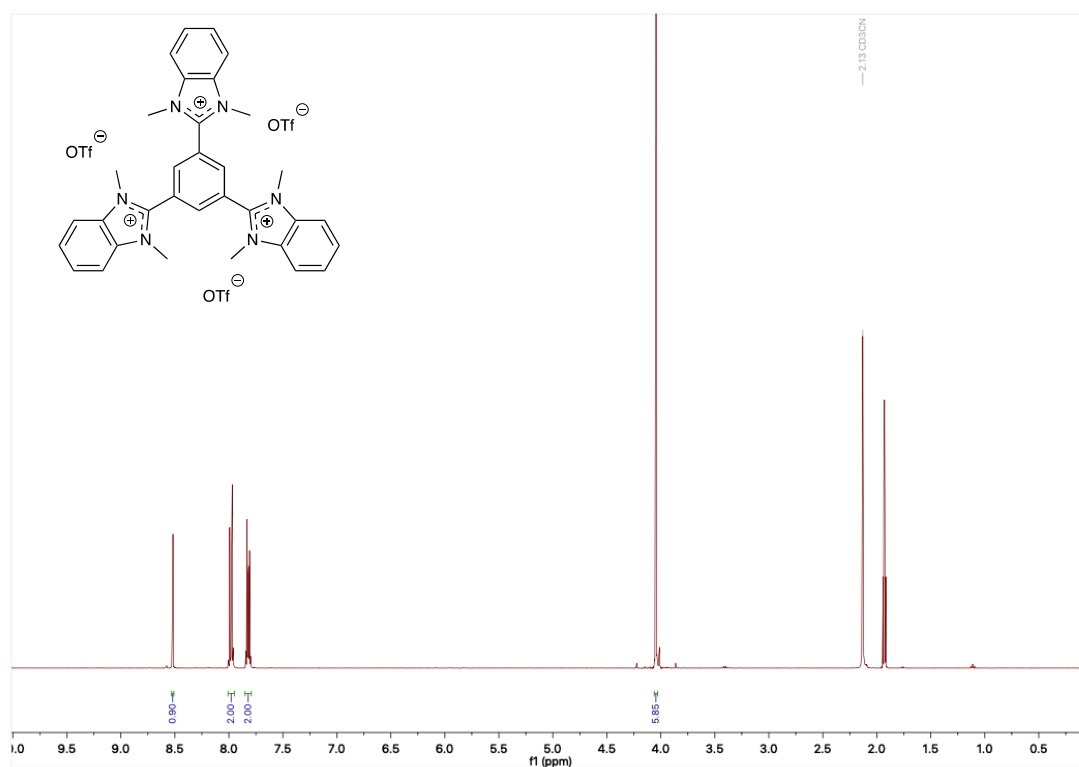
Figure S2. ¹³C NMR in ACN-d₃ of compound 8.
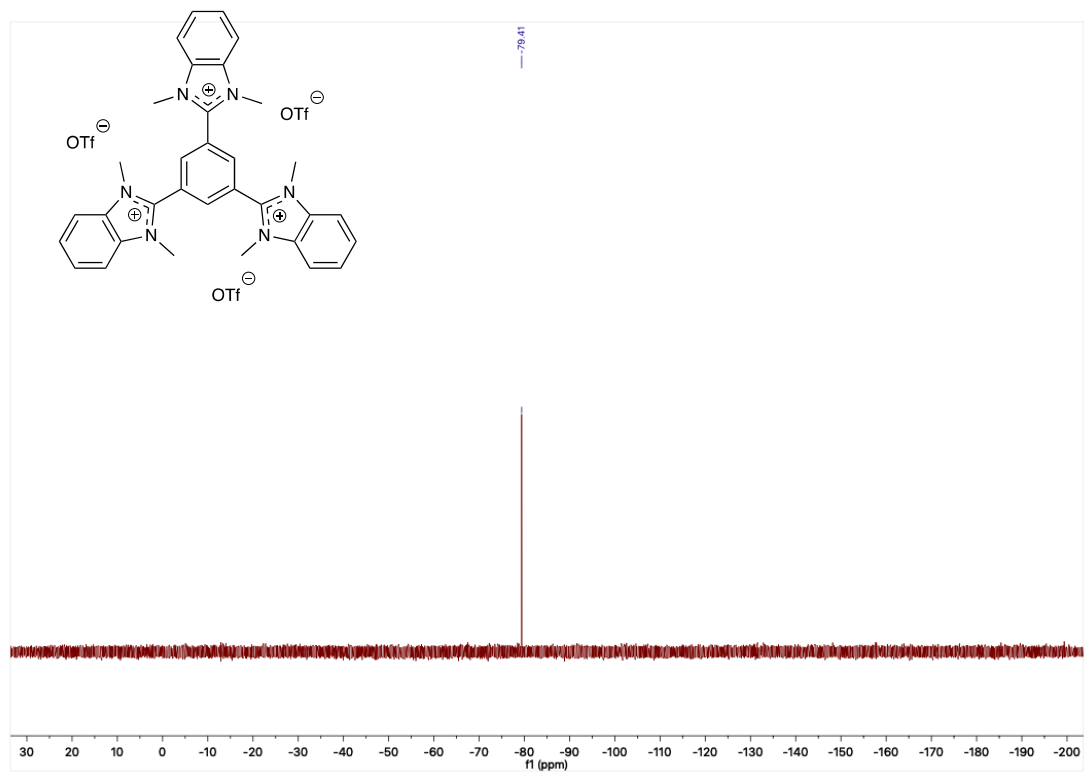
Figure S3. ^{19}F NMR in ACN-d$_3$ of compound 8.
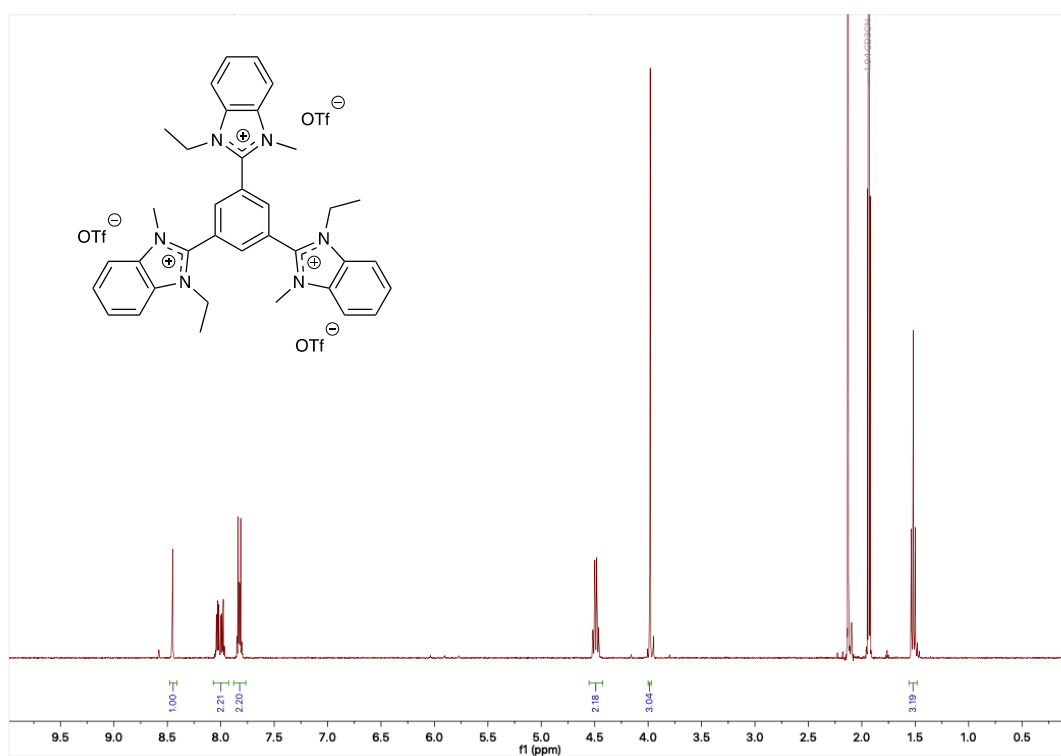
Figure S4. ^{1}H NMR in ACN-d$_3$ of compound 11.
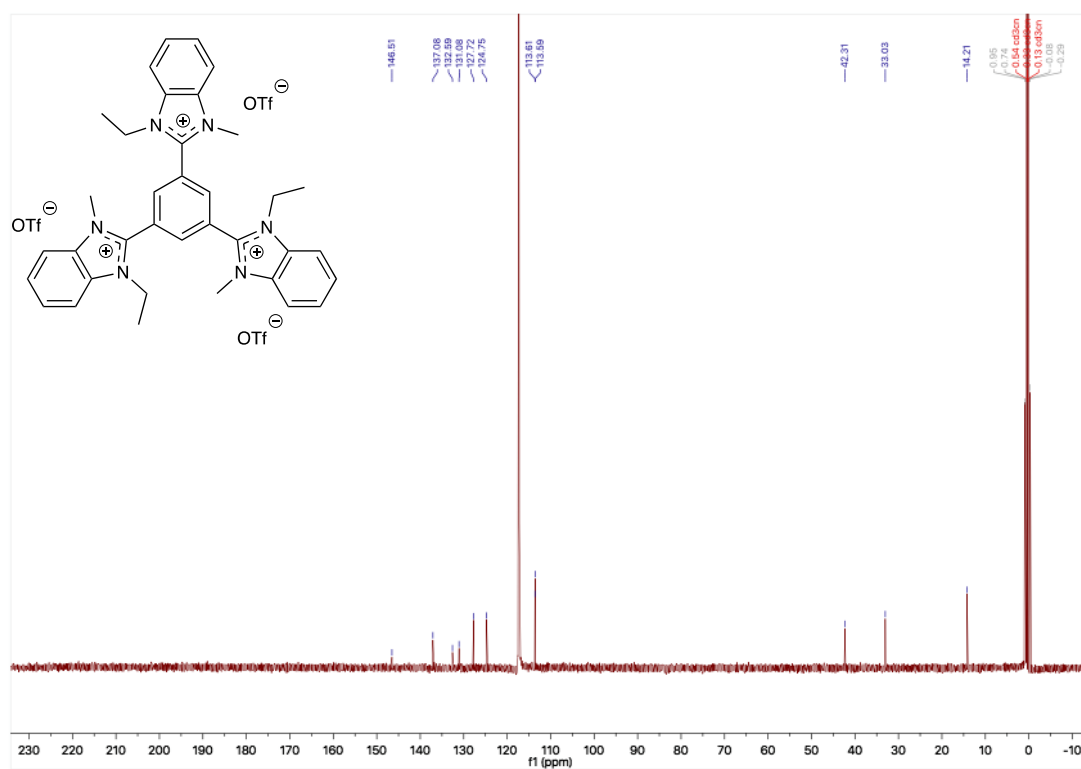
Figure S5. ^{13}C NMR in ACN-d$_3$ of compound 11.
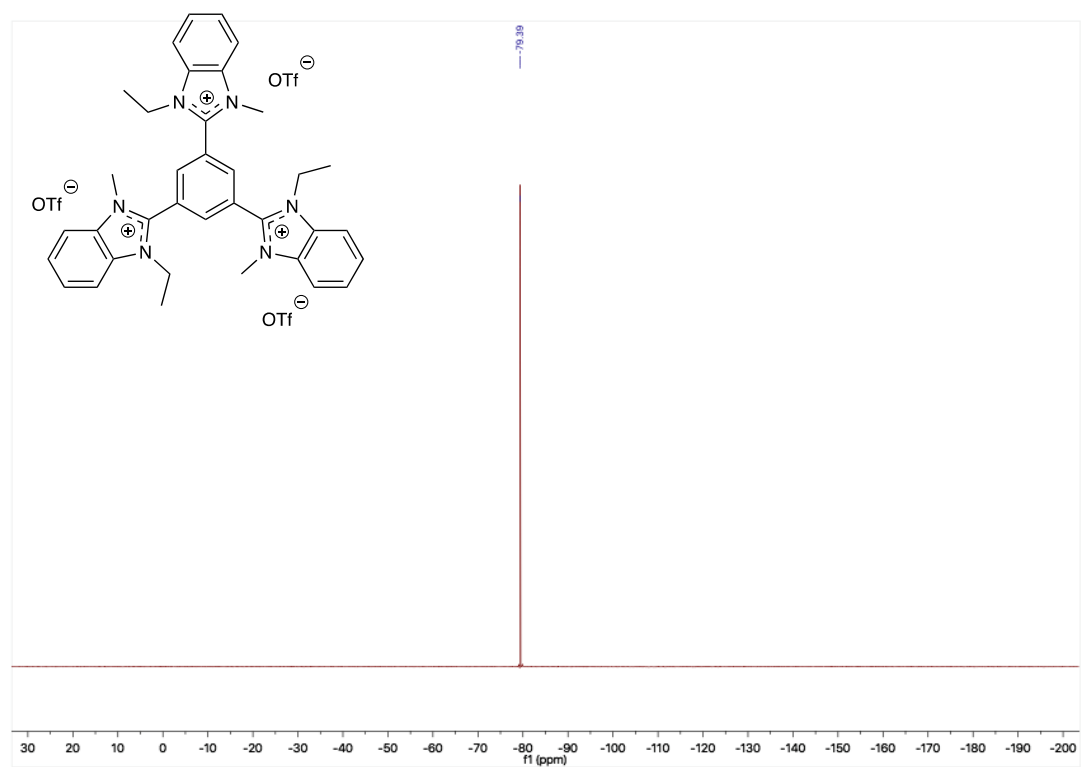
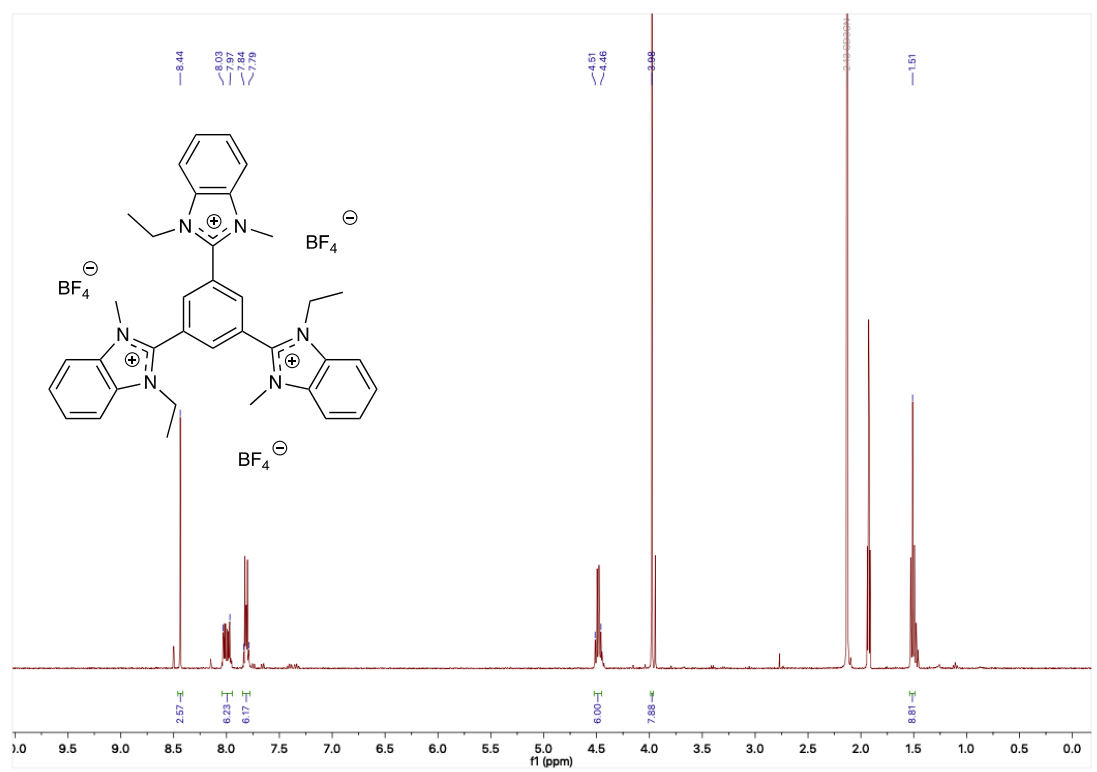Figure S6. ^{19}F NMR in ACN-d$_3$ of compound 11.
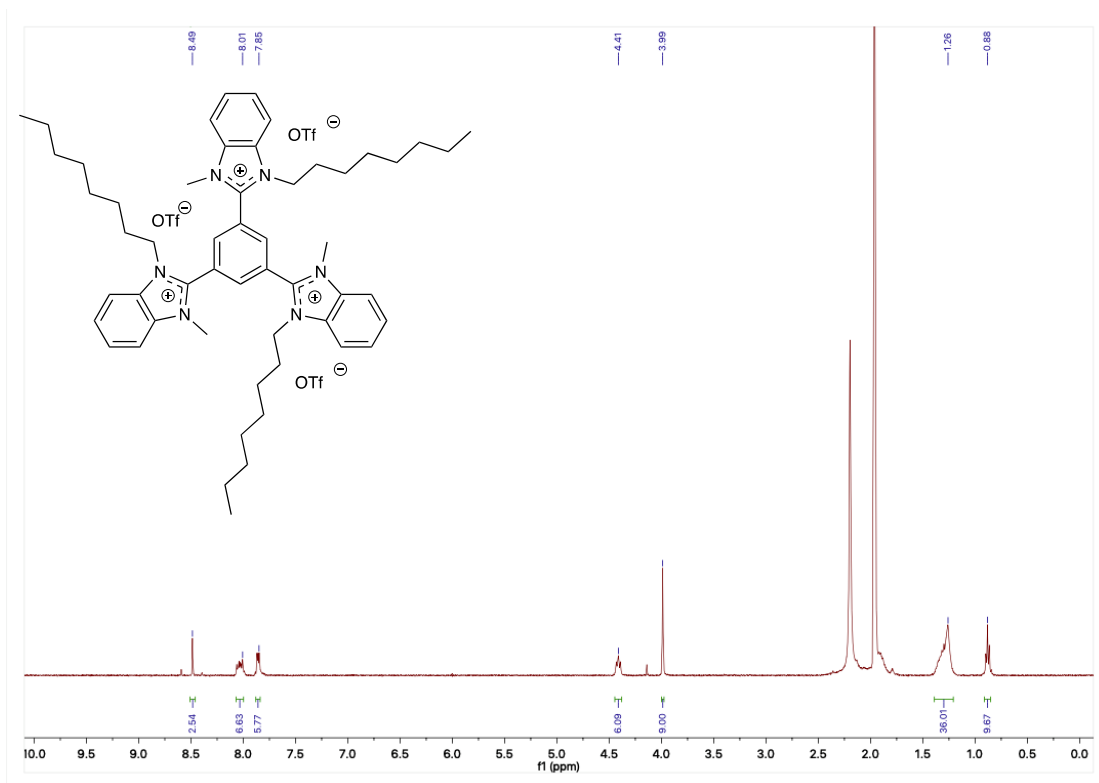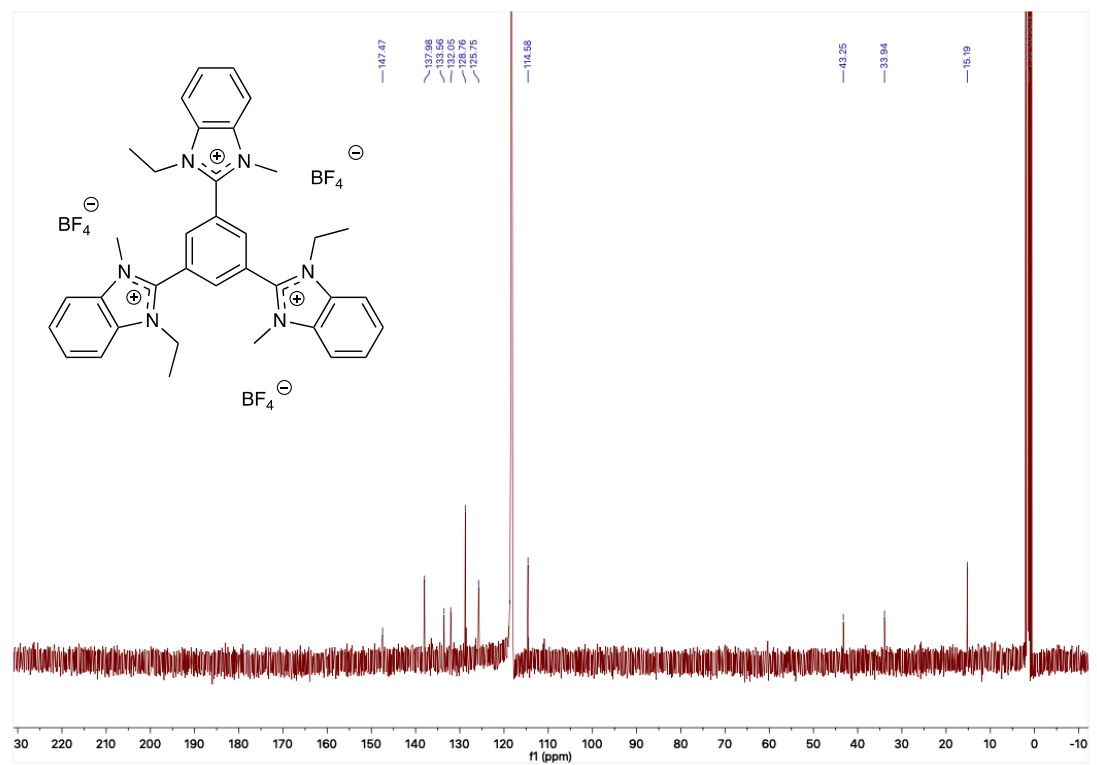
Figure S7. ^{1}H NMR in ACN-d$_3$ of compound 13.
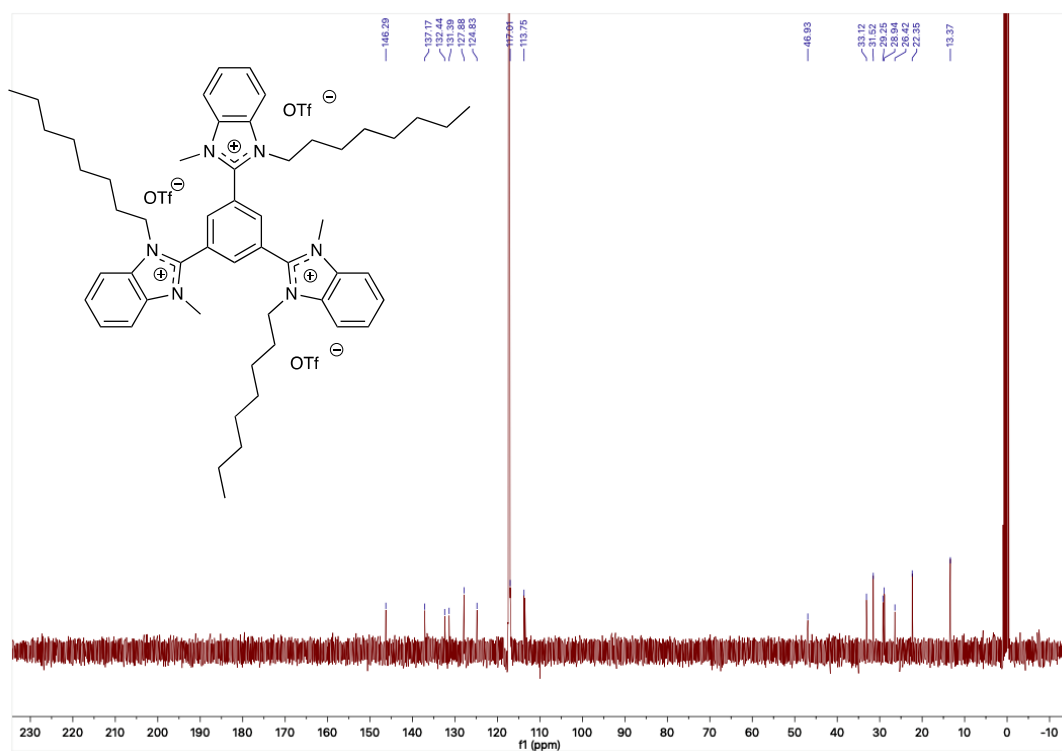
Figure S8. ^{13}C NMR in ACN-d$_3$ of compound 13.

100
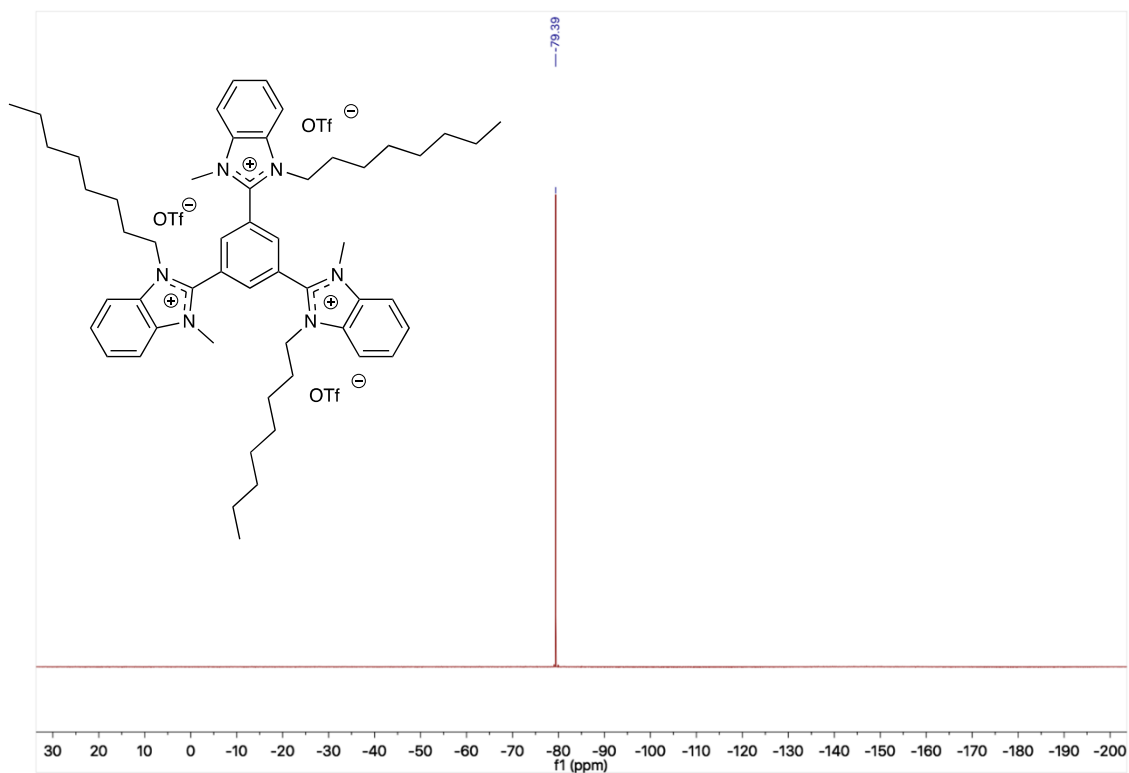
Figure S9. ^{19}F NMR in ACN-d$_3$ of compound 13.
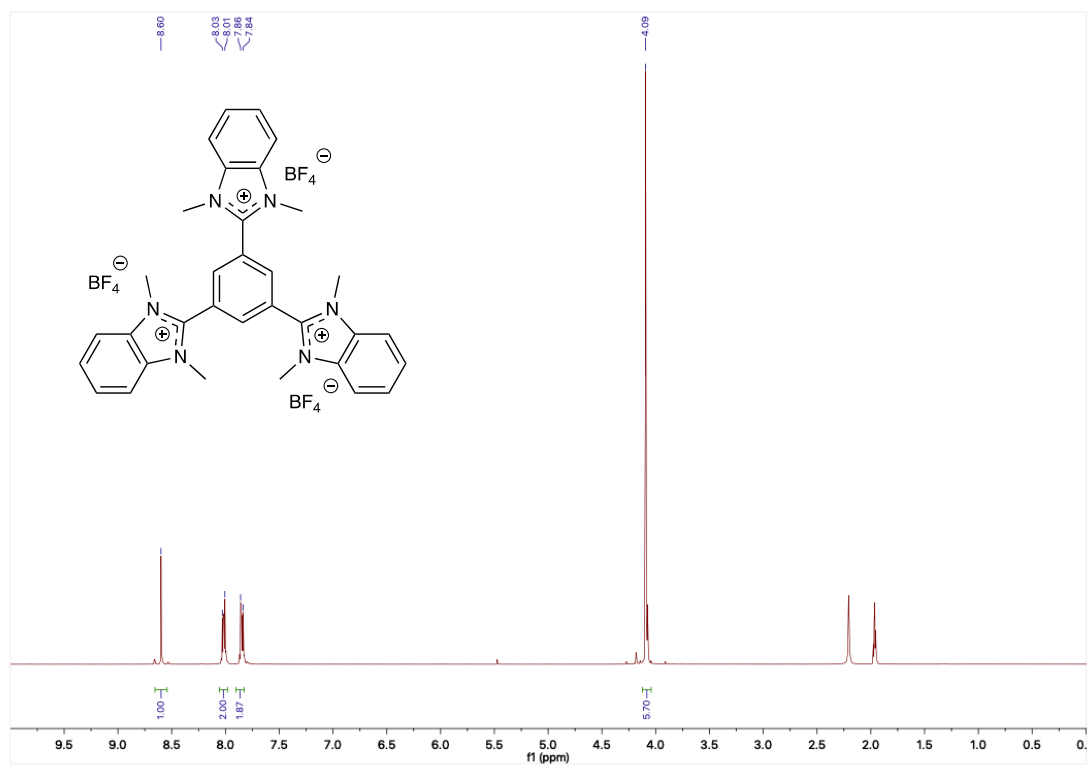
Figure S10. ^{1}H NMR in ACN-d$_3$ of compound **9**.
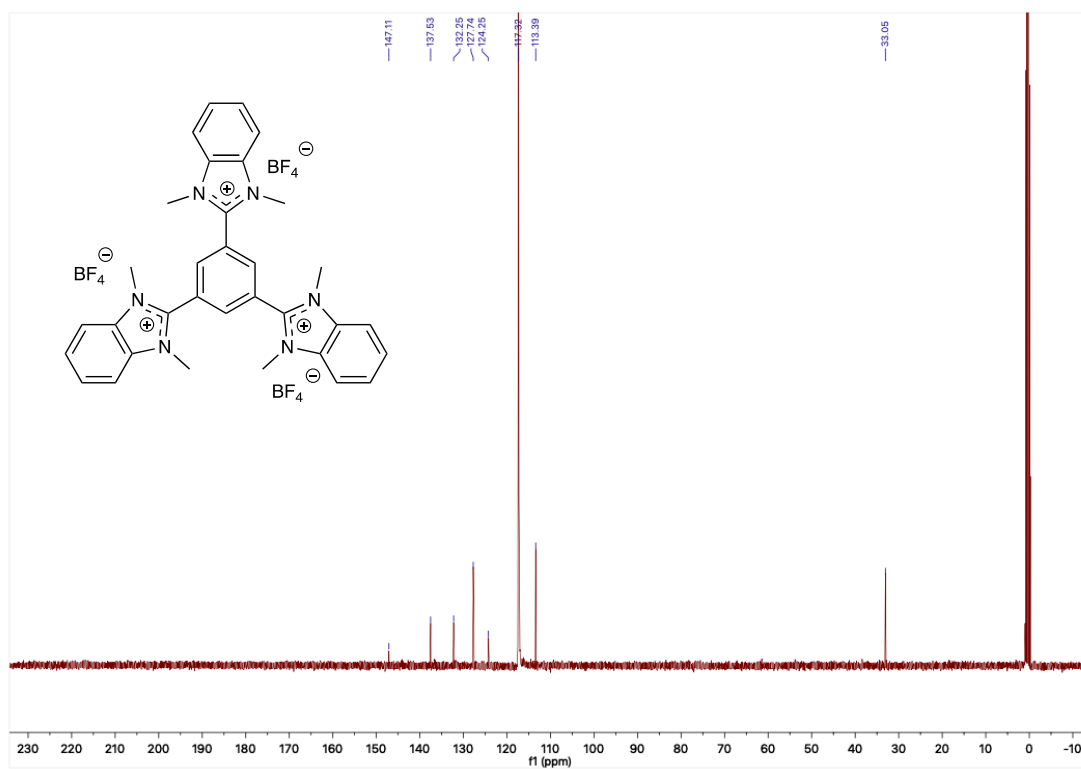
Figure S11. ^{13}C NMR in ACN-d$_3$ of compound 9.
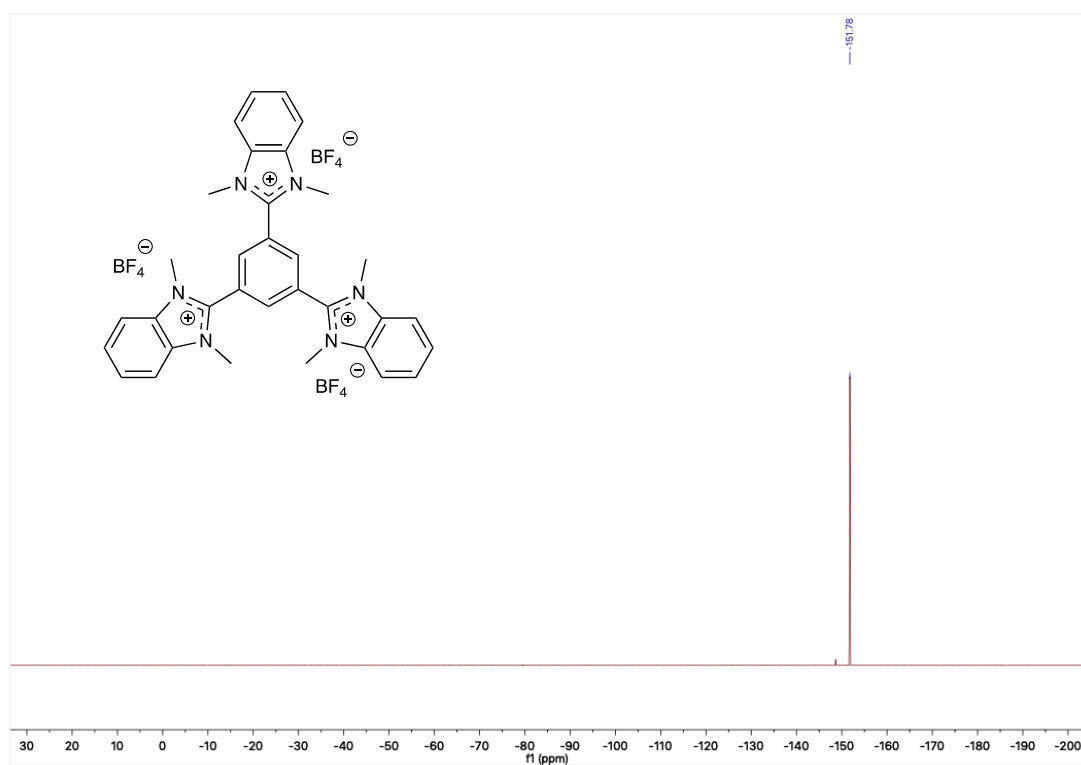
Figure S12. ^{19}F NMR in ACN-d$_3$ of compound 9.

Figure S13. ^{1}H NMR in ACN-d$_3$ of compound **12**.

Figure S14. ^{13}C NMR in ACN-d$_3$ of compound 12.

Figure S15. ^{19}F NMR in ACN-d$_3$ of compound 12.
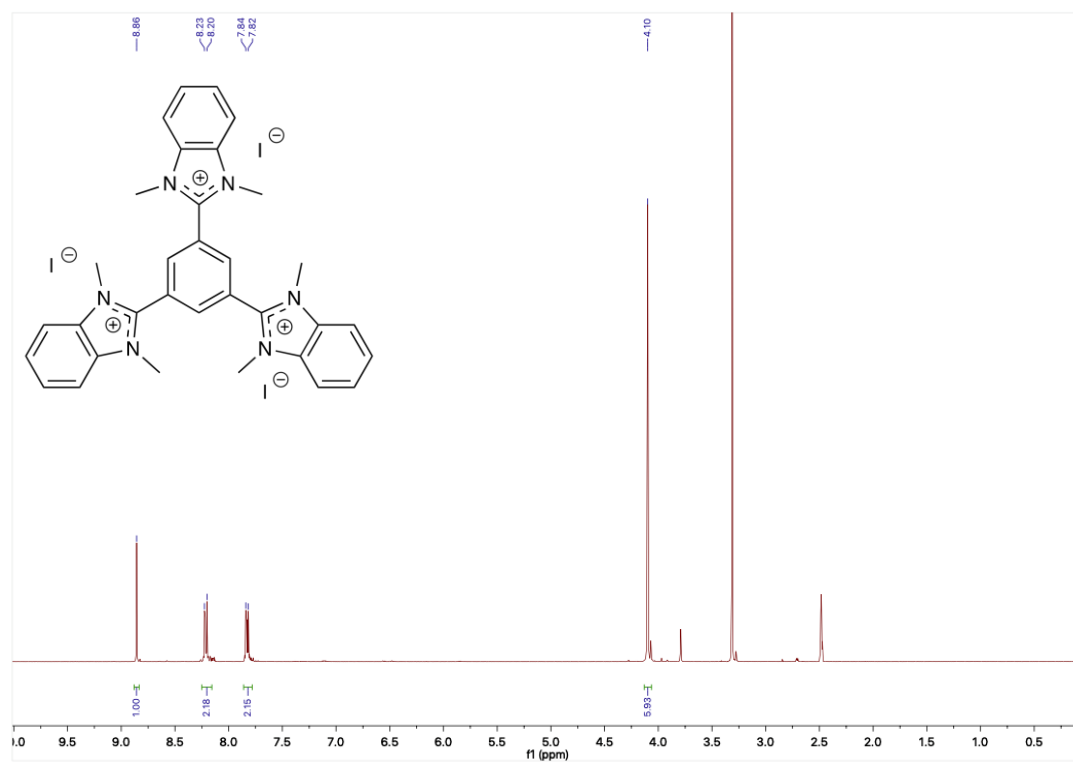
Figure S16. ^{1}H NMR in DMSO-d$_6$ of compound 7.
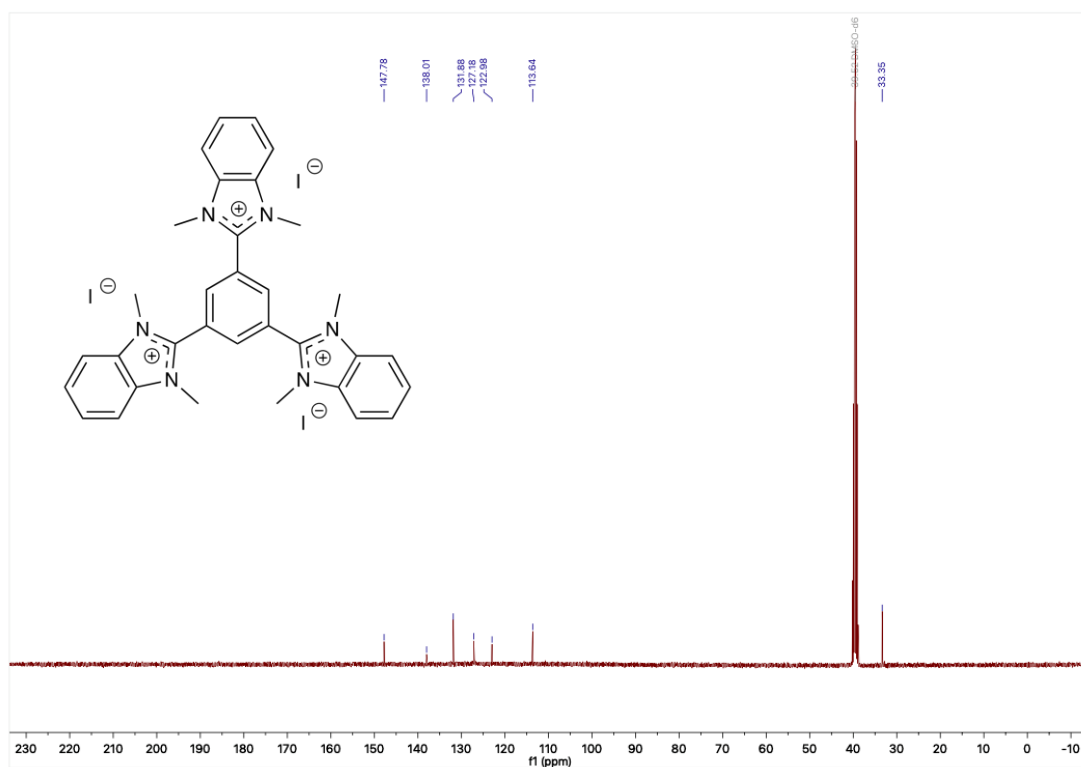
Figure S17. ^{13}C NMR in DMSO-d$_6$of compound 7.
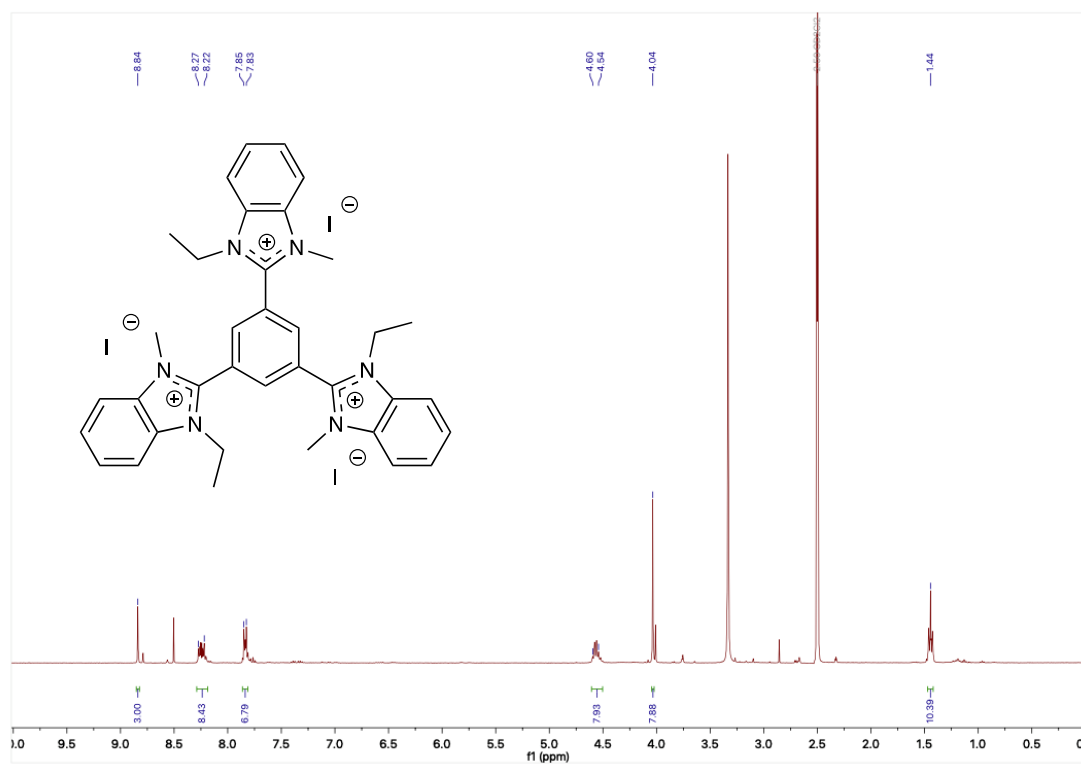
Figure S18. ^{1}H NMR in DMSO-d$_6$ of compound 10.
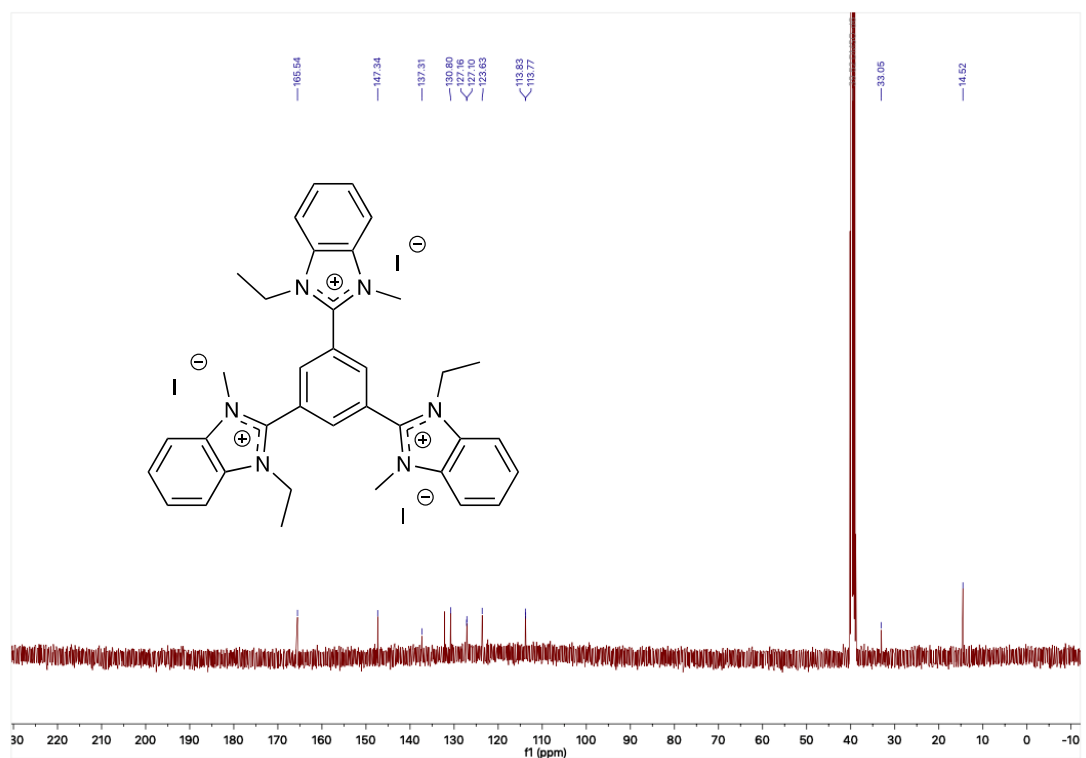
Figure S19. ^{13}C NMR in DMSO-d_6 of compound 10.

Results and Discussion

HR-MS spectra:

This paragraph shows the HR-MS spectra from **8**, **9, 11**, **13** Main Text Paragraph. Compounds **7**, **10** and **12** could be not protonated with ESI.
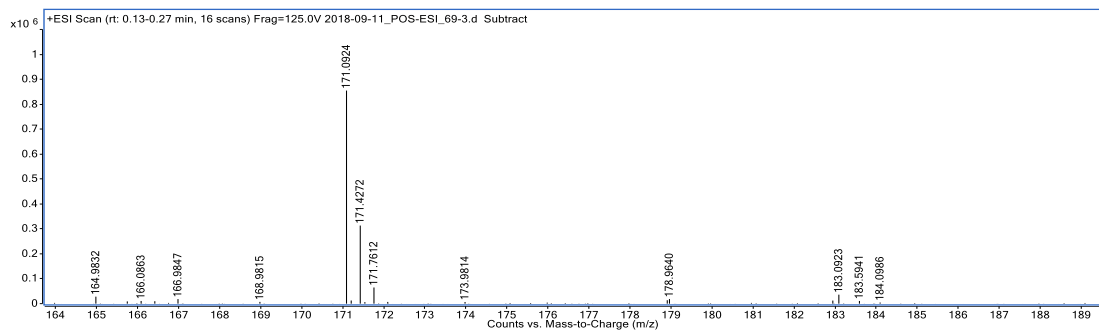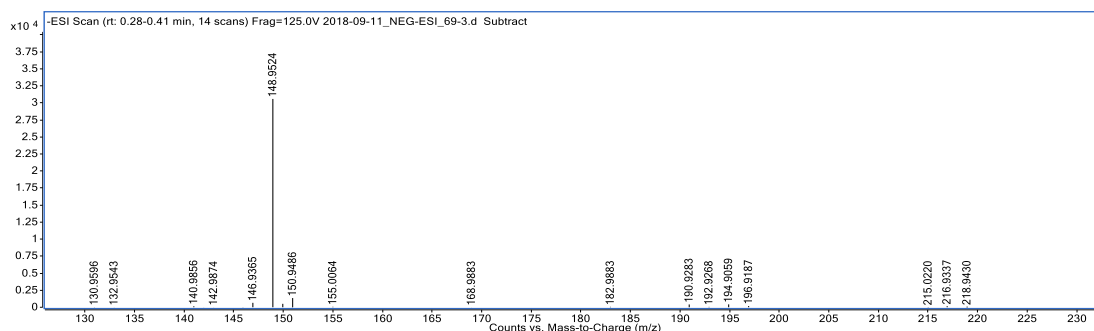
Figure S20. HR-MS spectra of compound **8**. Positive ion mode on the top and negative ion mode on the bottom.
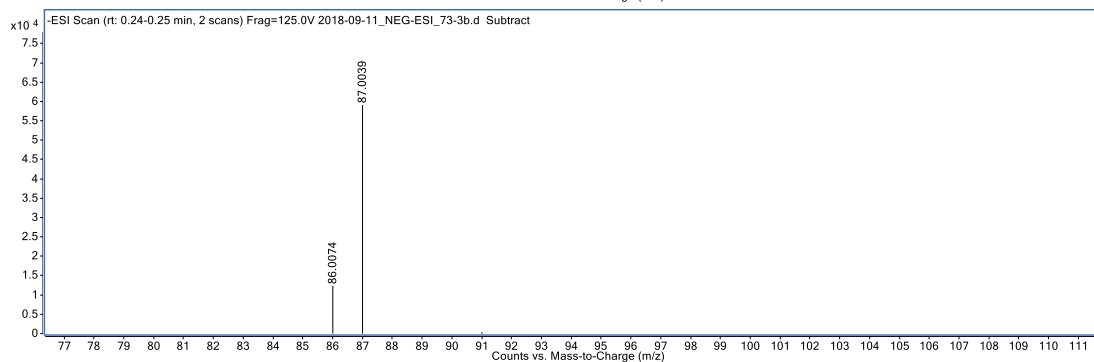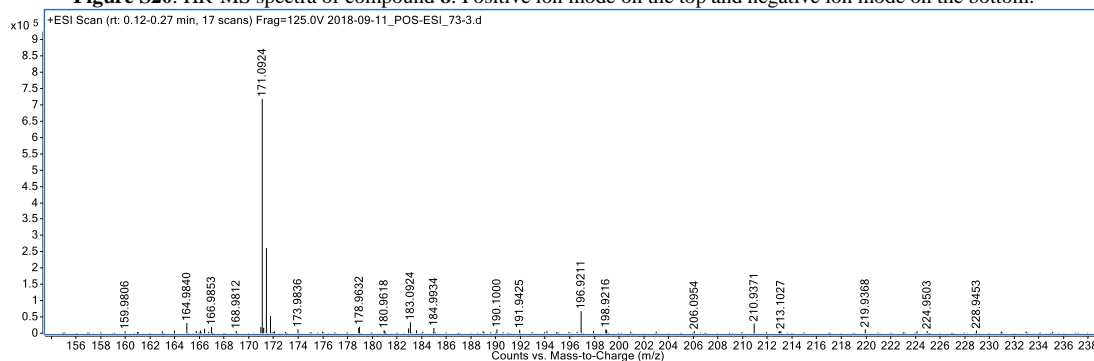
Figure S21. HR-MS spectra of compound **9**. Positive ion mode on the top and negative ion mode on the bottom.
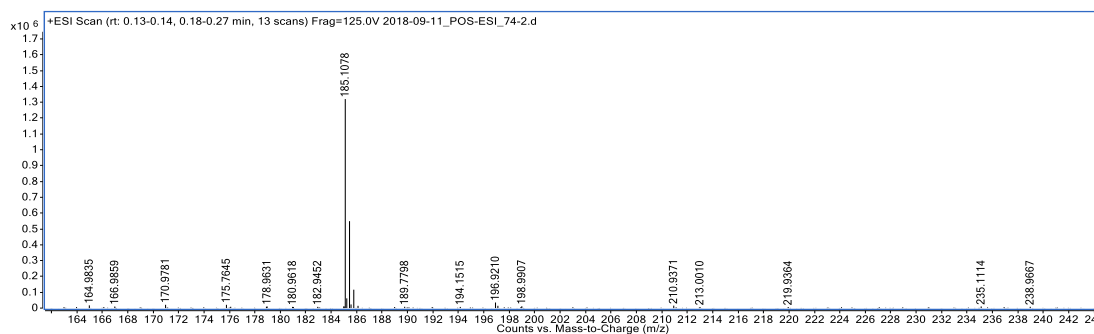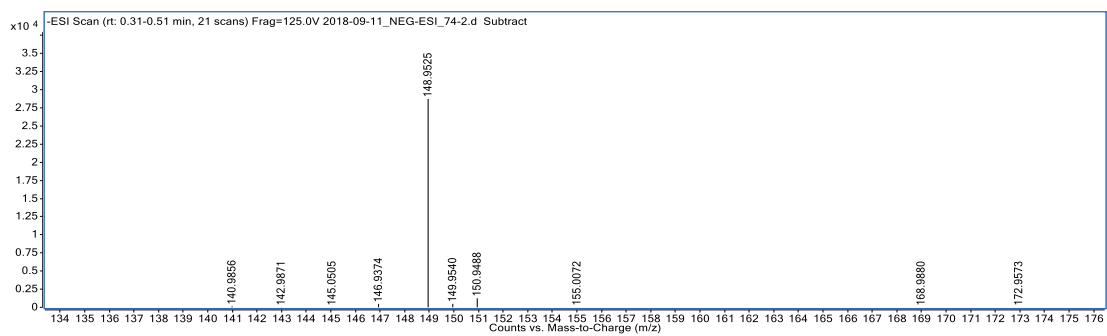
Figure S22. HR-MS spectra of compound **11**. Positive ion mode on the top and negative ion mode on the bottom.
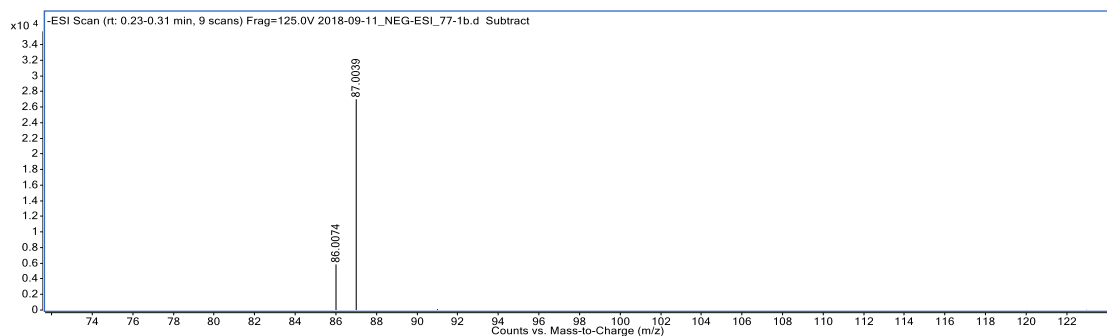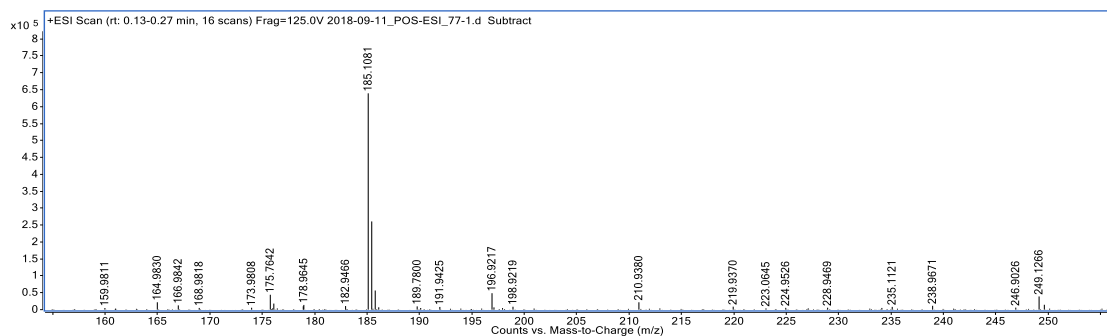
Figure S23. HR-MS spectra of compound **13**. Positive ion mode on the top and negative ion mode on the bottom.

108

Raman spectroscopy:
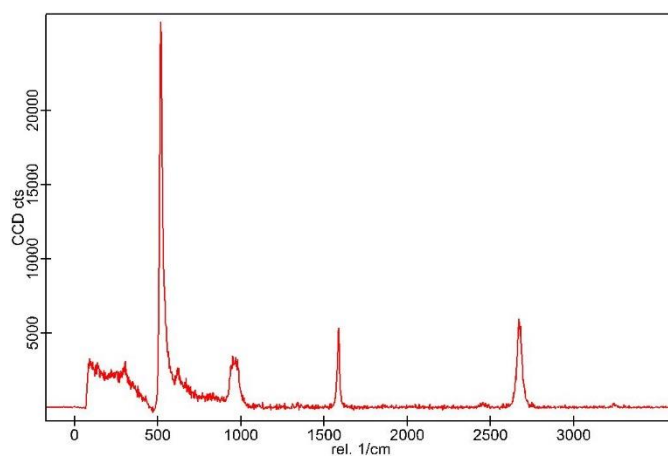
Figure S24. Raman spectrum of used CVD graphene, showing clearly the characteristic G and 2D bands of graphene.
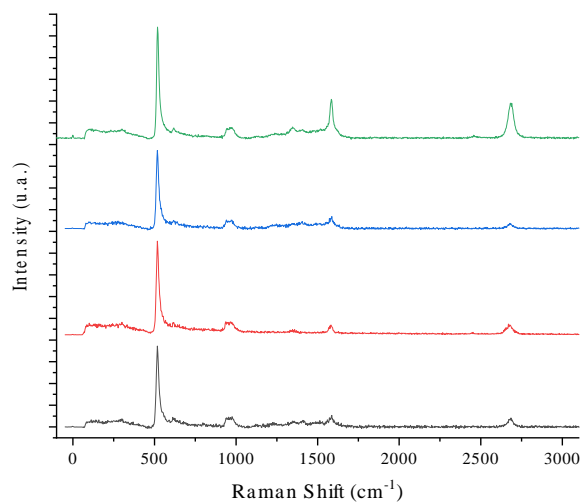
Figure S25. Raman spectra of non-covalently functionalized CVD graphene. Green curve: functionalized with **12**, blue curve: functionalized with **11**, red curve: functionalized with **7** derivative, black curve: functionalized with **5**.
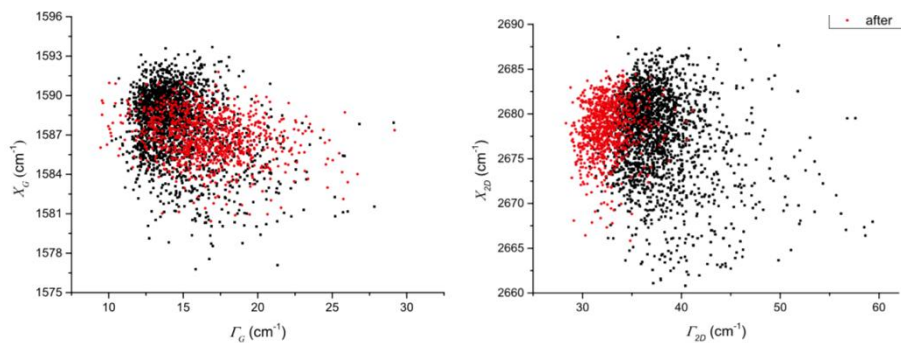
Figure S26. Scatter plot of the G peak (left side) and 2D peak (right side) of CVD graphene (black) and with molecule **8** functionalized CVD graphene (red).

All Raman spectra were fitted by Lorenzian functions to extract the G and 2D peaks. The CVD graphene sample (pristine graphene) gives a G peak at 1588 cm^{-1} (X_G, median value, **Figure S26**, left side in black) and the non-covalently functionalized graphene gives a G peak at 1586 cm^{-1} (median value, **Figure S26**, left side in red), indication a shift of 2.0 cm^{-1} for X_G. The full width at half maximum (FWHM) Γ_G of the G peak is at 14.2 cm^{-1} (median value, **Figure S26**, left side in black) for the CVD graphene sample and widens to 16.3 cm^{-1} (median value, **Figure S26**, left side in red) for the functionalized graphene sample. That leads to a shift of 2.1 cm^{-1} of Γ_G. Figure 13 shows the scatter plot of Γ_G against X_G.

Also, a significant change between the CVD graphene and the non-covalently functionalized graphene can be observed by analyzing the 2D peak for both samples. Both, the graphene sample as well as the non-covalently functionalized graphene give a 2D peak at 2678 cm^{-1} (median values, **Figure S26**, right side). The FWHM Γ_{2D} of the 2D peak of the graphene sample is 36.9 cm^{-1} (median value, **Figure S26**, right side in black) and stiffens to 32.2 cm^{-1} (median value **Figure S26**, right side in red) for the non-covalently functionalized graphene sample. That leads to a shift of 4.7 cm^{-1} of Γ_{2D}. Figure 14 shows the scatter plot of Γ_{2D} against X_{2D}.

X-ray photoelectron spectroscopy
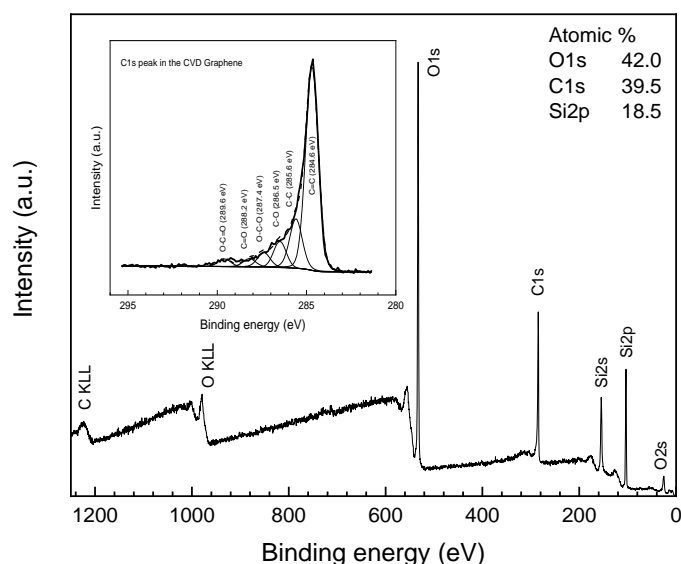
Figure S27. XPS survey spectrum of the CVD graphene and the corresponding spectrum of C1s peak.
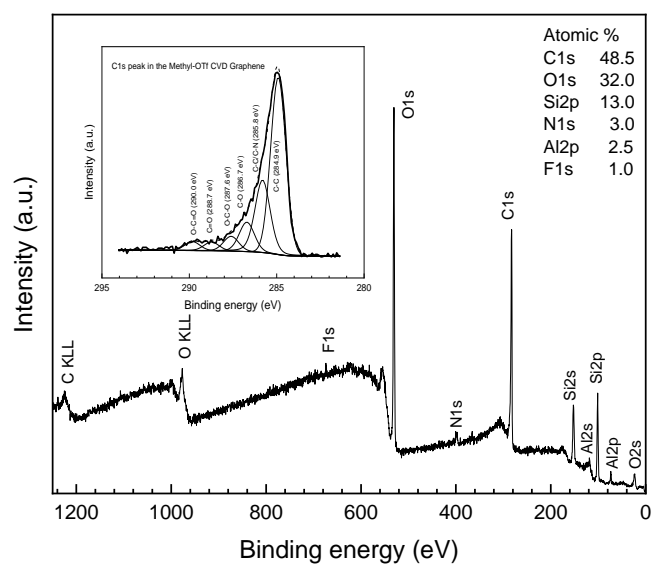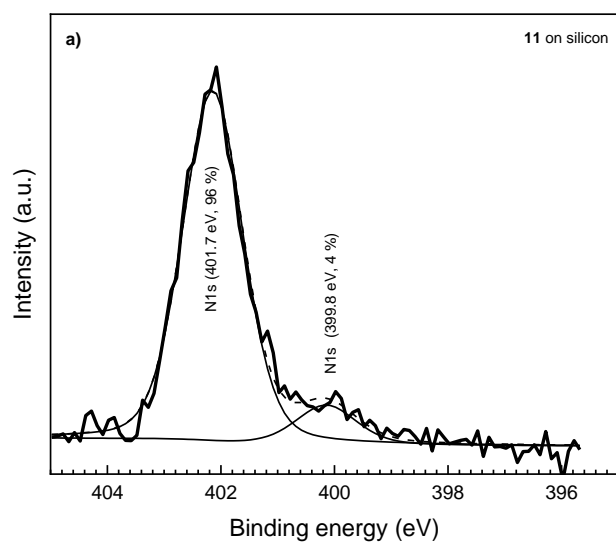
110

Figure S28. XPS survey spectrum of molecule **8** on CVD graphene and the corresponding spectrum of C1s peak.
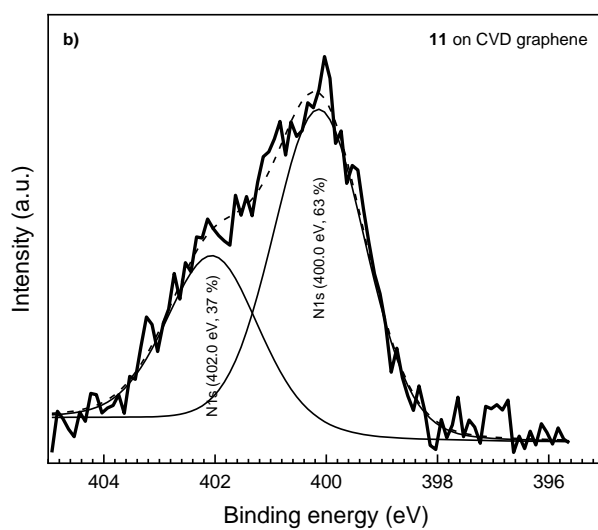
Figure S29. High resolution scan at the N1s region for a) **11** on silicon and b) **11** on CVD graphene.
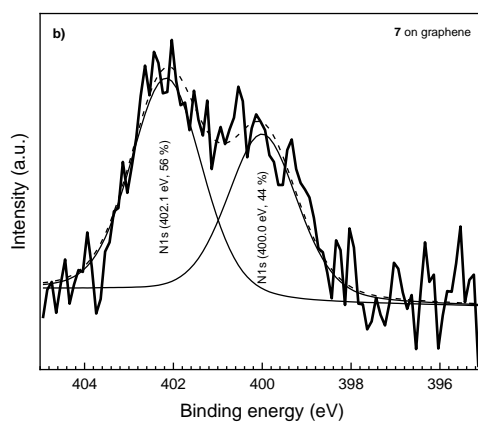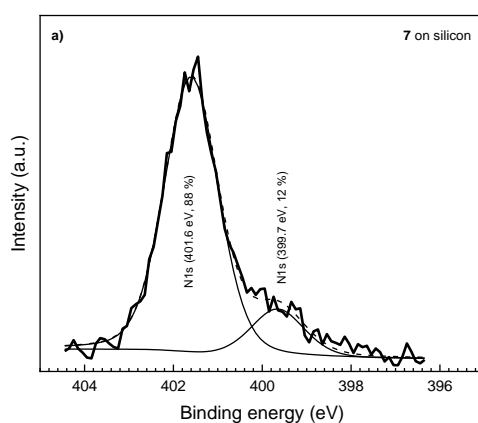

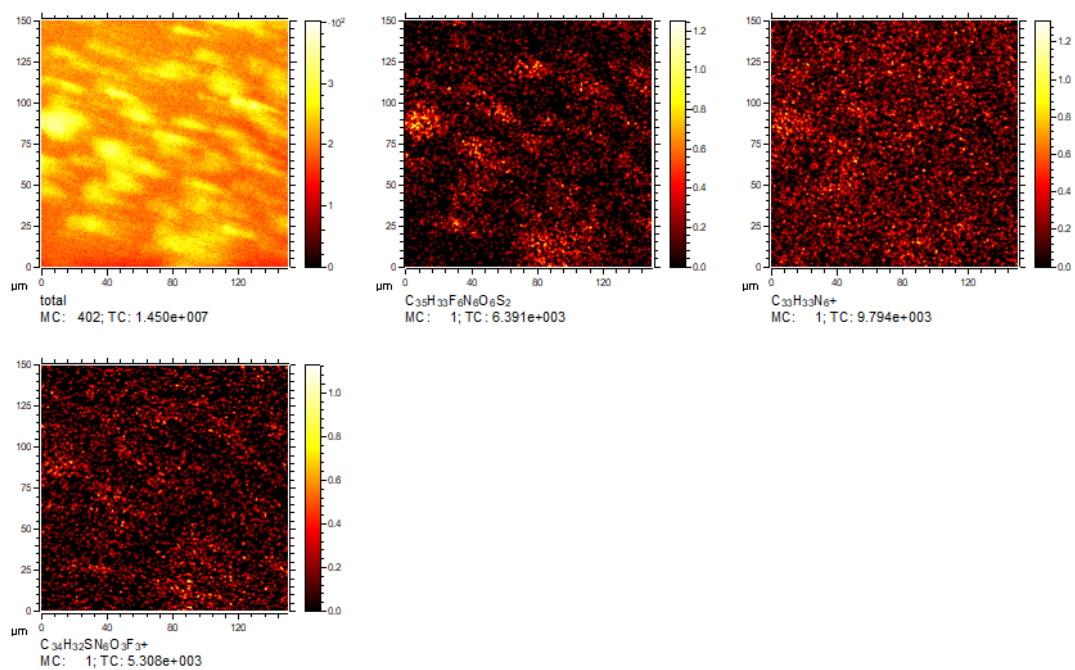**Figure S30**. High resolution scan at the N1s region for a) **7** on silicon and b) **7** on CVD graphene.

Figure S31. ToF-SIMS images in positive ion mode showing a) total amount of found m/z signals, b) m/z = 787.2 c) m/z = 513.28 and d) m/z = 662.73. Surface scan area: 150 μm x 150 μm.
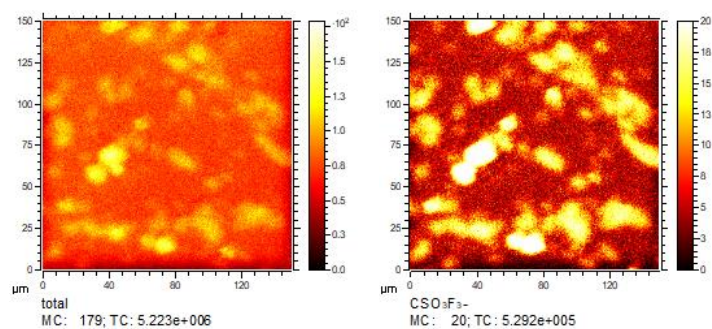
Figure S32. ToF-SIMS images in negative ion mode showing a) total amount of found m/z signals and b) m/z = 148.95. Surface scan area: 150 μm x 150 μm.
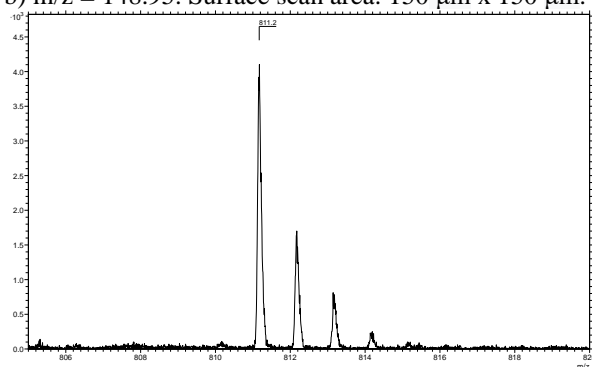

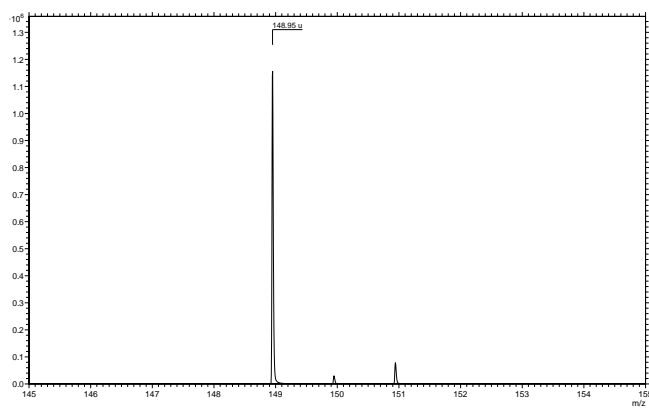**Figure S33**. ToF-SIMS spectrum in positive ion mode showing m/z = 811.2.

Figure S34. ToF-SIMS spectrum in negative ion mode showing m/z = 148.95.
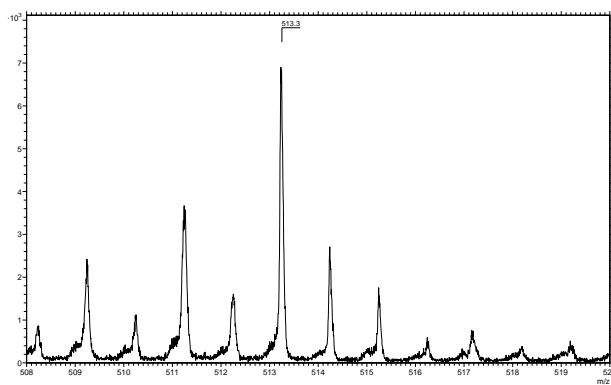

Figure S35. ToF-SIMS spectrum in positive ion mode showing m/z = 512.3.
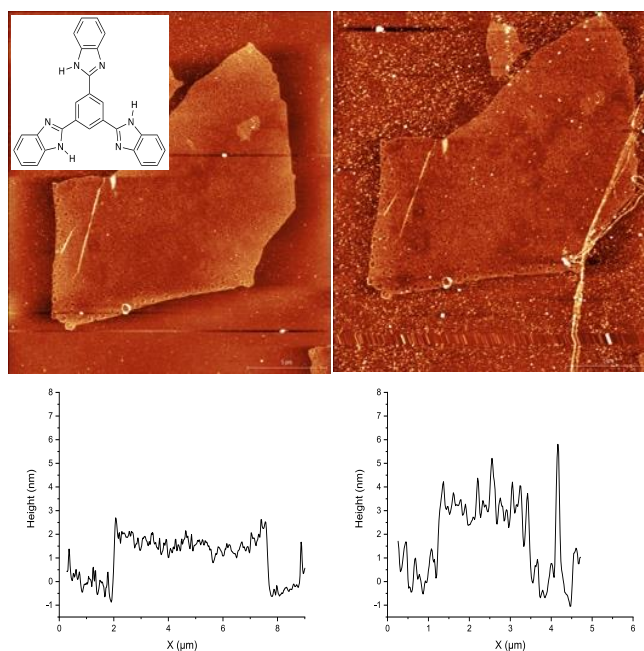
Atomic Force Microscopy

Figure S36. a) AFM image of reduced-oxo-G and with moleculare structure of **4**. b) AFM image of with **4** non-covalently functionalized reduced-oxo-G. c) High profile of reduced-oxo-G. d) High profile of with **4** non-covalently functionalized reduced-oxo-G.
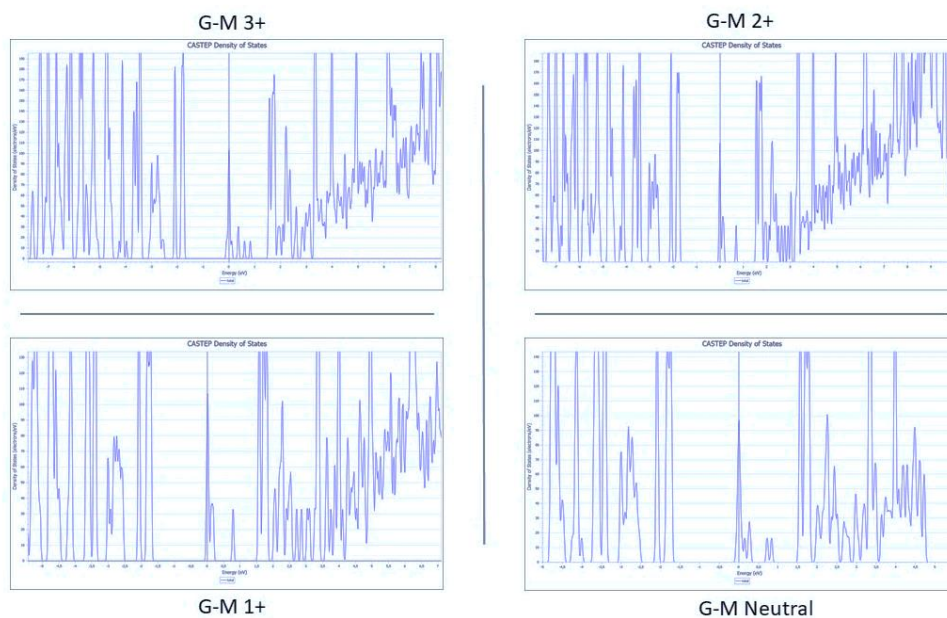
Discrete Fourier Transform Calculations

Figure S37. *a)* Details of the densities of States for G-M complexes with different charges. Notice the similar structures around the Fermi level.

G-M 3+
HOMO

G-M 2+
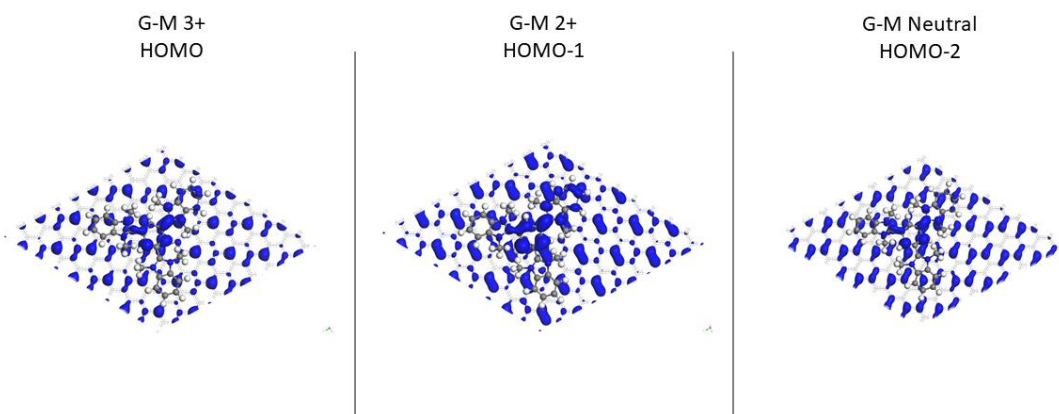HOMO-1

G-M Neutral
HOMO-2

Figure S38. *a)* Relevant orbitals for the charged G-M complexes.

In as much as DFT predicts electron transfer from graphene to tricationic molecule **6**, further signatures for such reduction of ionic charge, from 8^{3+} to 8^{2+}, is provided here. Thus, Raman spectra for 8^{3+}, 8^{2+}, and 8^{1+} in the gas phase have been computed. Indeed, it is the assumed non-covalent nature of the bonding between cation and graphene that implies changes in the Raman spectra of the molecular ions in the gas phase to be relevant. The qualitative differences in computed spectra allow the further validation of the non-covalent bonding. Hence, support for single-electron transfer is arrived at by matching the experimental Raman spectra of tricationic molecule **8** *(Figure 4A)* in solution to the computed Raman spectrum of the 8^{3+} charged moiety **6** in the gas phase *(Figure S59)*, and tricationic molecule **8** on CVD graphene **8** *(Figure 4B)* to the computed Raman spectrum of 8^{2+}, while excluding the 8^{1+}.
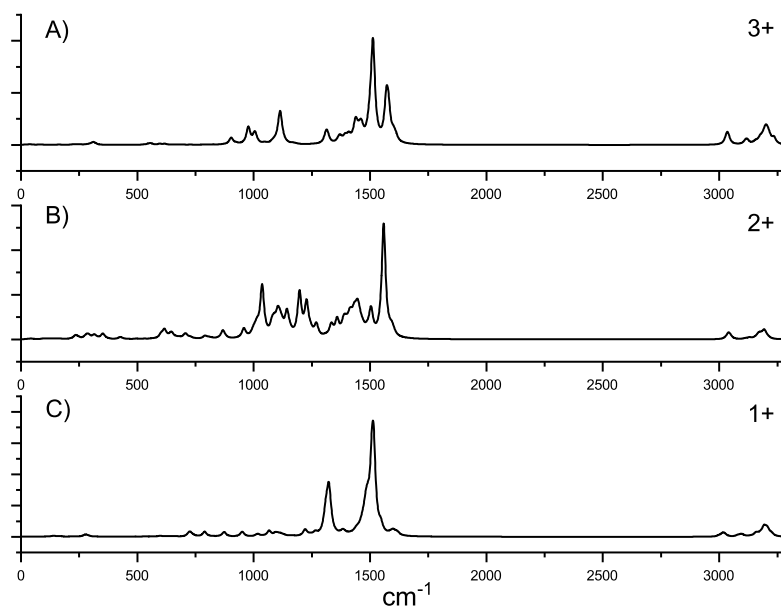

Figure S39. Comparison between calculated and measured Raman spectra of A) molecule **8**, b) the reduced species of **8** and C) the twice reduced species of **8**.

Cyclic Voltammetry characterization of 9:

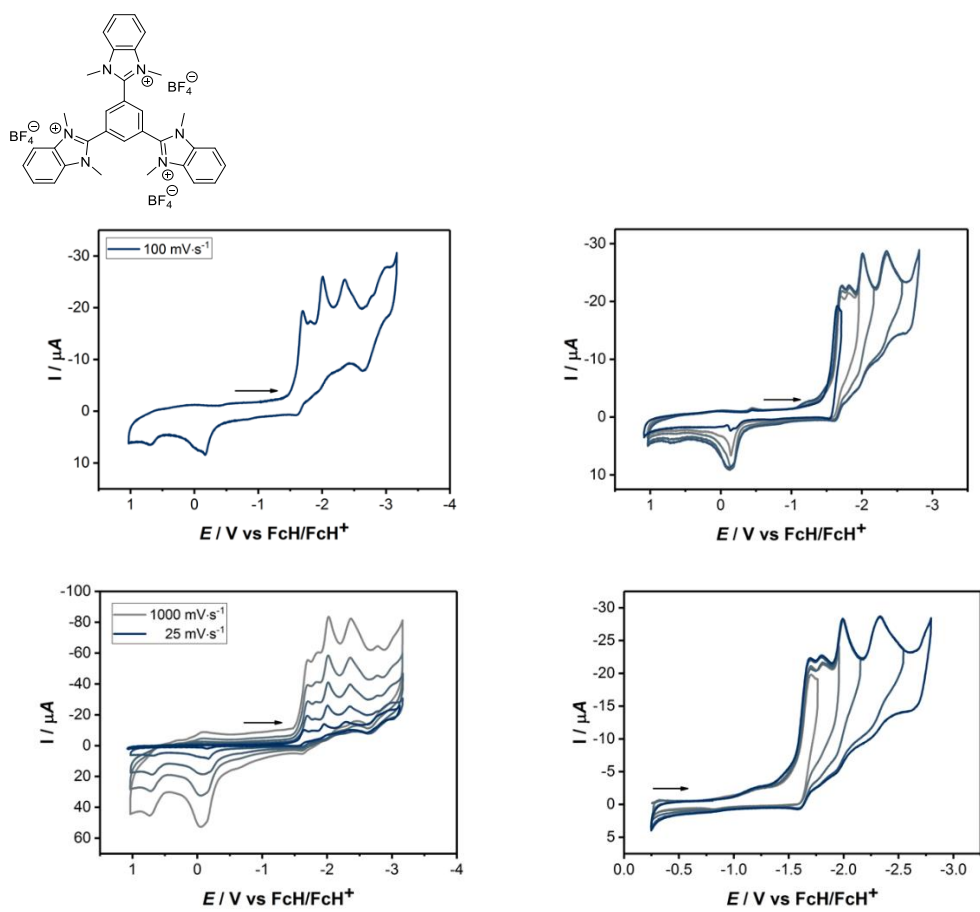

Figure S40. Cyclic voltammetry of **9** in ACN (+0.1 M Bu$_4$NPF$_6$) at different scan rates.
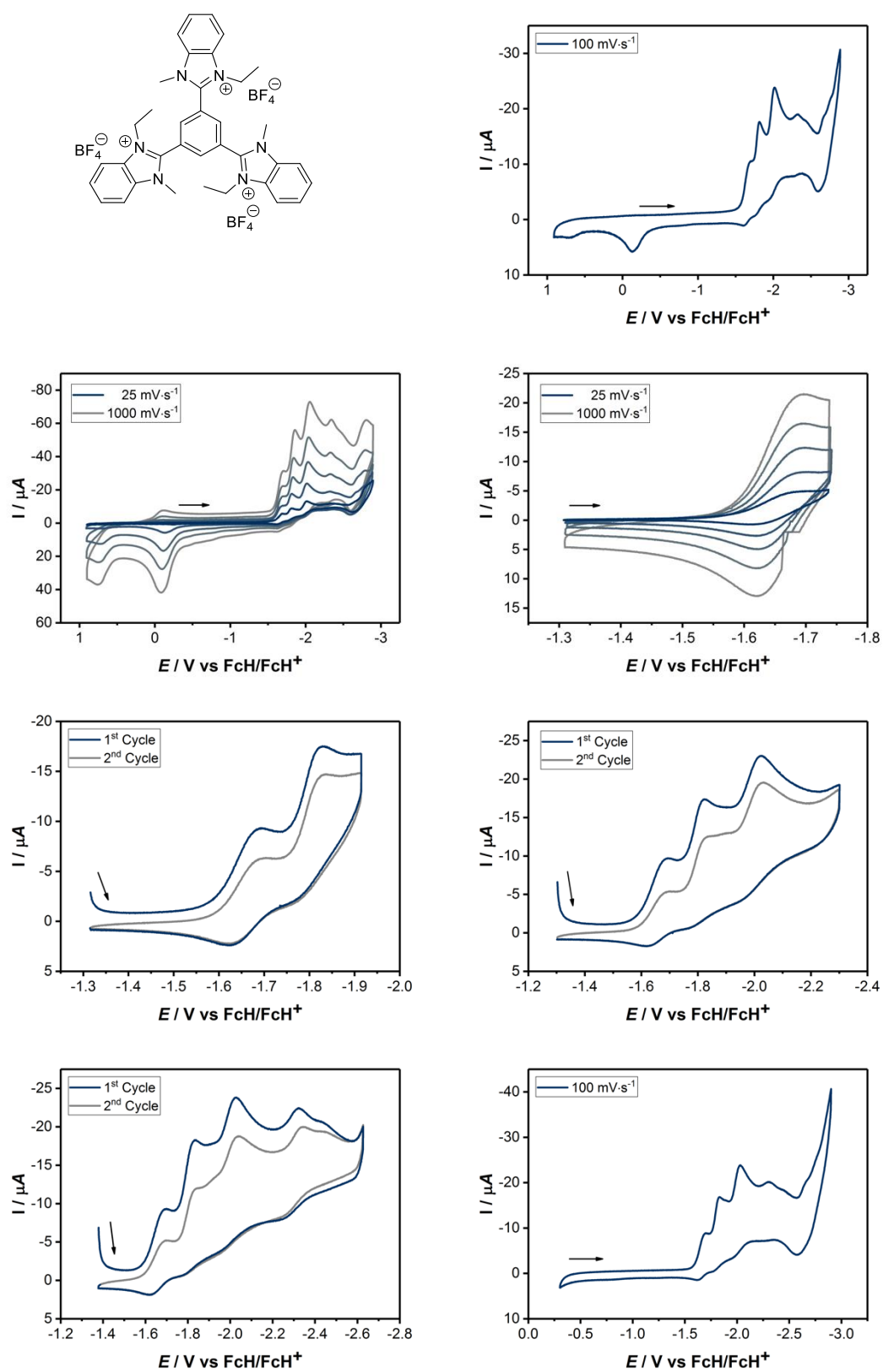
Cyclic Voltammetry characterization of 12:

Figure S41. Cyclic voltammetry of **12** in ACN (+0.1 M *Bu₄NPF₆*) at different scan rates.

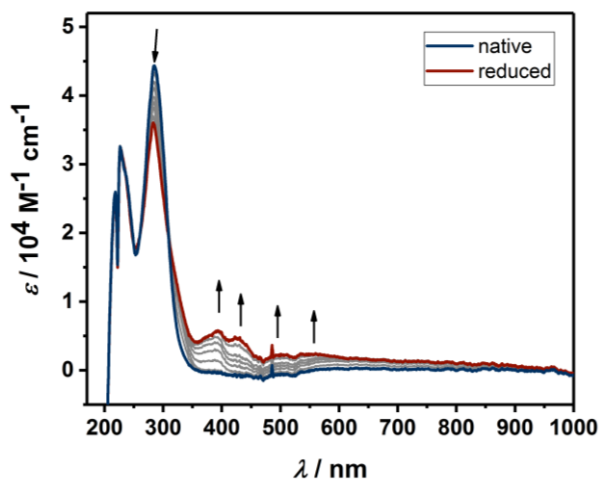**UV-Vis-NIR spectroelectrochemistry of 12:**

Figure S42. Changes in the UV-vis-NIR spectrum of **12**, during first reduction.

Table S1. In-situ spectroscopy for the native species (**12**)

Wavelength [nm]	Extinction coefficient [M^{-1}·cm^{-1}]
218	25710
227	32550
285	44370

Table S1. In-situ spectroscopy for the reduced species (**12**)

Wavelength [nm]	Extinction coefficient [M^{-1}·cm^{-1}]
218	25710
227	32550
285	35880
393	2785
423	4885
506	2270
553	2360

References

[1]   N. Chandrashekhar, B. Thomas, V. Gayathri, K. V. Ramanathan, N. M. Gowda, *Magn. Reson. Chem.* 2008, 46, 769.

[2]   W. K. Fife, P. Ranganathan, M. Zeldin, *J. Org. Chem.* 1990, 55, 5610-5613.

[3]   C. K. Chua, M. Pumera, *Chem.: Eur. J.* 2013, *19*, 2005-2011.

[4]   M. Krejčik, M. Daněk, F. Hartl, *J. Electroanal. Chem. Interfacial Electrochem*. 1991, *317*, 179.

5. Summary and outlook

During the past three years, my researches mainly focused on the fundamental research of oxo-G including atomic structures evolutions during thermal decomposition process and room-temperature electrical transport performances at single layer level. Some interesting findings were obtained and some significant problems were addressed. These fundamental studies can help to better understand the oxo-G derivatives and promote more tailored applications.

In the first part of the thesis, the substrate effect on the electronic transport of reduced oxo-G with a density of defects of about 0.5% ($^{0.5\%}$G) was studied. The devices composed of monolayer $^{0.5\%}$G, partially deposited on SiO_2 and hexagonal boron nitride (h-BN) were used for transport measurements. The $^{0.5\%}$G was a p-doped material and defects determined the scattering of charge carriers. Using h-BN as substrate led to less trapped molecules, which were responsible for p-doping. In this regard, most likely hydrogen-bonded water and other cleaved oxo-species were captured between SiO_2 and $^{0.5\%}$G causing p-doping, as a consequence of chemical reduction of oxo-G. The ambipolar behavior with a Dirac point of +20 V was observed for the h-BN/$^{0.5\%}$G structure while unipolar p-type response was shown for the same $^{0.5\%}$G flake on SiO_2. Transfer characteristics showed a reduction of hysteresis in the h-BN/$^{0.5\%}$G. The mobility of the SiO_2/$^{0.5\%}$G was determined to 7.4 -14.5 cm^2 V^{-1} s^{-1} and for h-BN/$^{0.5\%}$G to 5.6-8.5 cm^2 V^{-1} s^{-1} at ambient conditions. The h-BN/$^{0.5\%}$G structure has important applications in highly sensitive chemically-derived graphene based sensors.

In the second part of the thesis, room-temperature electrical properties of single-layer graphene derived from oxo-G containing defect densities varying from 0.2% to 1.5% was studied. The defects gave rise to a heterogeneous topographical morphology of oxo-G. The isolated graphene domains ($L_D \leq 3$ nm) in oxo-G were identified by Raman spectroscopy. The isolation of these domains limited the charge transport in reduced oxo-G. Therefore, the mobility values of charge carriers of graphene with densities of defects between 0.2% and 1.5%, changed by three orders of magnitude, from 0.3 cm^2 V^{-1} s^{-1} and 33.2 cm^2 V^{-1} s^{-1}. The mobility of charge carriers varied by orders of magnitude even though it looks like that the density of defects varies only a little. The fundamental findings reported here can explain the generally diverging results often reported for reduced graphene oxide used in applications.

In the third part of the thesis, the defect structures including holes and bilayer C-C sp^3-patches induced by thermal disproportion of the oxo-G were demonstrated. The identified C-C sp^3-patches, which were connected to nm-sized patches of the hexagonal carbon lattice in graphene, were separated by grain boundaries and holes which were 5 nm in diameter. We suggested that C-C sp^3-bonds were formed either after folding or adsorption of carbon patches, indicating that reactive species were formed in the course of the disproportionation reaction. The STS results turned out that the nanometer-sized sp^3 bilayer structures had a bandgap of ~ 0.4 eV. Our study indicates that the graphene with the sp^3-C in double layer areas are interesting semiconducting materials. With these deeper insights of the thermal disproportionation of oxo-G and correlation to the electrical properties future applications may come into reach. In particular, the formation of holes and sp^3-stacked regions potentially play a significant role for chemical reactions used to post-functionalize materials. Moreover, bottom-up synthesized molecular

carbon materials containing sp^3- and sp^2-carbon with a tunable band-gap might be discovered in the future.

6. Zusammenfassung und Ausblick

Während der letzten drei Jahre konzentrierte sich meine Forschung vorrangig auf die grundlegende Untersuchung von oxo-G, die Entwicklung von atomaren Strukturen während dessen thermischer Zersetzung sowie die elektrische Transportleistung einzelner Schichten des Materials bei Raumtemperatur. Diese fundamentalen Untersuchungen, bei welchen interessante Ergebnisse erzielt und wichtige Fragen beleuchtet wurden, tragen zu einem besseren Verständnis der Eigenschaften der oxo-G-Derivate bei und können die Entwicklung maßgeschneiderter Anwendungen fördern.

Im ersten Teil der Arbeit wurde der Effekt des verwendeten Substrats auf den elektronischen Transport in reduziertem oxo-G mit einer Defektdichte von ca. 0.5% ($^{0.5\%}$G) untersucht. Die hierzu verwendeten devices bestehen aus $^{0.5\%}$G-Monolagen, welche teilweise auf SiO$_2$ und hexagonalem Bornitrid (h-BN) aufgebracht sind. $^{0.5\%}$G ist ein p-dotiertes Material in welchem dessen Defekte für die Streuung der Ladungsträger verantwortlich sind. Die Verwendung von h-BN führt zu einer geringeren Anzahl an zwischen den Schichten eingeschlossenen Molekülen, welche eine p-Dotierung verursachen. Hierbei handelt es sich vermutlich um durch Wasserstoffbrückenbindungen zwischen den Schichten gebundene Wassermoleküle und andere oxo-Spezies, welche durch die chemische Reduktion des oxo-Gs zwischen dem SiO$_2$ – Substrat und der $^{0.5\%}$G-Monolage entstehen. Die h-BN/$^{0.5\%}$G-Struktur zeigte ambipolares Verhalten mit einem Diracpunkt von +20 V, während für den Teil derselben Flocke, welcher auf dem SiO$_2$ – Substrat auflag, unipolare p-Dotierung nachgewiesen wurde. Die Transfercharakteristik zeigt eine reduzierte Hysterese für die h-BN-Struktur. Für die Mobilität der SiO$_2$/$^{0.5\%}$G-Struktur bei normalen Umgebungsbedingungen ergibt sich ein Wert von 7.4 -14.5 cm^2 V^{-1} s^{-1} , während für die h-BN/$^{0.5\%}$G-Struktur 5.6-8.5 cm^2 V^{-1} s^{-1} gemessen wurde. Die h-BN/$^{0.5\%}$G-Struktur hat bedeutende Anwendung in hochempfindlichen, Graphen-basierten chemischen Sensoren.

Im zweiten Teil der Arbeit wurden die elektrischen Eigenschaften von Graphen-Monolagen bei Raumtemperatur untersucht, mit Defektdichten von 0,2% bis 1,5% bei Raumtemperatur untersucht. Die Defekte resultieren in einer heterogenen Morphologie des oxo-Gs. Isolierte Bereiche unfunktionalisierten Graphens (L$_D$ ≤ 3 nm) im oxo-G-Gitter wurden durch Raman-Spektroskopie nachgewiesen. Der Abstand dieser Graphendomänen beeinflusst den Ladungstransport in reduziertem oxo-G. Folglich verändern sich auch die gemessenen Mobilitäten abhängig von der Defektdichte zwischen 0,2% - 1,5% von 0.3 cm^2 V^{-1} s^{-1} zu 33.2 cm^2 V^{-1} s^{-1}. Obwohl die Defektdichte nur wenig variiert, ändert sich die Mobilität der Ladungsträger um mehrere Größenordnungen. Die hier gefundenen grundlegenden Erkenntnisse erklären die generell divergierenden Ergebnisse, welche oft für reduziertes Graphenoxid in Anwendungen berichtet werden.

Im dritten Teil der Arbeit wurden durch die thermische Zersetzung von oxo-G entstehende Defektstrukturen wie Löcher und Bereiche C-C- sp^3-verknüpfter Doppelschichten untersucht. Die sp^3-verknüpften Bereiche sind innerhalb des hexagonalen Graphengitters durch Korngrenzen und Löcher mit einem Durchmesser von durchschnittlich 5 nm getrennt. Wir vermuten, dass die C-C- sp^3-Bindungen

nach der Faltung oder Adsorption der aufgefalteten Bereiche gebildet werden, was impliziert, dass im Verlauf der Disproportionierungsreaktion reaktive Spezies gebildet werden. In STS-Messungen wurde die für Bandlücke dieser nanometergroßen sp^3-Doppelschichtstrukturen ein Wert von ca. 0,4 eV gefunden. Unsere Untersuchungen deuten darauf hin, dass Graphen mit solchen sp^3-Defekten ein vielversprechendes Halbleitermaterial darstellt. Das tiefere Verständnis der thermischen Disproportionierung von oxo-G und deren Zusammenhang mit den elektrischen Eigenschaften ermöglicht zukünftige Anwendungen. Besonders die Bildung von Löchern und sp^3-verknüpften Schichten könnte eine wichtige Rolle für die chemische Funktionalisierung von Materialien spielen. Darüber hinaus könnten zukünftig durch bottom-up-Synthesen hergestellte Kohlenstoff-Nanomaterialien endeckt werden, welche sp^3- sowie sp^2-hybridisierten Kohlenstoffatome enthalten und folglich eine abstimmbare Bandlücke besitzen.

7. References

[1] A. H. Castro Neto, F. Guinea, N. M. R. Peres, K. S. Novoselov and A. K. Geim, *Rev. Mod. Phys.* **2009**, *81*, 109-162.

[2] S. Y. Zhou, G. H. Gweon, A. V. Fedorov, P. N. First, W. A. De Heer, D. H. Lee, F. Guinea, A. H. Castro Neto and A. Lanzara, *Nat. Mater.* **2007**, *6*, 916-916.

[3] N. Tombros, C. Jozsa, M. Popinciuc, H. T. Jonkman and B. J. van Wees, *Nature* **2007**, *448*, 571-U574.

[4] a) K. I. Bolotin, K. J. Sikes, Z. Jiang, M. Klima, G. Fudenberg, J. Hone, P. Kim and H. L. Stormer, *Solid State Commun.* **2008**, *146*, 351-355; b) K. S. Novoselov, A. K. Geim, S. V. Morozov, D. Jiang, M. I. Katsnelson, I. V. Grigorieva, S. V. Dubonos and A. A. Firsov, *Nature* **2005**, *438*, 197-200; c) S. Das Sarma, S. Adam, E. H. Hwang and E. Rossi, *Rev. Mod. Phys.* **2011**, *83*, 407-470; d) J. H. Chen, C. Jang, S. Adam, M. S. Fuhrer, E. D. Williams and M. Ishigami, *Nat. Phys.* **2008**, *4*, 377-381.

[5] D. R. Dreyer, S. Park, C. W. Bielawski and R. S. Ruoff, *Chem. Soc. Rev.* **2010**, *39*, 228-240.

[6] W. Gao, L. B. Alemany, L. J. Ci and P. M. Ajayan, *Nat. Chem.* **2009**, *1*, 403-408.

[7] W. W. Cai, R. D. Piner, F. J. Stadermann, S. Park, M. A. Shaibat, Y. Ishii, D. X. Yang, A. Velamakanni, S. J. An, M. Stoller, J. H. An, D. M. Chen and R. S. Ruoff, *Science* **2008**, *321*, 1815-1817.

[8] A. M. Dimiev, L. B. Alemany and J. M. Tour, *ACS Nano* **2013**, *7*, 576-588.

[9] S. Eigler, C. Dotzer, A. Hirsch, M. Enzelberger and P. Muller, *Chem. Mater.* **2012**, *24*, 1276-1282.

[10] S. Eigler, M. Enzelberger-Heim, S. Grimm, P. Hofmann, W. Kroener, A. Geworski, C. Dotzer, M. Rockert, J. Xiao, C. Papp, O. Lytken, H. P. Steinruck, P. Müller and A. Hirsch, *Adv.Mater.* **2013**, *25*, 3583-3587.

[11] M. A. Velasco-Soto, S. A. Perez-Garcia, J. Alvarez-Quintana, Y. Cao, L. Nyborg and L. Licea-Jimenez, *Carbon* **2015**, *93*, 967-973.

[12] H. M. Huang, Z. B. Li, J. C. She and W. L. Wang, *J. Appl. Phys.* **2012**, *111*, 054317

[13] P. Feicht, J. Biskupek, T. E. Gorelik, J. Renner, C. E. Halbig, M. Maranska, F. Puchtler, U. Kaiser and S. Eigler, *Chem.Eur.J.* **2019**, *25*, 8955-8959.

[14] H. L. Poh, F. Sanek, A. Ambrosi, G. J. Zhao, Z. Sofer and M. Pumera, *Nanoscale* **2012**, *4*, 3515-3522.

[15] D. C. Marcano, D. V. Kosynkin, J. M. Berlin, A. Sinitskii, Z. Z. Sun, A. Slesarev, L. B. Alemany, W. Lu and J. M. Tour, *ACS Nano* **2010**, *4*, 4806-4814.

[16] a) H. T. Yu, B. W. Zhang, C. K. Bulin, R. H. Li and R. G. Xing, *Sci. Rep.* **2016**, *6*; b) W. S. Hummers and R. E. Offeman, *J. Am. Chem. Soc.* **1958**, *80*, 1339.

[17] A. Dimiev, D. V. Kosynkin, L. B. Alemany, P. Chaguine and J. M. Tour, *J. Am. Chem. Soc.* **2012**, *134*, 2815-2822.

[18] A. M. Dimiev and J. M. Tour, *ACS Nano* **2014**, *8*, 3060-3068.

[19] P. Feicht and S. Eigler, *ChemNanoMat* **2018**, *4*, 244-252.

[20] H. J. Jiang, *Small* **2011**, *7*, 2413-2427.

[21] F. Grote, C. Gruber, F. Borrnert, U. Kaiser and S. Eigler, *Angew.Chem.Int.Ed.* **2017**, *56*, 9222-9225.

[22] C. Gomez-Navarro, J. C. Meyer, R. S. Sundaram, A. Chuvilin, S. Kurasch, M. Burghard, K. Kern and U. Käiser, *Nano Lett.* **2010**, *10*, 1144-1148.

[23] C. Gomez-Navarro, R. T. Weitz, A. M. Bittner, M. Scolari, A. Mews, M. Burghard and K. Kern, *Nano Lett.* **2007**, *7*, 3499-3503.

[24] *Nature Nanotechnology*.

[25] S. Eigler, *Chem. Eur. J.* **2016**, *22*, 7012-7027.

[26] L. G. Cançado, A. Jorio, E. H. M. Ferreira, F. Stavale, C. A. Achete, R. B. Capaz, M. V. O. Moutinho, A. Lombardo, T. S. Kulmala and A. C. Ferrari, *Nano Lett.* **2011**, *11*, 3190-3196.

[27] a) L. G. Cançado, A. Jorio, E. H. M. Ferreira, F. Stavale, C. A. Achete, R. B. Capaz, M. V. O. Moutinho, A. Lombardo, T. S. Kulmala and A. C. Ferrari, *Nano Lett.* **2011**, *11*, 3190-3196; b) J. M. Engiert, P. Vecera, K. C. Knirsch, R. A. Schäfer, F. Hauke and A. Hirsch, *ACS Nano* **2013**, *7*, 5472-5482; c) M. M. Lucchese, F. Stavale, E. H. M. Ferreira, C. Vilani, M. V. O. Moutinho, R. B. Capaz, C. A. Achete and A. Jorio, *Carbon* **2010**, *48*, 1592-1597; d) A. C. Ferrari and D. M. Basko, *Nat. Nanotechnol.* **2013**, *8*, 235-246; e) L. G. Cançado, M. G. da Silva, E. H. M. Ferreira, F. Hof, K. Kampioti, K. Huang, A. Penicaud, C. A. Achete, R. B. Capaz and A. Jorio, *2D Mater.* **2017**, *4*, 025039-025050.

[28] P. Vecera, S. Eigler, M. Kolesnik-Gray, V. Krstić, A. Vierck, J. Maultzsch, R. A. Schafer, F. Hauke and A. Hirsch, *Sci. Rep.* **2017**, *7*, 45165-45171.

[29] a) F. Schwierz, *Nat. Nanotechnol.* **2010**, *5*, 487-496; b) B. B. Zhan, C. Li, J. Yang, G. Jenkins, W. Huang and X. C. Dong, *Small* **2014**, *10*, 4042-4065.

[30] P. Boggild, D. M. A. Mackenzie, P. R. Whelan, D. H. Petersen, J. D. Buron, A. Zurutuza, J. Gallop, L. Hao and P. U. Jepsen, *2D Mater.* **2017**, *4*, 042003-042035.

[31] K. I. Bolotin, K. J. Sikes, Z. Jiang, M. Klima, G. Fudenberg, J. Hone, P. Kim and H. L. Stormer, *Solid State Commun.* **2008**, *146*, 351-355.

[32] Q. B. Liu, C. Yu, Z. Z. He, G. D. Gu, J. J. Wang, C. J. Zhou, J. C. Guo, X. D. Gao and Z. H. Feng, *Appl. Surf. Sci.* **2018**, *454*, 68-73.

[33] D. De Fazio, D. G. Purdie, A. K. Ott, P. Braeuninger-Weimer, T. Khodkov, S. Goossens, T. Taniguchi, K. Watanabe, P. Livreri, F. H. L. Koppens, S. Hofmann, I. Goykhman, A. C. Ferrari and A. Lombardo, *ACS Nano* **2019**, *13*, 8926-8935.

[34] a) T. Kobayashi, N. Kimura, J. B. Chi, S. Hirata and D. Hobara, *Small* **2010**, *6*, 1210-1215; b) X. H. Zhang, Y. Zhang, Q. L. Liao, Y. Song and S. W. Ma, *Small* **2013**, *9*, 4045-4050.

[35] C. Y. Su, Y. P. Xu, W. J. Zhang, J. W. Zhao, X. H. Tang, C. H. Tsai and L. J. Li, *Chem. Mater.* **2009**, *21*, 5674-5680.

[36] a) R. Negishi, M. Akabori, T. Ito, Y. Watanabe and Y. Kobayashi, *Sci. Rep.* **2016**, *6*, 28936; b) C. Mattevi, G. Eda, S. Agnoli, S. Miller, K. A. Mkhoyan, O. Celik, D. Mastrogiovanni, G. Granozzi, E. Garfunkel and M. Chhowalla, *Adv. Funct. Mater.* **2009**, *19*, 2577-2583.

[37] H. J. Kim, D. Kim, S. Jung, S. N. Yi, Y. J. Yun, S. K. Chang and D. H. Ha, *J. Phys. Chem. C* **2015**, *119*, 28685-28690.

[38] J. B. Wu, M. L. Lin, X. Cong, H. N. Liu and P. H. Tan, *Chem. Soc. Rev.* **2018**, *47*, 1822-1873.

[39] a) X. Zhang, X. F. Qiao, W. Shi, J. B. Wu, D. S. Jiang and P. H. Tan, *Chem. Soc. Rev.* **2015**, *44*, 2757-2785; b) R. Beams, L. G. Cancado and L. Novotny, *J. Phys. Condens. Matter* **2015**, *27*, 083002.

[40] a) S. Eigler, F. Hof, M. Enzelberger-Heim, S. Grimm, P. Muller and A. Hirsch, *J. Phys. Chem. C* **2014**, *118*, 7698-7704; b) R. Rozada, J. I. Paredes, M. J. Lopez, S. Villar-Rodil, I. Cabria, J. A. Alonso, A. Martinez-Alonso and J. M. D. Tascon, *Nanoscale* **2015**, *7*, 2374-2390.

[41] C. J. Shearer, A. D. Slattery, A. J. Stapleton, J. G. Shapter and C. T. Gibson, *Nanotechnology* **2016**, *27*.

[42] J. Tersoff and D. R. Hamann, *Phys. Rev. B* **1985**, *31*, 805-813.

[43] R. Zan, C. Muryn, U. Bangert, P. Mattocks, P. Wincott, D. Vaughan, X. S. Li, L. Colombo, R. S. Ruoff, B. Hamilton and K. S. Novoselov, *Nanoscale* **2012**, *4*, 3065-3068.

[44] a) S. Marchini, S. Gunther and J. Wintterlin, *Phys. Rev. B* **2007**, *76*; b) A. T. N'Diaye, J. Coraux, T. N. Plasa, C. Busse and T. Michely, *New J. Phys.* **2008**, *10*; c) M. Ishigami, J. H. Chen, W. G. Cullen, M. S. Fuhrer and E. D. Williams, *Nano Lett.* **2007**, *7*, 1643-1648.

[45] R. Decker, Y. Wang, V. W. Brar, W. Regan, H. Z. Tsai, Q. Wu, W. Gannett, A. Zettl and M. F. Crommie, *Nano Lett.* **2011**, *11*, 2291-2295.

[46] a) X. L. Li, G. Y. Zhang, X. D. Bai, X. M. Sun, X. R. Wang, E. Wang and H. J. Dai, *Nat. Nanotechnol.* **2008**, *3*, 538-542; b) J. D. Mangadlao, C. M. Santos, M. J. L. Felipe, A. C. C. de Leon, D. F. Rodrigues and R. C. Advincula, *Chem Comm* **2015**, *51*, 2886-2889.

[47] a) H. J. Shin, K. K. Kim, A. Benayad, S. M. Yoon, H. K. Park, I. S. Jung, M. H. Jin, H. K. Jeong, J. M. Kim, J. Y. Choi and Y. H. Lee, *Adv. Funct. Mater.* **2009**, *19*, 1987-1992; b) O. M. Slobodian, P. M. Lytvyn, A. S. Nikolenko, V. M. Naseka, O. Y. Khyzhun, A. V. Vasin, S. V. Sevostianov and A. N. Nazarov, *Nanoscale Res. Lett.* **2018**, *13*, 139; c) H. F. Liang, C. T. G. Smith, C. A. Mills and S. R. P. Silva, *J Mater Chem* **2015**, *3*, 12484-12491; d) M. A. Velasco-Soto, S. A. Perez-Garcia, J. Alvarez-Quintana, Y. Cao, L. Nyborg and L. Licea-Jimenez, *Carbon* **2015**, *93*, 967-973.

[48] a) J. K. Wassei and R. B. Kaner, *Mater.Today* **2010**, *13*, 52-59; b) Z. P. Wang, Q. R. Yao, Y. L. Hu, C. Li, M. Hussmann, B. Weintrub, J. N. Kirchhof, K. Bolotin, T. Taniguchi, K. Watanabe and S. Eigler, *RSC Adv.* **2019**, *9*, 38011-38016.

[49] G. Cassabois, P. Valvin and B. Gil, *Nat. Photonics.* **2016**, *10*, 262-266.

[50] C. R. Dean, A. F. Young, I. Meric, C. Lee, L. Wang, S. Sorgenfrei, K. Watanabe, T. Taniguchi, P. Kim, K. L. Shepard and J. Hone, *Nat. Nanotechnol.* **2010**, *5*, 722-726.

[51] C. E. Halbig, R. Lasch, J. Krull, A. S. Pirzer, Z. P. Wang, J. N. Kirchhof, K. I. Bolotin, M. R. Heinrich and S. Eigler, *Angew. Chem. Int. Edit* **2019**, *58*, 3599-3603.

[52] a) G. Eda and M. Chhowalla, *Adv. Mater.* **2010**, *22*, 2392-2415; b) D. W. Boukhvalov and M. I. Katsnelson, *Journal of the American Chemical Society* **2008**, *130*, 10697-10701.

[53] C. Mattevi, G. Eda, S. Agnoli, S. Miller, K. A. Mkhoyan, O. Celik, D. Mastrogiovanni, G. Granozzi, E. Garfunkel and M. Chhowalla, *Adv. Funct. Mater.* **2009**, *19*, 2577-2583.

[54] Q. B. Zheng, Z. G. Li, J. H. Yang and J. K. Kim, *Prog. Mater. Sci.* **2014**, *64*, 200-247.

[55] C. Mattevi, G. Eda, S. Agnoli, S. Miller, K. A. Mkhoyan, O. Celik, D. Mastrogiovanni, G. Granozzi, E. Garfunkel and M. Chhowalla, *Adv. Funct. Mater.* **2009**, *19*, 2577-2583.

8. Publications and conference contributions

A) publications

1. Z. Wang, Q. Yao, Y. Hu, C. Li, M. Hußmann, B. Weintrub, J. N. Kirchhof, K. Bolotin, T. Taniguchi, K. Watanabe, S. Eigler, Influence of SiO_2 or h-BN substrate on the room-temperature electronic transport in chemically derived single layer graphene, *RSC Adv.* **2019**, *9*, 38011-38016.

2. Z. Wang, Q. Yao, S. Eigler, Room-temperature transport properties of graphene with defects derived from oxo-graphene, *Chem. Eur. J.,* **2020**, *26*, 1-7.

3. Z. Wang, Q. Yao, Christof Neumann, Felix Börrnert, Julian Renner, Ute Kaiser, Andrey Turchanin, Harold J. W. Zandvliet and Siegfried Eigler, Identification of Semiconductive Patches in Thermally Processed Monolayer Oxo-Functionalized Graphene, *Angew. Chem. Int. Ed*, Under review.

4. C. Halbig, R. Lasch, J. Krüll, A. Pirzer, Z. Wang, Ma. R. Heinrich and S. Eigler, Selective Functionalization of Graphene at Defect-Activated Sites by Arylazocarboxylic tert-Butyl Esters, *Angew. Chem. Int. Ed.* **2019**, *58*, 3599–3603.

5. S. M. Brülls, V. Cantatore, Z. Wang, P. L. Tam, P. Malmberg, J. Stubbe, B. Sarkar, I. Panas, J. Mårtensson, and S. Eigler, Evidence for Electron Transfer between Graphene and Non-covalently Bound π-Systems, *Chem. Eur. J.*, submitted.

6. X. Yu**, Z. Wang**, Z. Su and G. Wei, Design, fabrication, and biomedical applications of bioinspired peptide–inorganic nanomaterial hybrids, *J. Mater. Chem. B*, **2017**, 5, 1130-1142.

7. D. Li, W. Zhang, X. Yu, **Z. Wang**, Z. Su and G. Wei, When Biomolecules Meet Graphene: from Molecular Level Interactions to Material Design and Applications. *Nanoscale* **2016***, 8,* 19491-19509.

8. L. Huang, **Z. Wang** and J. Zhang, Full printed, Fast Response-Recovery and Chemically Modified Graphene Gas Sensors for Trance Level Detection of NO_2 at Room Temperature, *ACS Appl. Mater. Interfaces* **2014**, 6, 10, 7426-7433.

9. Q. Chang, **Z. Wang**, J. Wang and L. Huang, Graphene Nanosheets Inserted by Silver Nanoparticles as 0-Dimensinal Nanospacers for Dye Sensitized Solar. *Nanoscale*, **2014**, *6* (10), 5410-5415.

B) conferences

1. **Z. Wang**, First Ulm-Erlangen Mini-Symposium on Functional Organic Materials 2017, Ulm, Germany, poster.

2. **Z. Wang**, Flatlands Beyond Graphene 2018, Leipzig, Germany, poster.

3. **Z. Wang**, Women in Science-1st Erlangen Symposium 2019, Erlangen, Germany, Poster.

4. **Z. Wang**, Fifth Erlangen Symposium on Synthetic Carbon Allotropes 2019, Erlangen, Germany, Poster.

Acknowledgements

Statement of the author

I declare on the affidavit that I have written the dissertation independently and have used no sources other than those I have indicated and that there are no facts which make me unworthy of the conduct of a doctoral degree under the provisions of the law governing academic degrees. Further I declare my consent that the electronic version of my dissertation, while maintaining my copyrights and data protection, may be subjected to a separate review regarding the independent preparation of the dissertation. I have not submitted the dissertation anywhere else to obtain an academic degree and have not already passed this or a similar doctoral exam without success.

Berlin,

_____

Zhenping Wang